IDŐJÁRÁS

QUARTERLY JOURNAL OF THE HUNGAROMET
HUNGARIAN METEOROLOGICAL SERVICE

CONTENTS

VOL. 129 * NO. 3 * JULY – SEPTEMBER 2025

IDŐJÁRÁS

Quarterly Journal of the HungaroMet Hungarian Meteorological Service

Editorial Office: Kitaibel P.u. 1, H-1024 Budapest, Hungary
P.O. Box 38, H-1525 Budapest, Hungary
E-mail: journal.idojaras@met.hu

Indexed and abstracted in Science Citation Index Expanded™ and Journal Citation Reports/Science Edition
Covered in the abstract and citation database SCOPUS®
Included in EBSCO's database

Subscription by mail:
IDŐJÁRÁS, P.O. Box 38, H-1525 Budapest, Hungary
E-mail: journal.idojaras@met.hu

DOI:10.28974/idojaras.2025.3.1

IDŐJÁRÁS

Quarterly Journal of the HungaroMet Hungarian Meteorological Service
Vol. 129, No. 3, July – September, 2025, pp. 241–263

Homogenized and gridded daily surface air pressure data series in Hungary from 1901 to 2023

Olivér Szentes[1,2,*], **Rita Pongrácz**[3], and **Mónika Lakatos**[1]

[1]*Climate Research Department*
HungaroMet Hungarian Meteorological Service
Kitaibel Pál u.1, Budapest 1024, Hungary

[2]*ELTE Faculty of Science, Doctoral School of Earth Sciences*
Budapest, Hungary

[3]*ELTE Department of Meteorology*
Pázmány Péter st. 1/A, Budapest 1117, Hungary

**Corresponding Author e-mail: szentes.o@met.hu*

(Manuscript received in final form February 25, 2025)

Abstract—To describe and study the climate and its changes more accurately, climate databases are needed that are representative in time and spatial coverage, and that are based on sufficiently long measurement data series. In Hungary, air pressure measurements have a long history, similar to temperature and precipitation, but a homogeneous gridded database of Hungarian air pressure measurements over a century, with a daily resolution covering the whole 20th century, has not yet been produced. Therefore, the main aim of this research was to produce a homogenized gridded daily air pressure database from the beginning of the 20th century, which is currently available from 1961 only. In addition, in the period after 1961, and especially in the last few decades, station data series are used in much greater numbers than before. This will produce a more accurate interpolation, i.e., a more accurate grid point database than at present, which can be updated annually in the future, as for temperature and precipitation.

In this paper, we describe the methods used, discuss the station systems used for homogenization and interpolation of air pressure in different time periods, analyze the main verification statistics of the homogenization, and also analyze the results of the interpolation, examine the annual, seasonal, and monthly surface air pressure data series and their extremes, including the daily extremes for the period 1901–2023.

Key-words: climate data, station level air pressure, homogenization, interpolation, MASH, MISH, verification statistics, gridded data series

INSTRUCTIONS TO AUTHORS OF *IDŐJÁRÁS*

The purpose of the journal is to publish papers in any field of meteorology and atmosphere related scientific areas. These may be

- research papers on new results of scientific investigations,
- critical review articles summarizing the current state of art of a certain topic,
- short contributions dealing with a particular question.

Some issues contain "News" and "Book review", therefore, such contributions are also welcome. The papers must be in American English and should be checked by a native speaker if necessary.

Authors are requested to send their manuscripts to

Editor-in Chief of IDŐJÁRÁS
P.O. Box 38, H-1525 Budapest, Hungary
E-mail: journal.idojaras@met.hu

including all illustrations. MS Word format is preferred in electronic submission. Papers will then be reviewed normally by two independent referees, who remain unidentified for the author(s). The Editor-in-Chief will inform the author(s) whether or not the paper is acceptable for publication, and what modifications, if any, are necessary.

Please, follow the order given below when typing manuscripts.

Title page should consist of the title, the name(s) of the author(s), their affiliation(s) including full postal and e-mail address(es). In case of more than one author, the corresponding author must be identified.

Abstract: should contain the purpose, the applied data and methods as well as the basic conclusion(s) of the paper.

Key-words: must be included (from 5 to 10) to help to classify the topic.

Text: has to be typed in single spacing on an A4 size paper using 14 pt Times New Roman font if possible. Use of S.I. units are expected, and the use of negative exponent is preferred to fractional sign. Mathematical formulae are expected to be as simple as possible and numbered in parentheses at the right margin.

All publications cited in the text should be presented in the *list of references*, arranged in alphabetical order. For an article: name(s) of author(s) in Italics, year, title of article, name of journal, volume, number (the latter two in Italics) and pages. E.g., *Nathan, K.K.*, 1986: A note on the relationship between photosynthetically active radiation and cloud amount. *Időjárás 90*, 10–13. For a book: name(s) of author(s), year, title of the book (all in Italics except the year), publisher and place of publication. E.g., *Junge, C.E.*, 1963: *Air Chemistry and Radioactivity.* Academic Press, New York and London. Reference in the text should contain the name(s) of the author(s) in Italics and year of publication. E.g., in the case of one author: *Miller* (1989); in the case of two authors: *Gamov* and *Cleveland* (1973); and if there are more than two authors: *Smith et al.* (1990). If the name of the author cannot be fitted into the text: *(Miller,* 1989); etc. When referring papers published in the same year by the same author, letters a, b, c, etc. should follow the year of publication. DOI numbers of references should be provided if applicable.

Tables should be marked by Arabic numbers and printed in separate sheets with their numbers and legends given below them. Avoid too lengthy or complicated tables, or tables duplicating results given in other form in the manuscript (e.g., graphs). *Figures* should also be marked with Arabic numbers and printed in black and white or color (under special arrangement) in separate sheets with their numbers and captions given below them. JPG, TIF, GIF, BMP or PNG formats should be used for electronic artwork submission.

More information for authors is available: journal.idojaras@met.hu

1. Introduction

To better understand the climate system and its changes, we need to analyze long-term data series of high quality. A detailed analysis of global and regional climate change, which is already clearly detectable today, therefore requires the longest possible reliable meteorological data series. This is the main goal of the current research, which aimed to create a long, homogenized station database, and hence a gridded air pressure database instead of the existing shorter and fewer station-based datasets. The resulting data will serve as an excellent basis for the further analysis of complex extreme meteorological and climatological events. In addition to the long-term analysis of air pressure for Hungary, the resulting air pressure database will also be used to check for erroneous/suspicious data for other meteorological elements (e.g., temperature data for cold air pool weather situations), thus helping to verify archive data during periods when measurements and observations are scarce.

Air pressure is a meteorological element whose spatial variability is essentially determined by altitude, so unlike, e.g., precipitation, where many stations with long time series are needed (*Szentes et al.*, 2023, 2024), for air pressure significantly fewer stations are sufficient to create a good quality climate database. However, the data series contain so-called inhomogeneities, for example due to station relocations, instrument changes or environmental changes, therefore, homogenization is needed (*Izsák* and *Szentimrey*, 2020). In the last decades, several methods and software were developed to homogenize meteorological data (*Venema* et al, 2012, 2020), such as MASH (*Szentimrey*, 1999, 2017, 2023, 2024a), standard normal homogeneity test (SNHT) (*Alexandersson*, 1986), and HOMER (*Joelsson* et al., 2021).

For data series homogenization, quality control and filling missing values, the MASH (Multiple Analysis of Series for Homogenization) procedure is used at the Climate Research Department of HungaroMet Nonprofit Zrt. (*Szentimrey*, 1999, 2008a, 2017). Using the MASHv3.03 software, homogenized and quality controlled data series without missing data are available for further analysis. The MASH method is based on hypothesis testing. An additive model with a significance level of 0.05 was used to homogenize the air pressure data series. Inhomogeneities were estimated from monthly data series. Monthly, seasonal, and annual inhomogeneities were harmonized in all MASH systems (taking into account different station networks). The homogenization of daily data is based on the detected monthly inhomogeneities.

Stations do not cover the country uniformly, so spatial interpolation is necessary to ensure spatial representativity. For such spatial interpolation, at HungaroMet we use the MISH (Meteorological Interpolation based on Surface Homogenized Data Basis) method, which was developed specifically for the interpolation of meteorological elements (*Szentimrey* and *Bihari*, 2007, 2014; *Szentimrey* 2024b).

2. Applied methods

In this chapter, we discuss the main features of the MASH and MISH methods used.

The MASH (*Szentimrey*, 1999, 2008b, 2017) procedure is used to homogenize the data sets, check the data and fill in missing data. Using the MASHv3.03 software, we have homogenized and quality controlled data sets filled with missing data, while the MISH method, MISHv1.03 software, is used to generate gridded data series.

2.1. The main properties of the MASH procedure

The homogenization of monthly series includes:

- a relative homogeneity test procedure,
- a step-by-step iteration procedure,
- additive (e.g., temperature) or multiplicative (e.g., precipitation) models that can be selected according to the meteorological element,
- quality control and missing data completion,
- homogenization of seasonal and annual series,
- metadata (probable dates of breakpoints) that can be used automatically,
- automatically generated verification files.

The homogenization of daily series is:

- based on the detected monthly inhomogeneities,
- quality controlled and containing the completion of missing data for each day.

For the air pressure data series, a normal distribution is assumed. In this case, an additive model can be used for homogenization (*Szentimrey*, 2008a). The general form of the additive model for additional monthly series for the same month in a small climatic region can be expressed as follows:

$$X_j(t) = C(t) + IH_j(t) + \varepsilon_j(t) \quad (j = 1,2,\dots,N;\ t = 1,2,\dots,n), \qquad (1)$$

where X is the data series, C is climate change, IH is inhomogeneity, ε is noise, N is the total number of data series, and n is the total number of time steps.

2.2. The main properties of the MISH method

By using the MISHv1.03 software (*Szentimrey* and *Bihari*, 2007, 2014), spatially representative data series are obtained. MISH consists of a modeling and an interpolation subsystem.

The main features of the modeling subsystem for climate statistics (local and stochastic) are as follows:

- it is based on long-term homogenized data series and supplementary deterministic model variables (elevation, topography, distance from the sea, etc.),
- additive (e.g., temperature) or multiplicative (e.g., precipitation) models can be selected,
- the modeling procedure should be executed only once before the applied interpolation,
- it uses a high resolution grid (e.g., 0.5'×0.5').

The main characteristics of the interpolation subsystem are as follows:

- use of the modeled parameters for the interpolation of the meteorological elements to any point of grid,
- use of background information (e.g., satellite, radar, forecast data),
- data series completion (missing value interpolation for daily or monthly station data) during the interpolation process,
- capability for interpolation, gridding of monthly or daily station data series.

In practice, many kinds of interpolation methods exist (e.g., inverse distance weighting (IDW), kriging, spline interpolation) with different approaches (*Szentimrey et al.*, 2011). According to the interpolation problem, the unknown predictand $Z(\mathbf{s}_0, t)$ is estimated by the use of the known predictors $Z(\mathbf{s}_i, t)$ $(i = 1, \dots, M)$, where the location vectors $\mathbf{s}$ are the elements of the given space domain, M is the total number of predictors, and t is time. The type of the adequate interpolation formula depends on the probability distribution of the meteorological element.

In the case of air pressure, an additive model can be used because of the assumed normal distribution:

$$\hat{Z}(\boldsymbol{s}_0, t) = \lambda_0 + \sum_{i=1}^{M} \lambda_i \cdot Z(\boldsymbol{s}_i, t), \tag{2}$$

where $\sum_{i=1}^{M} \lambda_i = 1$, $\lambda_i \geq 0$ $(i = 1, \dots, M)$, and λ_0, λ_i $(i = 1, \dots, M)$ are the interpolation parameters (*Szentimrey* and *Bihari*, 2014).

The root mean squared interpolation error (RMSE) is defined as follows:

$$RMSE(\boldsymbol{s}_0) = \sqrt{E\left(\left(Z(\boldsymbol{s}_0,t) - \hat{Z}(\boldsymbol{s}_0,t)\right)^2\right)}, \quad (3)$$

and the representativity (REP) of the station network can be defined as follows:

$$REP(\boldsymbol{s}_0) = 1 - \frac{RMSE(\boldsymbol{s}_0)}{D(\boldsymbol{s}_0)}, \quad (4)$$

where E is the expected value and $D(\boldsymbol{s}_0)$ is the standard deviation of the predictand.

2.3. ANOVA (analysis of variance)

To compare gridded data sets interpolated from different numbers of data series, ANOVA is performed to examine the estimated spatio-temporal variances (*Szentimrey* and *Bihari*, 2014; *Izsák et al*., 2022).

Notations:

$Z(\boldsymbol{s}_j,t)$ $(j = 1,\dots,N; t = 1,\dots,n)$ – gridded data series $(\boldsymbol{s}_j: \text{location}, t: \text{time})$,

$\hat{E}(\boldsymbol{s}_j) = \frac{1}{n}\sum_{t=1}^{n} Z(\boldsymbol{s}_j,t)$ (j=1,…,N) – temporal mean at location $\boldsymbol{s}_j$,

$\hat{D}(\boldsymbol{s}_j) = \sqrt{\frac{1}{n}\sum_{t=1}^{n}(Z(\boldsymbol{s}_j,t) - \hat{E}(\boldsymbol{s}_j))^2}$ (j=1,…,N) – temporal standard deviation at location $\boldsymbol{s}_j$,

$\hat{E}(t) = \frac{1}{N}\sum_{j=1}^{N} Z(\boldsymbol{s}_j,t)$ (t=1,…,n) – spatial mean at moment t,

$\hat{D}(t) = \sqrt{\frac{1}{N}\sum_{j=1}^{N}(Z(\boldsymbol{s}_j,t) - \hat{E}(t))^2}$ (t=1,…,n) – spatial standard deviation at moment t,

$\hat{E} = \frac{1}{N\cdot n}\sum_{j=1}^{N}\sum_{t=1}^{n} Z(\boldsymbol{s}_j,t) = \frac{1}{N}\sum_{j=1}^{N}\hat{E}(\boldsymbol{s}_j) = \frac{1}{n}\sum_{t=1}^{n}\hat{E}(t)$ – total mean,

$\hat{D}^2 = \frac{1}{N\cdot n}\sum_{j=1}^{N}\sum_{t=1}^{n}(Z(\boldsymbol{s}_j,t) - \hat{E})^2$ – total variance.

Partitioning of total variance (Theorem):

$$\widehat{D}^2 = \frac{1}{N}\sum_{j=1}^{N}(\hat{E}(\boldsymbol{s}_j) - \hat{E})^2 + \frac{1}{N}\sum_{j=1}^{N}\widehat{D}^2(\boldsymbol{s}_j) = \frac{1}{n}\sum_{t=1}^{n}(\hat{E}(t) - \hat{E})^2 + \frac{1}{n}\sum_{t=1}^{n}\widehat{D}^2(t).$$

The analysis of these terms is recommended to characterize the spatio-temporal variability.

Spatial terms:

spatial variance of temporal means: $\frac{1}{N}\sum_{j=1}^{N}(\hat{E}(\boldsymbol{s}_j) - \hat{E})^2$,

and temporal mean of spatial variances: $\frac{1}{n}\sum_{t=1}^{n}\widehat{D}^2(t)$.

Temporal terms:

spatial mean of temporal variances: $\frac{1}{N}\sum_{j=1}^{N}\widehat{D}^2(\boldsymbol{s}_j)$,

and temporal variance of spatial means $\frac{1}{n}\sum_{t=1}^{n}(\hat{E}(t) - \hat{E})^2$.

We do not show the variances but the standard deviations instead, to make the values easier to interpret, especially in the case of pressure:

total standard deviation: $\widehat{D} = \sqrt{\frac{1}{N\cdot n}\sum_{j=1}^{N}\sum_{t=1}^{n}\left(Z(\boldsymbol{s}_j, t) - \hat{E}\right)^2}$,

spatial standard deviation of temporal means: $\sqrt{\frac{1}{N}\sum_{j=1}^{N}(\hat{E}(\boldsymbol{s}_j) - \hat{E})^2}$,

root spatial mean of temporal variances: $\sqrt{\frac{1}{N}\sum_{j=1}^{N}\widehat{D}^2(\boldsymbol{s}_j)}$,

temporal standard deviation of spatial means: $\sqrt{\frac{1}{n}\sum_{t=1}^{n}(\hat{E}(t) - \hat{E})^2}$,

root temporal mean of spatial variances: $\sqrt{\frac{1}{n}\sum_{t=1}^{n}\widehat{D}^2(t)}$.

3. Data

The meteorological measurements in Hungary are stored in the climate database of HungaroMet. Nowadays, the meteorological measurements of the automatic meteorological stations are continuously added to the database, where air pressure measurements are also recorded. The records of older, pre-automation (before 1990s) periods are kept in the climatology books. The digitization of the old data into the climate database is still in progress today. Since the 1960s, most of the air pressure data are available in digital format, while most of the data from earlier decades are still only available on paper. At the same time, air pressure is a much less variable meteorological element than, for example, precipitation, so that data from a few stations are sufficient. The digital climate database already contains a sufficient number of air pressure records from the early 20th century for different areas of the country, so that a homogenized gridded air pressure database covering the whole 20th century can be established. Prior to the complete renewal of the air pressure database, homogenization of air pressure data series was done in one step, starting in 1961 with 22 station data series homogenized and interpolated to a regular grid of 0.1°. As part of the research, the climate database on air pressure has been completely renewed. Similarly to temperature and precipitation, daily homogenized and gridded data series are now available for air pressure from the beginning of the 20th century. The previous one-step homogenization has been replaced by a three-step homogenization: from 1901 onwards, 10 stations are used for daily data, from 1951 onwards 25 stations, and from 1997 onwards 41 stations. It is important to note that the homogenization of air pressure is based on the instrumental air pressure data series, i.e., station-level pressure values, and not on the sea-level pressure values, which is a derived, non-measured quantity. The design of the station systems used for homogenization is essentially determined by the fact that, on the one hand, a larger number of digitized data sets are available since the 1950s and, on the other hand, the number of air pressure stations increased significantly due to the automation that started in the second half of the 1990s. *Fig. 1* shows the amount of monthly air pressure data available in the different MASH systems from January 1901 to December 2023.

Fig. 1. Number of air pressure data used in the three MASH systems between 1901 and 2023, by month.

The location of air pressure stations in Hungary is shown in *Fig. 2*.

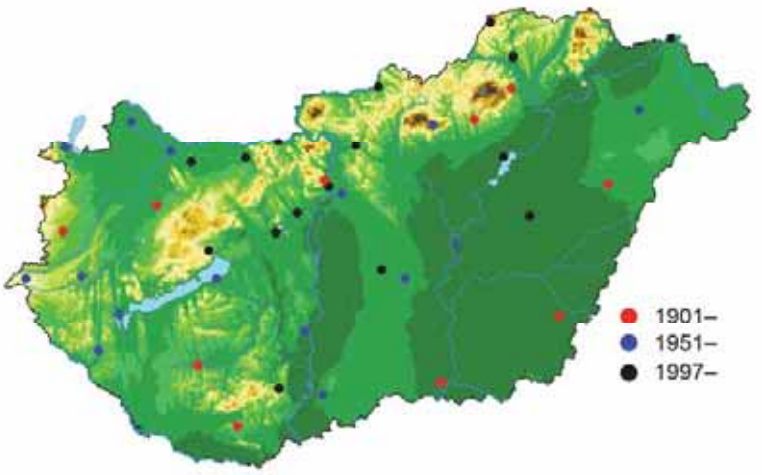

Fig. 2. Location of the stations used in the three MASH systems in Hungary.

4. Results

4.1. Results of homogenization

The homogenization is based on a total of three different station systems, where the monthly, seasonal, and annual inhomogeneities detected in each station system are harmonized during the homogenization process. Naturally, the MASH systems with shorter periods include stations with longer series (e.g., MASH2 includes MASH1 series from 1951 onwards). The homogenization process automatically produces verification statistics. *Table 1* summarizes the main verification statistics for the homogenization of annual air pressure averages for each station system.

Table 1. Main verification statistics of homogenization for annual air pressure means

	MASH1	**MASH2**	**MASH3**
Number of series	10	25	41
Critical value (significance level: 0.01)	21.93	21.40	20.53
Test statistics before homogenization	18359.40	18016.62	3711.91
Test statistics after homogenization	21.74	19.34	16.04
Relative modification of series	1.17	0.78	0.27
Representativity of station network	0.93	0.93	0.93

Before homogenization, the average test statistics for all station systems were well above the critical value, while the test statistics after homogenization were below the critical value, so the air pressure database can be considered homogeneous, with a representative station dataset in time after homogenization. The extremely high test statistic values before homogenization are mainly caused by the fact that air pressure is a meteorological element with a very small temporal variance, and therefore significant breaks, so-called inhomogeneities, can be caused by station relocations in the data series. The changes in the data series are of course larger for longer data series, because longer data series contain more inhomogeneities, for example due to more instrument changes and relocations. The representativity of the station network is similar in all three MASH systems, indicating that a few stations can be used to provide a good substitute for the meteorological element.

The significant inhomogeneities due to relocations are illustrated by the annual air pressure data series for Miskolc (*Fig. 3*), where the three most significant inhomogeneities were caused by the known relocations of the station.

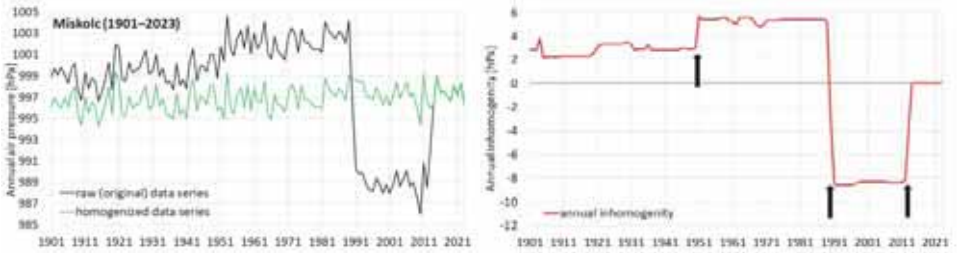

Fig. 3. Raw and homogenized annual air pressure means (left) and annual inhomogeneities (right) in Miskolc between 1901 and 2023, where black arrows indicate well-documented station relocations.

In the mid-20th century, measurements were taken at the airport in the lower part of the city, from where the station was moved to the Avas hill in 1990, more than 100 m higher than the previous measuring site. This resulted in a 14 hPa decrease in the air pressure data. Later, in 2013, the meteorological station together with the air pressure measurements were moved to the western part of Miskolc, to the valley of Diósgyőr, causing another significant inhomogeneity in the air pressure data series.

4.2. Results of interpolation

After homogenization, the data series were interpolated to a regular grid of 0.1° using the MISHv1.03 software. The mean of the values in grid points represents the country average.

The question arises, how similar the grid point data series produced from different numbers of data series are. Our aim is to create a grid point air pressure database in which grid point data series interpolated from 10 stations (MISH1), 25 stations (MISH2), and 41 stations (MISH3) show similar spatiotemporal characteristics. ANOVA was performed on the grid point data series interpolated from three different station systems for the period 1997-2023 for all station systems. *Table 2* shows the main results of the ANOVA for the annual air pressure means.

Table 2. The main ANOVA results for the gridded annual mean air pressure data series for different station systems over the period 1997-2023 (all values are expressed in hPa)

	MISH1	**MISH2**	**MISH3**
Total mean	998.52	998.52	998.52
Total standard deviation	9.85	9.84	9.85
Spatial standard deviation of temporal means	9.79	9.78	9.79
Root spatial mean of temporal variances	1.05	1.05	1.05
Temporal standard deviation of spatial means	1.05	1.05	1.05
Root temporal mean of spatial variances	9.79	9,79	9.79

The ANOVA results clearly show that the total (spatial) mean is the same for all MISH systems over the period 1997–2023. In addition, the spatial variance of the temporal averages and the temporal variance of the spatial averages are almost exactly identical, which shows that air pressure is a very well interpolated meteorological element, and that a few data series is sufficient to create a good quality air pressure climate database.

As far as the annual air pressure averages and the spatial variance of the annual air pressure averages over the period 1997–2023 are concerned, the interpolation results do not show significant differences, with only a few hundredths of a hPa difference (*Fig. 4*).

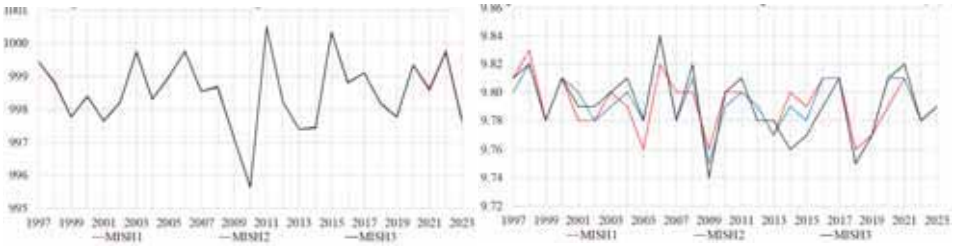

Fig. 4. Annual mean air pressure (left) and spatial standard deviations of annual means (right) for different station systems in Hungary, for the period 1997–2023.

When comparing the spatial means from the MISH1 and MISH2 station systems with the interpolation from MISH3 of 41 stations, it can be seen (*Fig. 5*) that the mean error in absolute value is within 0.01 hPa in each month, and the RMSE values are also within 0.05 hPa in each month. This implies that the spatial

mean produced from a smaller set of stations can also be considered representative for Hungary. After interpolation, a spatially representative surface air pressure database becomes available.

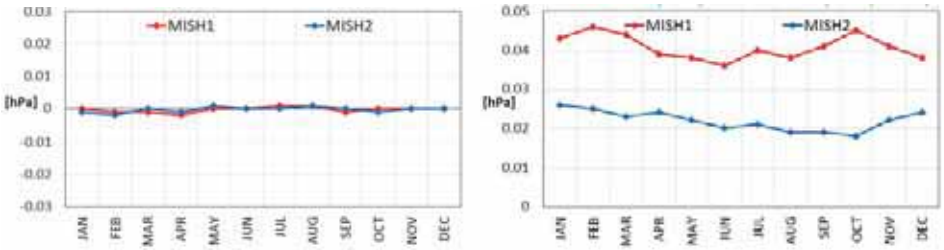

Fig. 5. Monthly mean errors (left) and RMSE values (right) of spatial means of surface air pressure for the period 1997–2023 compared to interpolation from 41 stations in different MISH systems.

4.3. Annual air pressure

Fig. 6 shows the spatial means of annual air pressure values from the beginning of the 20th century. The annual average surface air pressure in Hungary is generally between 997 and 1000 hPa.

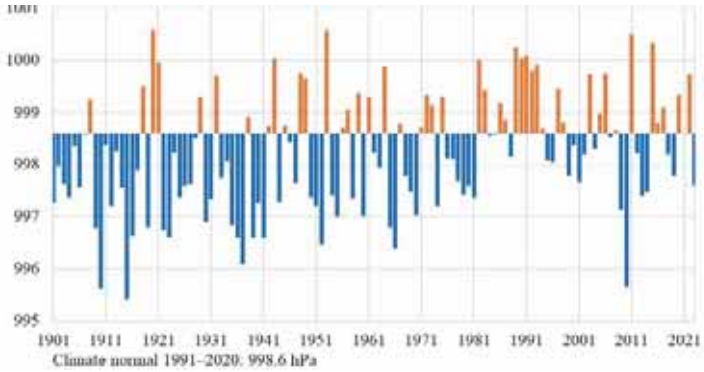

Fig. 6. Spatial means of annual surface air pressure in Hungary from 1901 to 2023.

The annual mean air pressure values show a reverse relationship with annual precipitation totals. Although the extremes do not coincide, in years with higher precipitation (e.g., early 20th century), more cyclones occur, resulting in lower

pressure means, while in drier years, when more anticyclones dominate the weather, the pressure means is higher. The wettest year on average in Hungary since the beginning of the 20th century was 2010, and the driest year was 2011. This is also reflected in the annual mean air pressure, which was below 996 hPa in 2010, while it exceeded 1000 hPa in 2011. Considering the long averaging time period and a relatively small overall variance, this difference of 4–5 hPa is quite substantial between years.

4.4. Seasonal and monthly air pressure

Winter

Among the seasons, the greatest variability in air pressure occurs in winter (*Fig. 7*). In some years, winter weather in Hungary is mostly determined by Mediterranean cyclones, while there are winters when northern European anticyclones are more dominant.

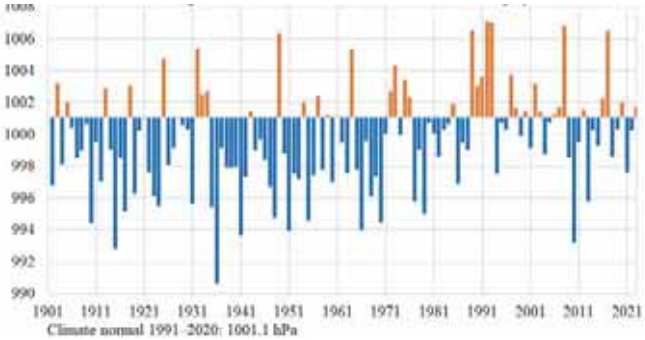

Fig. 7. Spatial means of winter surface air pressure in Hungary from 1901/1902 to 2022/2023.

Looking at the individual winter months within the season, it can be observed that spatial means below 990 hPa and above 1010 hPa can occur in all the three months (*Fig. 8*). January and February show both higher and lower air pressure values in each decade, while December exhibits a higher frequency of higher monthly air pressure means compared to the 1991-2020 average since the 1970s than in the first half of the 20th century.

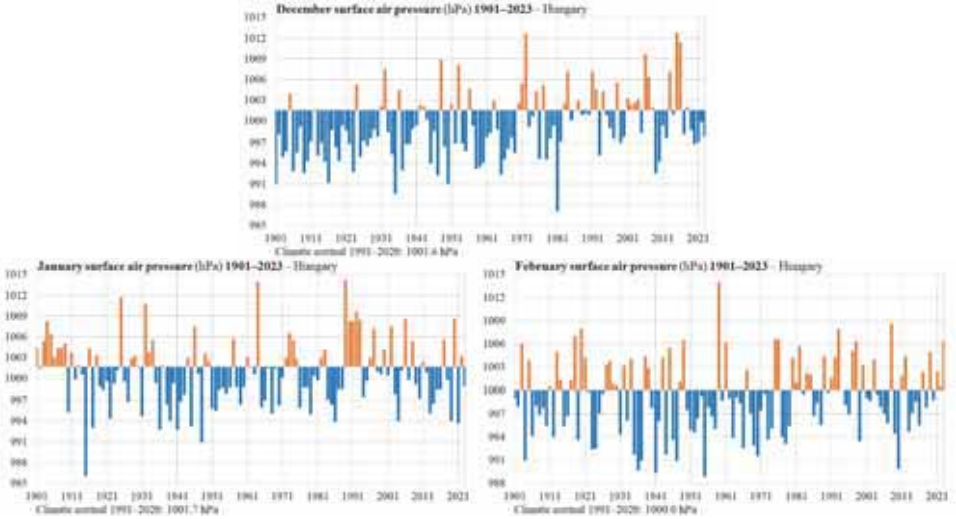

Fig. 8. Spatial means of surface air pressure in the winter months in Hungary from 1901 to 2023.

Spring

In spring, the entire pressure range is much smaller than in winter, mostly between 994 and 1000 hPa. Among the seasonal averages for 1991–2020, the mean spring pressure is the lowest. Averages are lower in the first three decades of the 20th century, when springs were wetter, while higher pressure averages occurred more frequently in the mid-20th century and in the last two decades (*Fig. 9*).

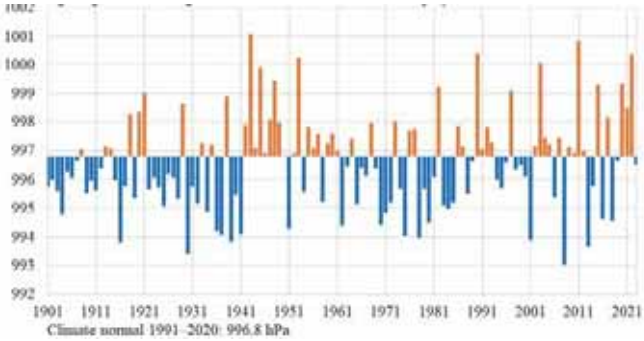

Fig. 9. Spatial means of spring surface air pressure in Hungary from 1901 to 2023.

Of the spring months, March is the most variable. Lower air pressures in April were recorded in the 1920s, 1930s, and 1970s, while higher values were recorded in the mid-20th century and the last 20 years (*Fig. 10*). Nevertheless, the mean air pressure in April is the lowest of all months over the period 1991–2020. In May, the mean reaches 1000 hPa less frequently, and there is no spatial means below 990 hPa.

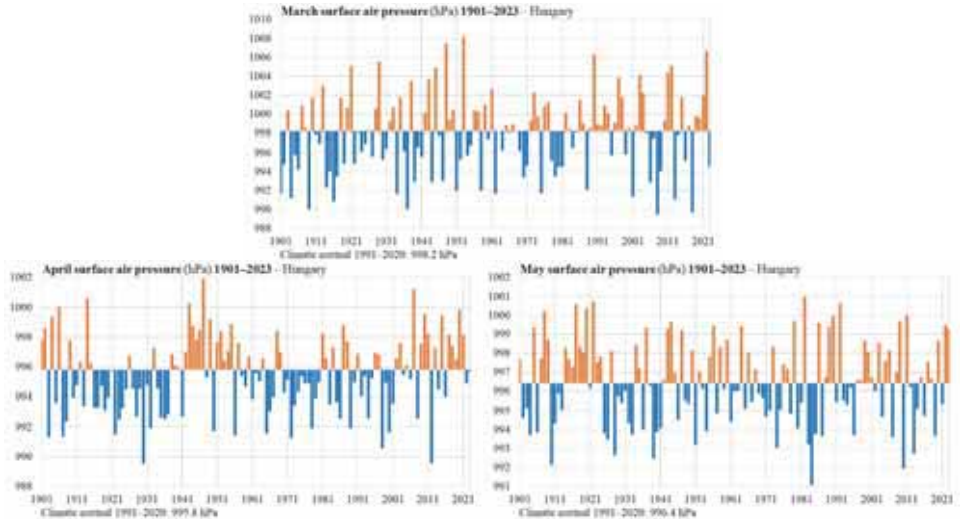

Fig. 10. Spatial means of surface air pressure in the spring months in Hungary from 1901 to 2023.

Summer

The mean air pressure in summer is very similar to spring, only 0.1 hPa higher on average. However, the least variability of all seasons occurs in summer, with the spatial mean summer air pressure typically remaining within a range of 3 hPa, between 995 and 998 hPa (*Fig. 11*).

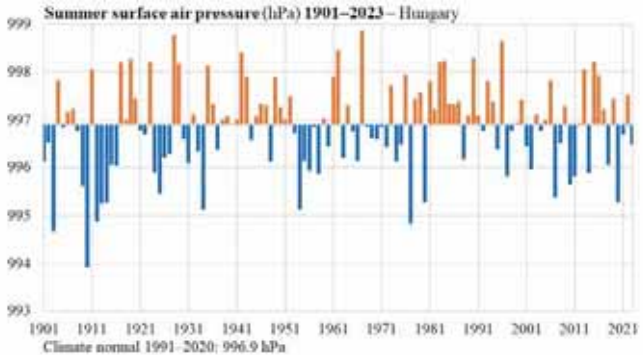

Fig. 11. Spatial means of summer surface air pressure in Hungary from 1901 to 2023.

In summer, the pressure field is often uncharacteristic, with cyclones and anticyclones much less dominant than in other seasons, especially compared to winter. This is also reflected in the air pressure values during the summer months. The highest monthly spatial means rarely reach 1000 hPa, while values below 993 hPa are also seldom (*Fig. 12*).

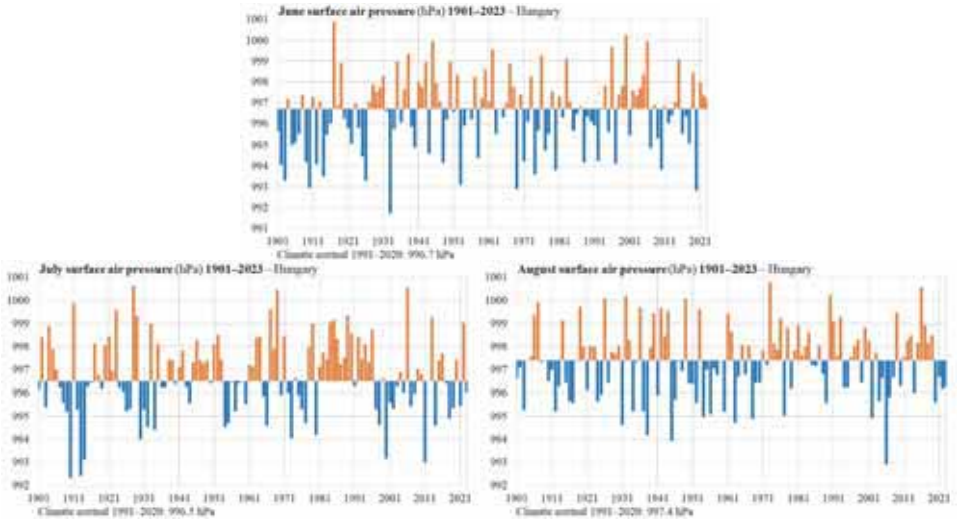

Fig. 12. Spatial means of surface air pressure in the summer months in Hungary from 1901 to 2023.

Autumn

The spatial mean for autumn air pressure was mostly below the 1991–2020 average in the first four decades of the 20th century, and then more consistently above the 1991–2020 average in the following four decades. Autumn surface air pressure is generally around 1000 hPa, typically between 997 and 1003 hPa (*Fig. 13*).

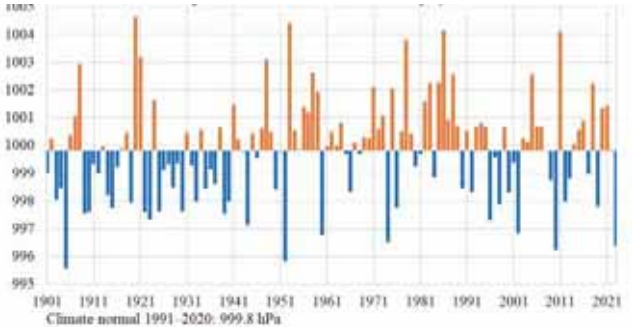

Fig. 13. Spatial means of autumn surface air pressure in Hungary from 1901 to 2023

As in the seasonal mean, September and October are dominated by lower air pressure in the first four decades of the 20th century, and then higher pressure until the 1980s (*Fig. 14*). September also shows a clear decline in the 1990s, when cyclonic circulation conditions became more frequent in September. As we approach winter, there is an increasing variability in air pressure values. The November surface air pressure is more similar to the winter months than to the other two autumn months, with monthly mean values above 1010 hPa.

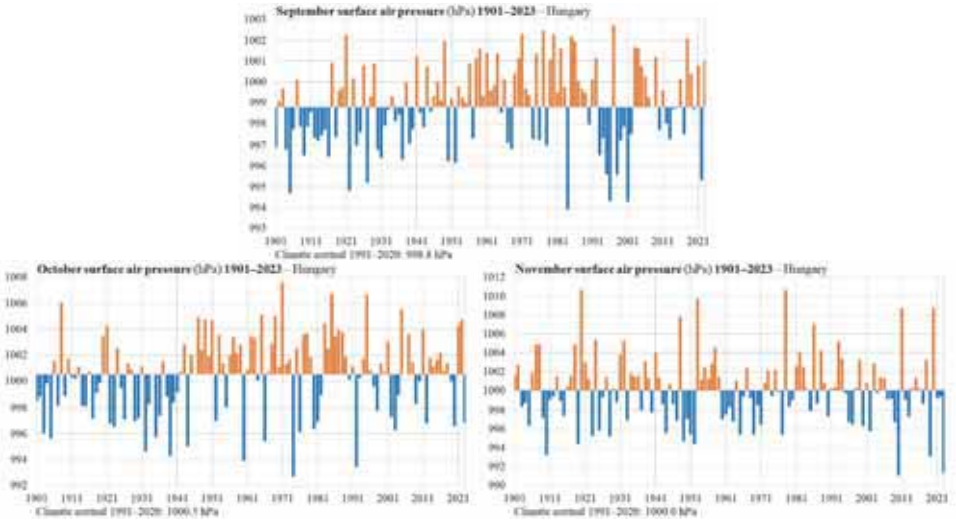

Fig. 14. Spatial means of surface air pressure in the autumn months in Hungary from 1901 to 2023

Table 3 summarizes the monthly, seasonal, and annual extremes and standard deviations for the period 1901–2023, as well as the averages for 1991–2020. Both the lowest and highest monthly air pressure were recorded in January. Monthly mean pressures above 1010 hPa averaged over the winter months in November, while monthly mean pressures below 990 hPa averaged over January to April and December since the beginning of the 20th century. The standard deviation of monthly values is close to 5 hPa in winter and less than 2 hPa in summer.

Table 3. Monthly, seasonal, annual extremes and standard deviations of spatial means of air pressure for the period 1901–2023 and the 1991–2020 averages

Month/ season	Lowest		Highest		1901–2023 standard deviation [hPa]	1991–2020 average [hPa]
	hPa	year	hPa	Year		
January	986.1	1915	1014.3	1989	4.9	1001.7
February	988.9	1955	1014.0	1959	4.9	1000.0
March	989.5	2008	1008.2	1953	4.2	998.2
April	989.5	1930	1002.0	1947	2.6	995.8
May	991.1	1984	1001.0	1982	2.3	996.4
June	991.7	1933	1000.9	1917	1.8	996.7
July	992.3	1910	1000.7	1928	1.7	996.5
August	992.9	2006	1000.8	1973	1.6	997.4
September	993.9	1984	1002.8	1997	2.0	998.8
October	992.7	1974	1007.6	1971	3.1	1000.5
November	991.0	2010	1010.7	1920	3.7	1000.0
December	987.1	1981	1012.8	2015	4.9	1001.6
Winter	990.7	1935/1936	1007.1	1991/1992	3.3	1001.1
Spring	993.0	2008	1001.1	1943	1.7	996.8
Summer	993.9	1910	998.9	1967	1.0	996.9
Autumn	995.6	1905	1004.7	1920	1.8	999.8
Year	995.4	1915	1000.6	1920	1.2	998.6

4.5. Daily air pressure

In the monthly and seasonal air pressure data, it was already shown that there is much more variability in air pressure in winter than in summer, and that both absolute maximum and minimum values occur in winter. In this chapter, the daily spatial means of surface air pressure is analyzed together with its annual pattern and its daily extremes.

The daily mean surface air pressure is above 1000 hPa for most of the winter months and below 1000 hPa from mid-March to mid-September (*Fig. 15*). For the

1991–2020 averages, the highest daily pressure occurred on January 15 (1004.5 hPa) and the lowest on April 18 (993.4 hPa). There is a distinct annual pattern of extremes, daily maximum and minimum values. The maxima and minima clearly occur in winter, with a substantially narrower interval of pressure values in summer, with higher minima and lower maxima. The mean daily minimum of spatial averages is 974.2 hPa in January and 985.8 hPa in July, while the corresponding mean maximum is 1023.2 hPa and 1006.1 hPa, respectively.

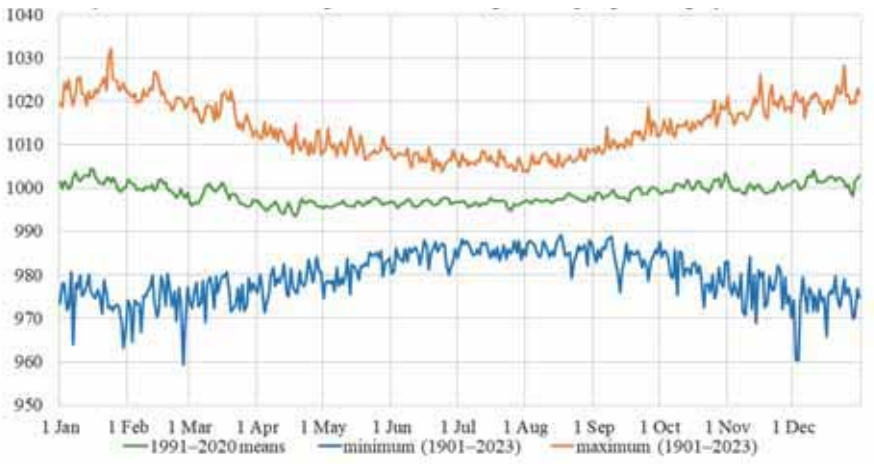

Fig. 15. Spatial means of daily surface air pressure 1991–2020 and daily extreme values for the period 1901–2023.

The daily spatial mean surface air pressure was the lowest on February 26, 1989 and the highest on January 24, 1907. The distribution of surface air pressure in Hungary on these days is shown in *Fig. 16*, while *Table 4* lists the ten lowest and ten highest values of spatial means of daily air pressure since the beginning of the 20th century.

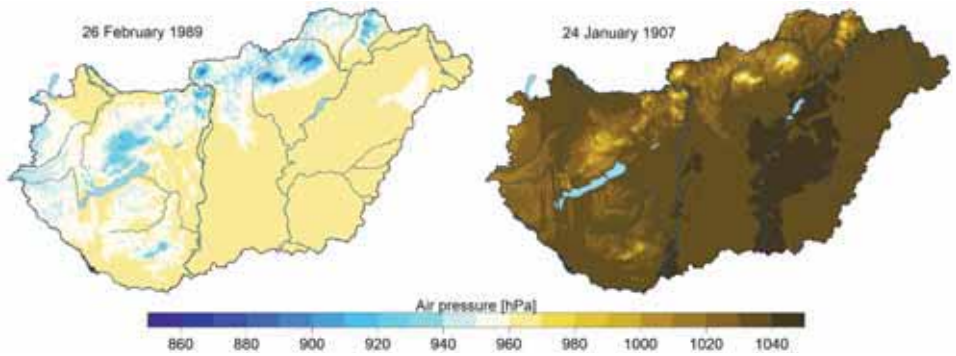

Fig. 16. Distribution of surface air pressure in Hungary on February 26, 1989 and January 24, 1907.

Table 4. Spatial means of daily surface air pressure lows and highs in Hungary, in period 1901-2023

	Lowest		Highest	
	hPa	**Date**	**hPa**	**Date**
1.	959.3	February 26, 1989	1032.3	January 24, 1907
2.	960.3	December 3, 1976	1030.2	January 23, 1907
3.	960.6	December 2, 1976	1028.3	December 24, 1963
4.	963.2	January 30, 2015	1026.9	February 13, 1959
5.	964.0	January 7, 1912	1026.3	February 14, 1959
6.	964.5	February 3, 1912	1026.0	November 16, 1908
7.	965.9	December 16, 1962	1025.7	January 10, 1929
8.	966.9	February 7, 1974	1025.5	January 21, 1925
9.	967.9	December 2, 1935	1025.4	January 9, 1929
10.	968.0	January 31, 2015	1025.3	January 25, 1932

The weather in the Carpathian Basin in winter, especially in November and December, is often humid and foggy, with low-level stratus clouds in the lower few hundred meters of the atmosphere, during which maximum temperatures remain near freezing and low daily temperature fluctuations are common. Such weather situations can develop with persistently anticyclonic, i.e., high atmospheric pressure, while the higher mountains stay above the cloud cover, where the anticyclone is responsible for sunny, clear weather, with maximum temperatures several degrees above the lowlands. Such a cold air pool situation is illustrated in *Fig. 17*, where, in addition to the maximum temperatures measured at Kékestető and Gyöngyös (i.e., at the top and foot of the Mátra, respectively) in November 1978, the anomalies of the daily air pressure are shown as spatial averages for the entire country.

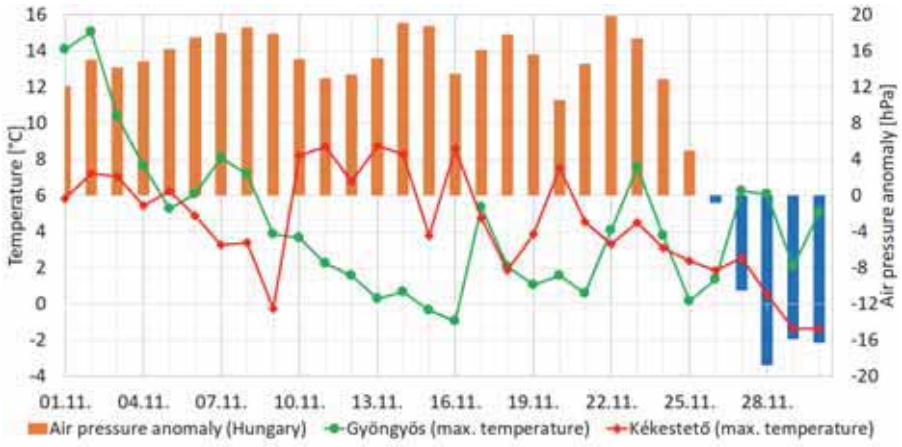

Fig. 17. Daily maximum temperatures at Kékestető and Gyöngyös and anomalies of daily surface air pressure anomalies of Hungarian spatial means in November 1978.

It can be seen that for most of the month, the air pressure was 12–20 hPa higher than usual. At the beginning and end of the month, the maximum daily temperature at the mountain station (Kékestető) was several degrees lower than normal. However, in the middle of the month, especially between November 10 and 16, maximum temperatures were lower at the foot of the mountain, in Gyöngyös, by 4–8 °C. Looking at the temperature data alone, one might therefore think that the values from Kékestető or Gyöngyös could be wrong, as the temperature should normally be several degrees lower on the mountain. However, considering the air pressure anomalies, it is clear that these reverse conditions occurred during a period of persistent high pressure in November, which suggests the formation of a cold air pool over Hungary. Nowadays, satellite imagery can also help in deciding on the temperature values in question in such weather situations, and the importance of daily air pressure data is enhanced when checking older suspicious data, especially before the mid-20th century, when there were fewer mountain stations to measure, as they can significantly help in checking archive data.

5. Summary

Within the framework of the present research, the surface air pressure database, which started in 1961, was completed from the beginning of the 20th century to the year 2024, thus, in addition to temperature and precipitation (*Szentes* et al., 2023), a daily climate database for surface air pressure was created, which is representative in time and space from the beginning of the 20th century to the present. In addition, station data series are used in much larger numbers in the

period after 1961, especially in the last few decades. Homogenized station time series and interpolated gridded air pressure database are produced from station air pressure measurements and, like other meteorological elements, can be updated annually in the future. The station systems used for the homogenization were presented, which is now done in three steps instead of the previous one-step homogenization. The interpolation results were also subjected to an ANOVA test, where it was shown that barometric pressure is a meteorological element that can be interpolated with high accuracy. When analyzing the monthly, seasonal, and annual averages of air pressure, a correlation with precipitation is apparent, as lower air pressures are associated with more intense cyclonic activity, and thus, more precipitation, while persistently high air pressures are associated with the lack of precipitation, even drought. During the winter period, high air pressure often causes the formation of a low-level stratus cloud (so-called cold air pool), under which the air is humid and air pollution increases substantially, often to levels above the health limit. The development and frequency of these weather events, which can have a significant impact on our health, can now be studied in more detail over the long term by examining long air pressure data series. Moreover, the air pressure database, which has been compiled since the early 20th century, can be used to check suspicious data from other meteorological elements (e.g., temperature data from cold air pool weather situations), helping to verify archive data at times when measurements are scarce.

Acknowledgement: This paper was supported by the ÚNKP-23-1 New National Excellence Program of the Ministry for Culture and Innovation from the source of the National Research, Development and Innovation Found, the framework of the Széchenyi Fund Plus program with the support of the RRF-2.3.1-21-2022-00014 National Multidisciplinary Laboratory for Climate Change project.

References

Alexandersson, H., 1986: A homogeneity test applied to precipitation data, *Int. J. Climatol. 6*, 661–675. https://doi.org/10.1002/joc.3370060607

Izsák, B. and *Szentimrey, T.*, 2020: To what extent does the detection of climate change in Hungary depend on the choice of statistical methods?. *Int. J. Geomath 11*, 17. https://doi.org/10.1007/s13137-020-00154-y

Izsák, B., Szentimrey, T., Lakatos, M., Pongrácz, R., and *Szentes, O.*, 2022: Creation of a representative climatological database for Hungary from 1870 to 2020, *Időjárás 126*, 1–26. https://doi.org/10.28974/idojaras.2022.1.1

Joelsson, M., Sturm, C., Södling, J., Engström, E., and *Kjellström, E.*, 2021: Automation and evaluation of the interactive homogenization tool HOMER, *Int. J. Climatol. 42*, 2861–2880. https://doi.org/10.1002/joc.7394

Szentes, O., Lakatos, M., and *Pongrácz, R.*, 2023: New homogenized precipitation database for Hungary from 1901, *Int. J. Climatol. 43*, 4457–4471, https://doi.org/10.1002/joc.8097

Szentes, O., Lakatos, M., Pongrácz, R., and *Szentes, O.*, 2024: Precipitation conditions in Hungary from 1854 to 2022, *Időjárás 128*, 171–193. https://doi.org/10.28974/idojaras.2024.2.3

Szentimrey T., 1999: Multiple Analysis of Series for Homogenization (MASH). Paper presented at the Proceedings of the Second Seminar for Homogenization of Surface Climatological Data, Budapest, Hungary, WMO WCDMP-No. 41: 27–46. Retrieved from https://library.wmo.int/index.php?lvl=notice_display&id=11624#.X48Glu28qUk

Szentimrey, T., 2008a: An overview on the main methodological questions of homogenization. In: (eds. *Lakatos, M., Szentimrey, T., Bihari, Z., Szalai, S.*) Proceedings of the Fifth Seminar for Homogenization and Quality Control in Climatological Databases. Seminar for Homogenization and Quality Control in Climatological Databases 5th session (29 May–2 June 2006; Budapest, Hungary). WMO/TD-No. 1493; WCDMP-No. 71, 1–6. World Meteorological Organization (WMO)

Szentimrey T., 2008b: Development of MASH Homogenization Procedure for Daily Data. In: (eds. *Lakatos, M., Szentimrey, T., Bihari, Z., Szalai, S.*) Proceedings of the Fifth Seminar for Homogenization and Quality Control in Climatological Databases. Seminar for Homogenization and Quality Control in Climatological Databases 5th session (29 May–2 June 2006; Budapest, Hungary). WMO/TD-No. 1493; WCDMP-No. 71, 123–130. World Meteorological Organization (WMO)

Szentimrey, T., 2017: Manual of homogenization software MASHv3.03, Hungarian Meteorological Service.

Szentimrey, T., 2023: Overview of mathematical background of homogenization, summary of method MASH and comments on benchmark validation. *Int. J. Climatol. 43*, 6314–6329. https://doi.org/10.1002/joc.8207

Szentimrey, T., 2024a: Development of new version MASHv4.01 for homogenization of standard deviation, *Időjárás 128*, 219–235. https://doi.org/10.28974/idojaras.2024.2.5

Szentimrey, T., 2024b: Statistical modeling of the present climate by the interpolation method MISH – theoretical considerations, *Időjárás 128*, 143–154. https://doi.org/10.28974/idojaras.2024.2.1

Szentimrey, T. and *Bihari, Z.*, 2007: Mathematical background of the spatial interpolation methods and the software MISH (Meteorological Interpolation based on Surface Homogeni-zed Data Basis). In: Proceedings from the Conference on Spatial Interpolation in Climatology and Meteorology, Budapest, Hungary, 2004, COST Action 719, COST Office, 17–27.

Szentimrey, T. and *Bihari, Z.*, 2014: Manual of interpolation software MISHv1.03, Hungarian Meteorological Service.

Venema V., Mestre, O., Aguilar, E., and *Auer, I.*, 2012: Benchmarking monthly homogenization algorithms. *Climate Past 8*, 89–115. https://doi.org/10.5194/cpd-7-2655-2011

Venema, V., Trewin, B., Wang, X., Szentimrey, T., Lakatos, M., Aguilar, E., Auer, I., Guijarro, J., Menne, M., Oria, C., Louamba, W., and *Rasul, G.*, 2020: Guidelines on Homogenization, 2020 Edition, Geneva: World Meteorological Organization

DOI:10.28974/idojaras.2025.3.2

IDŐJÁRÁS

Quarterly Journal of the HungaroMet Hungarian Meteorological Service
Vol. 129, No. 3, July – September, 2025, pp. 265–278

Characteristics of the September-December Teleconnection (SDT) in the current Atlantic Multidecadal Oscillation (AMO) phase

György Babolcsai [1,*] and **Tamás Hirsch**[2]

[1] *HungaroMet Hungarian Meteorological Service*
Kitaibel Pál Street 1, 1024 Budapest, Hungary

[2] *Federal Institute of Hydrology*
Am Mainzer Tor 1, 56068 Koblenz, Germany

**Corresponding Author e-mail: babolcsai.gy@met.hu*

(Manuscript received in final form November 10, 2024)

Abstract— The atmospheric teleconnection presented in our former paper (*Babolcsai* and *Hirsch*, 2019) shows a particularly strong regularity between the Euro-Atlantic mean sea level pressure anomaly pattern in September and the pattern three months later, in December, in the current positive AMO (Atlantic Multidecadal Oscillation) phase lasting since 1995.

Euro-Atlantic mean sea level pressure anomaly patterns for September were divided into four clusters, whereas cases that could not be classified as any of these, were assigned to a fifth cluster.

Based on the clustering, the December macrosynoptic situation in Europe can be predicted in a significant number of cases, and hence the sign of the temperature anomaly in Central Europe.

In our paper, these regularities are described, as well as their connection to the polar vortex, which is the main factor in forming the mean sea level anomaly of the winter months of the northern hemisphere. In the last 29 years, clustering based on the mean sea level pressure anomaly for September has been able to divide significantly cold and mild December months even better than the state of the polar vortex in December (sign of the AO index).

In addition, a new phenomenon is presented, which might be a sign of climate change and has been interfering in the atmospheric processes since 2019.

Key-words: teleconnection, Arctic Oscillation (AO), polar vortex, temperature anomaly, mean sea level pressure (MSLP), Central Europe, climate change

1. Introduction

It is well known that a part of the inner variability of the climate system is not due to random fluctuations. Instead, these are caused by teleconnections, which are different anomalies mostly in a distance of thousands of kilometers but in a way connected to each other.

The best-known atmospheric oscillation phenomena are the El Niño-Southern Oscillation (ENSO) and the North Atlantic Oscillation (NAO), which are connected to anomalies of the sea surface temperature (SST) and the large-scale cyclic changes in mean sea level pressure (MSLP). NAO accounts for approximately one-third of the whole atmospheric variability (of temperature, precipitation, and so on) in the North Atlantic Region (*Marshall et al*., 2001).

A small part of long-distance connections has a prognostic value, i.e., in addition to spatial distance, temporal distance (lagged teleconnection) is also shown, so the connection can act as an anomaly predictor.

For example, the extent of the polar ice cover and the Eurasian snow cover can be predictors. The Eurasian snow cover anomaly in spring has been considered as one of the important factors affecting Asian summer monsoon variability. According to a study (*Liu* and *Yanai*, 2002), in the years of excessive Eurasian snow cover anomalies, cooling and a cyclonic circulation anomaly in the lower troposphere appear over the northern part of Eurasia, leading to a Rossby-wave-train-like circulation response, then to a weakened East Asian summer monsoon and deficient rainfall with an anticyclonic circulation anomaly south of Lake Baikal. Anomalies with opposite signs occur in the years of deficient snow cover. Another investigation (*Ye* and *Bao*, 2001) shows that winter snow depth over European Russia and central Siberia is associated with summer monsoon rainfall over southern and western India and eastern Pakistan, and sea-surface temperatures over the eastern and central tropical Pacific Ocean during the following winters. The connection is slightly stronger when snow depth over European Russia is above normal. The results of this study suggest that winter snow depth over the western rather than the eastern portion of Eurasia is critical to the Southeast Asian summer monsoon rainfall and eastern tropical Pacific SSTs during the following seasons.

Some of the teleconnections have a known physical explanation, while others have yet to be identified. According to a conceptual model (*Cohen et al*., 2007), when snow cover is above normal in the fall across Siberia, the diabatic cooling helps strengthen the Siberian high and leads to below normal temperatures. Snow-forced diabatic cooling in proximity to the high topography of Asia increases upward flux of wave activity from the troposphere, which is absorbed in the stratosphere. The strong convergence of wave activity flux leads to higher geopotential heights, a weakened polar vortex, and warmer temperatures in the stratosphere. Zonal mean geopotential height and wind anomalies propagate down from the stratosphere into the

troposphere all the way to the surface. Finally, the dynamic pathway culminates with strong negative phase of the Arctic Oscillation (AO) at the surface.

The cold equatorial Pacific SST anomalies generate weakened tropical convection and Hadley circulation over the Pacific, resulting in a decelerated subtropical jet and accelerated polar front jet in the extratropics (*Kim* and *Ahn*, 2015). The intensified polar front jet implies a stronger stratospheric polar vortex relevant to the positive AO phase; hence, surface manifestations of the reflected positive AO phase were then induced through the downward propagation of the stratospheric polar vortex. The results suggest that properly assimilated initial ocean conditions might contribute to improve the predictability of global oscillations, such as the AO, through large-scale tropical ocean–atmosphere interactions.

In an another study (*Yang et al.*, 2016), the authors suggest a connection between the November sea ice extent in the Barents and Kara Seas and the following winter's atmospheric circulation in terms of the fast sea ice retreat and the subsequent modification of local air–sea heat fluxes. In particular, the dynamical processes that link the November sea ice in the Barents and Kara Seas with the development of AO anomalies in February is explored. In response to the lower-tropospheric warming associated with the initial thermal effect of the sea ice loss, the large-scale atmospheric circulation goes through a series of dynamical adjustment processes: the decelerated zonal-mean zonal wind anomalies propagate gradually from the subarctic to midlatitudes in about one month. The equivalent barotropic AO dipole pattern develops in January because of wave–mean flow interaction, and firmly establishes itself in February following the weakening and warming of the stratospheric polar vortex. This connection between the sea ice loss and the AO mode is robust on time scales ranging from interannual to decadal. Therefore, the recent winter AO weakening and the corresponding midlatitude climate change may be partly associated with the early winter sea ice loss in the Barents and Kara Seas.

The atmospheric teleconnection presented in this paper – and referred to as September-December Teleconnection, SDT – shows a particularly strong regularity between the Euro-Atlantic mean sea level pressure anomaly pattern in September and the pattern three months later, in December, in the current positive AMO phase lasting since 1995.

We have not found a description of a teleconnection similar to the clustering-based method for forecasting air pressure, temperature, and AO index presented in this paper, either for Central Europe or for other regions of the world.

2. Data and methods

All the data used for the research (mean sea level pressure and surface temperature fields as well as time series of the AO index) are based on the NCEP/NCAR reanalysis (https://psl.noaa.gov/data/reanalysis/reanalysis.shtml) developed as a joint project between the National Centers for Environmental Prediction (NCEP) and the National Center for Atmospheric Research (NCAR). A state-of-the-art data assimilation system is used with a wide variety of weather observations to provide analyses of atmospheric parameters from 1948 up to recently. For calculations and visualization of results, the web application tool provided by NOAA (https://psl.noaa.gov/cgi-bin/data/composites/printpage.pl) was used.

The reference period for mean sea level pressure anomaly is 1991 to 2020, whereas surface temperature anomaly refers to the average of the period 1995 to 2022. The mean Central European surface temperature anomaly for December is calculated as the average of the grid point values within the area of 10° to 27.5° E and 45° to 55° N. This surface temperature anomaly average is shown on the top right side of the December maps, whereas relevant AO index values are shown on the left side (*Figs. 1–5*).

The AO index is constructed by projecting the monthly 1000 hPa geopotential height anomalies between 20° N and 90° N onto the first leading mode from the EOF analysis of the same parameter (https://www.cpc.ncep.noaa.gov/products/precip/CWlink/daily_ao_index/history/method.shtml). Monthly values of the AO index are calculated by NOAA and updated on a regular basis for a period from 1950 (https://www.cpc.ncep.noaa.gov/products/precip/CWlink/daily_ao_index/monthly.ao.index.b50.current.ascii.table).

The research is based on our own clustering of Euro-Atlantic mean sea level pressure anomaly fields for September for the period 1995 to 2023. Due to the small number of cases (only 29 years) and the mostly clearly distinguishable anomaly patterns, subjective clustering was applied focusing on the areas of Greenland, Scandinavia, and the British Isles.

3. Results and discussion

The following clusters were identified for the Euro-Atlantic mean sea level pressure anomaly for September. In the figures below, the mean sea level pressure anomaly pattern for September is presented for each year that belongs to the given cluster. The anomaly pattern for the corresponding December months is also shown.

3.1. Cluster H1

- Strong positive mean sea level pressure anomaly can be seen to the east, southeast, and south of Greenland and negative anomaly south of this area (*Fig. 1*)
- Septembers prior to the 6 coldest Decembers in Central Europe are in this cluster.
- September of 2021 and 2022 also belong to this cluster, which will be discussed later together with the years 2019 and 2020 of the cluster H2. (2021 is a borderline case due to a small area with negative anomaly within the larger area of positive anomaly in and around Greenland, which was followed by a December with mean temperature around average.)

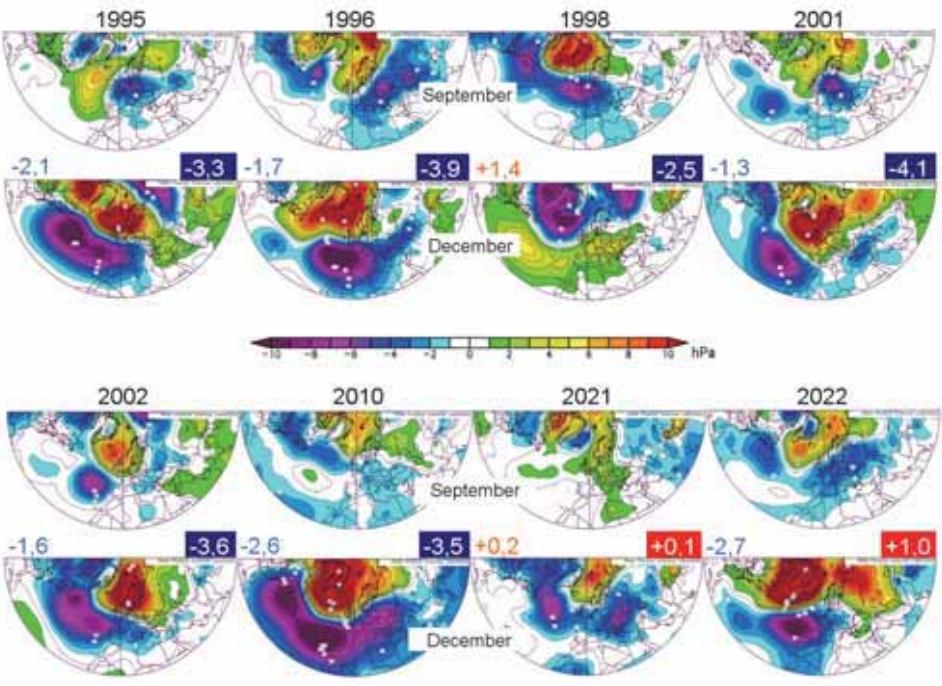

Fig. 1. Monthly mean sea level pressure anomaly of the years in cluster H1 for September and December (1995–2023), temperature anomaly in Central Europe in December compared to the average of the period 1995–2022 (°C, right), and AO index in December (left).

3.2. Cluster H2

- Strong negative anomaly can be seen in North Scandinavia, to the north of this area as well as between Scandinavia and Greenland, while significant positive anomaly occurs to the southwest and south (*Fig. 2*). (The year 2019 is a borderline case with the negative anomaly slightly more to the east and less significant positive anomaly. This September was followed by the mildest December of the cluster by far.)
- September months of the years with a negative temperature anomaly in December of less than 2 °C were all classified as members of this cluster.

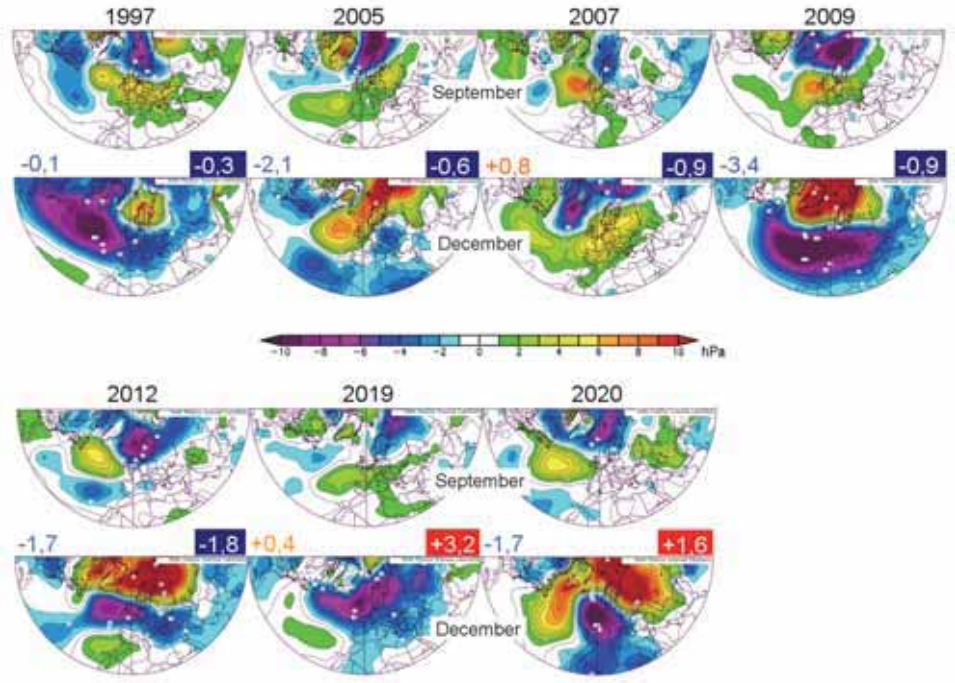

Fig. 2. Monthly mean sea level pressure anomaly of the years in cluster H2 for September and December (1995–2023), temperature anomaly in Central Europe in December compared to the average of the period 1995–2022 (°C, right), and AO index in December (left).

3.3. *Cluster E1*

- A ring-like band of positive anomaly is stretching from North America with an area of very strong negative anomaly over Greenland or to the east, southeast of that (*Fig. 3*).
- September months in this cluster were followed by moderately mild Decembers.

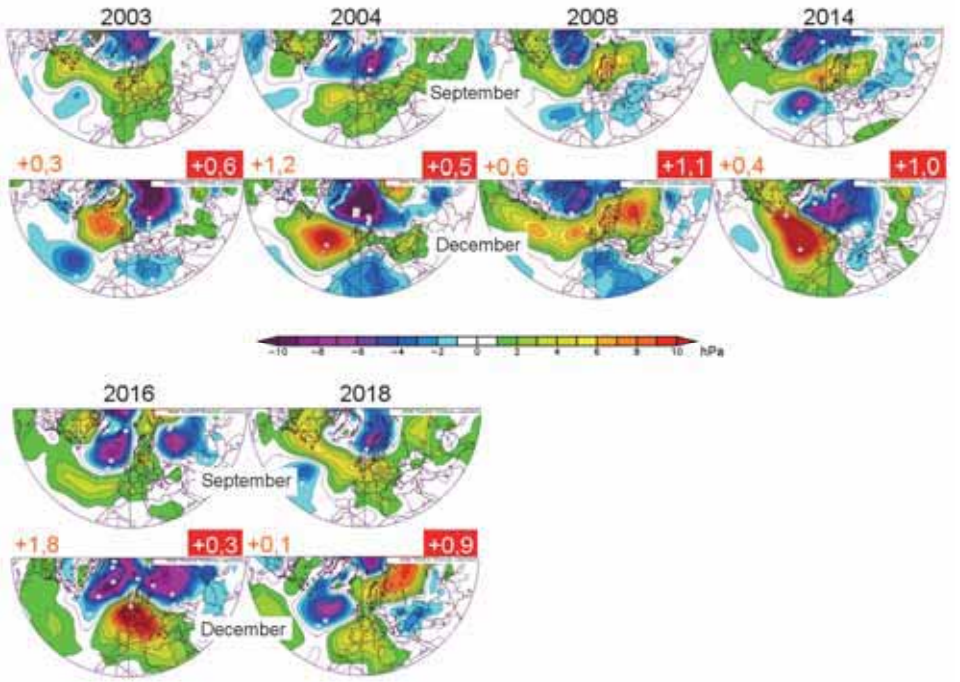

Fig. 3. Monthly mean sea level pressure anomaly of the years in cluster E1 for September and December (1995–2023), temperature anomaly in Central Europe in December compared to the average of the period 1995–2022 (°C, right), and AO index in December (left).

3.4. *Cluster E2*

- Positive anomaly is limited to Scandinavia and to the north of that region with negative areas to the south and near Greenland (*Fig. 4*).
- These are cases prior to December months with significantly positive temperature anomaly (over +1.5 °C).

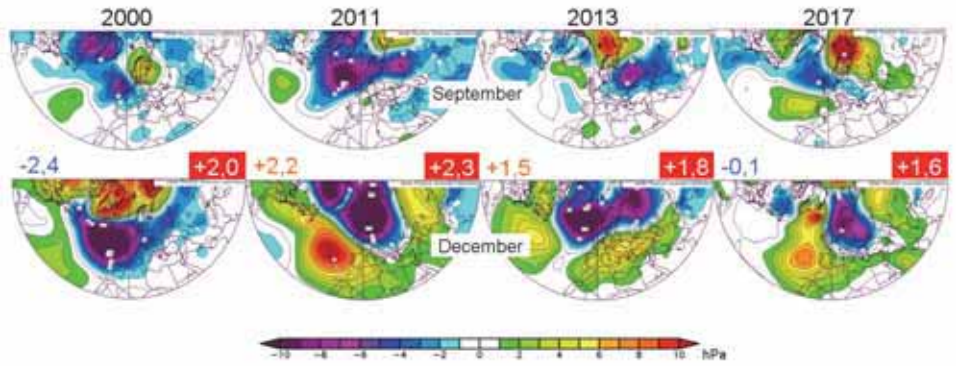

Fig. 4. Monthly mean sea level pressure anomaly of the years in cluster E2 for September and December (1995–2023), temperature anomaly in Central Europe in December compared to the average of the period 1995–2022 (°C, right), and AO index in December (left).

3.5. Cluster N

Four September months could not be classified as any of the 4 mentioned clusters (*Fig. 5*).

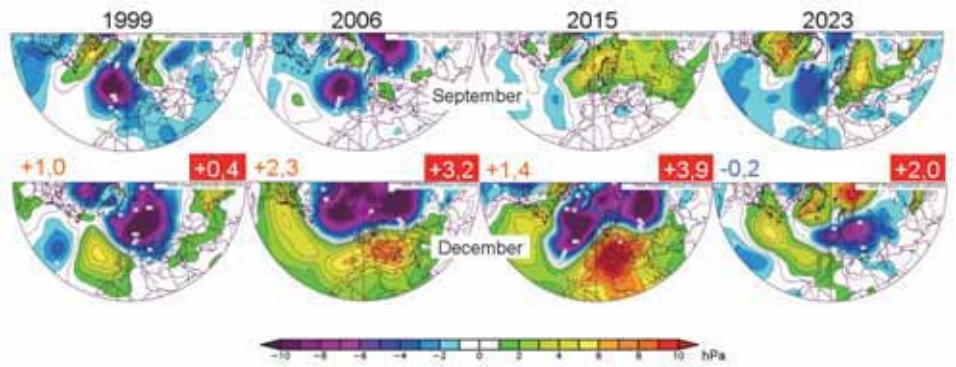

Fig. 5. Monthly mean sea level pressure anomaly of the years in cluster N for September and December (1995–2023), temperature anomaly in Central Europe in December compared to the average of the period 1995–2022 (°C, right), and AO index in December (left).

3.6. Similarity of the years 1996 and 2021 in cluster H1

In case of two years belonging to cluster H1, 1996 and 2021, the similarity of the mean sea level anomaly pattern between the two years lasted even for a period of a whole year starting in May, stretching to April next year (*Fig. 6*). Without the existence of teleconnections, such a similarity at half-hemispheric level for a whole year would not be possible.

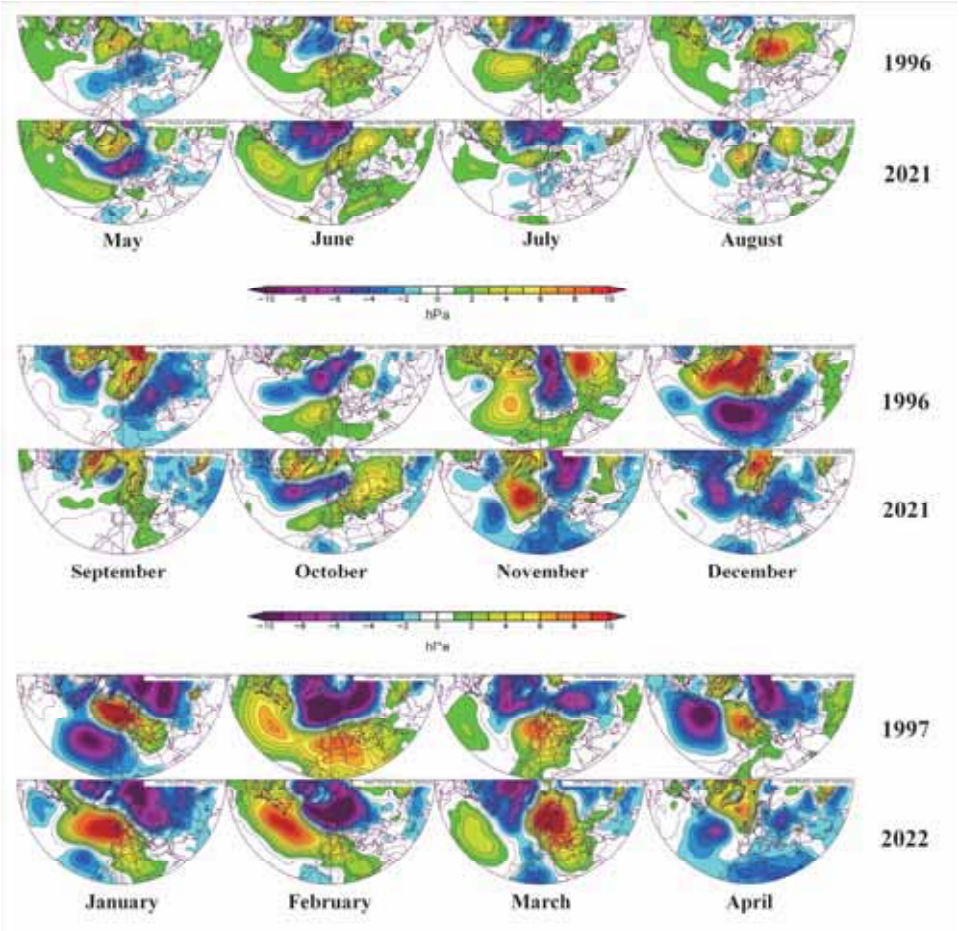

Fig. 6. Monthly mean sea level pressure anomaly in 1996/97 and 2021/2022 from May until April.

3.7. Connection of SDT with the polar vortex and the AO index

The AO index is an important measure of the state of the polar vortex, which is responsible for the winter temperature anomaly of the northern hemisphere to a high degree (*Cohen et al.*, 2007; *Kennedy* and *Lindsey*, 2014). In case of a strong polar vortex (significantly positive AO index), cold air is not able to frequently reach lower latitudes (also Central Europe) in larger quantity in the winter period, due to the fact that it is locked in the arctic region by the vortex. In this case, our region is also characterized by temperature conditions mostly above average. When the arctic low pressure is weak (significantly negative AO index), cold air can more often burst from the arctic region towards the south by the more frequent wave development on the polar jet stream, leading to longer lasting cold winter weather in Europe, North America, and also in Asia.

The clusters classified based on the mean sea level pressure anomaly in September in the Euro-Atlantic region predicted the state of the significantly weak or strong polar vortex with high accuracy (*Fig. 7*): 10 of the 11 Decembers with an AO index of under -1 belong to cluster H1 or H2, but only 1 of the 7 cases with an AO index of over +1 belongs to these clusters.

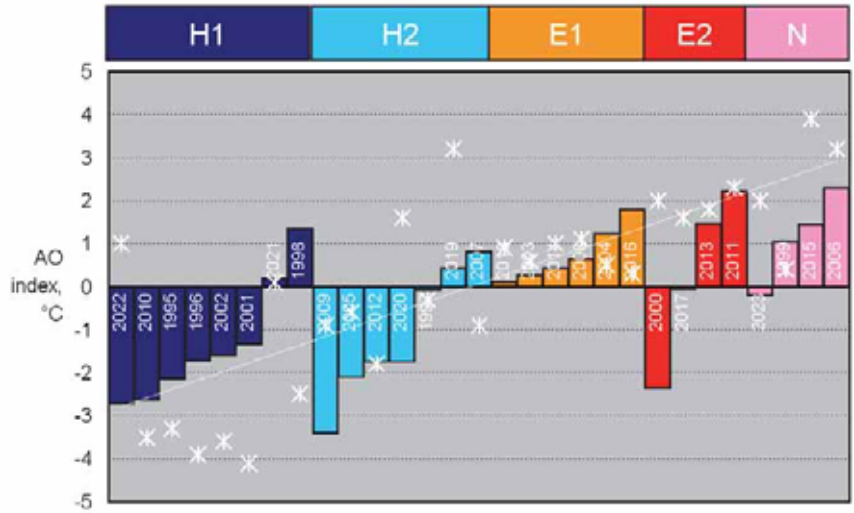

Fig. 7. Monthly AO index values (colored) and temperature anomalies (white) of the December months in Central Europe in each cluster (1995–2023)

Fig. 8 showing mean sea level pressure anomaly distribution averaged for September and December in each cluster provides an expressive explanation of

the results presented above: in clusters H1 and H2, strongly positive mean sea level pressure anomaly can be found over the arctic in December, whereas clusters E1 and E2 show strongly negative anomalies over the mentioned region.

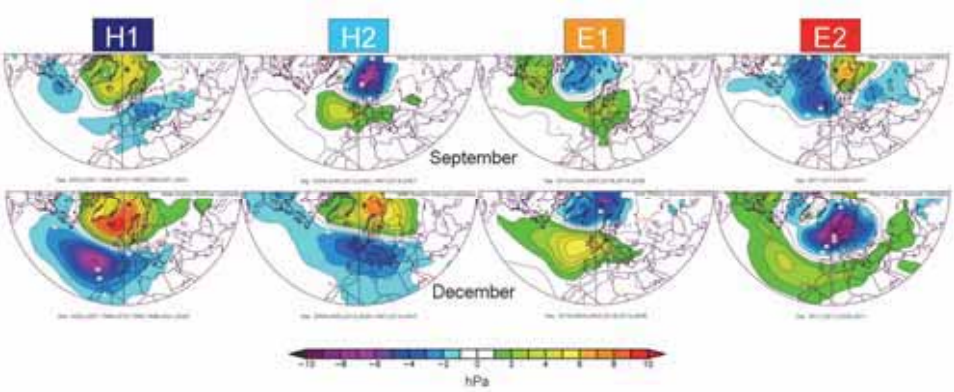

Fig. 8. Mean sea level pressure anomaly distribution averaged for September and December in each cluster (1995–2023).

Mean sea level pressure anomaly distribution averaged for all December months with a negative AO index (*Fig. 9*) strongly resembles to that of the clusters H1 and H2 (*Fig. 8*).

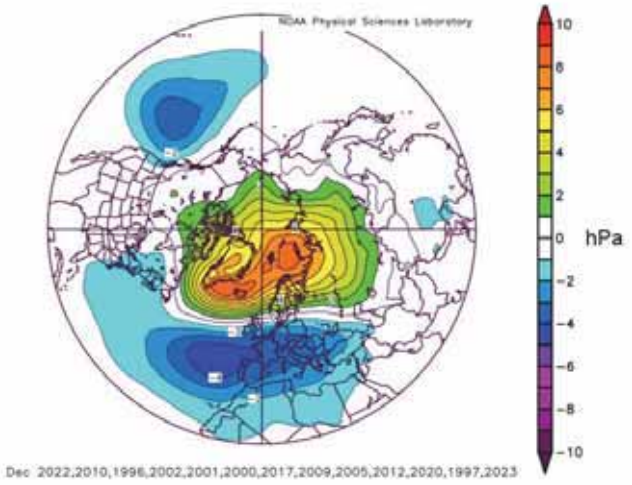

Fig. 9. Mean sea level pressure anomaly distribution averaged for all December months with a negative AO index (1995–2023).

Since 1995, 6 of the 7 December months with a negative temperature anomaly exceeding 1 °C in Central Europe have been accompanied with a negative AO index. Meanwhile, 4 of the 9 December months with a positive

temperature anomaly exceeding 1 °C were also characterized by a negative AO index. Consequently, a weaker than average polar vortex is, apart from some exceptional cases, a necessary but not at all sufficient condition for a cold December in our region. The explanation for that is that cold bursts from the arctic might not hit Central Europe (mostly affecting North America or the Atlantic in these cases), leading to a mild December in our region. **In the last 29 years, clustering based on the mean sea level pressure anomaly for September has been able to divide significantly cold and mild December months even better than the state of the polar vortex in December (sign of the AO index) with 7 of 7 months and 5 of 7 months in the right cluster (not regarding cluster N), respectively.**

3.8. A new phenomenon: mysterious depression in December over the British Isles and Scandinavia

An unpleasant experience of recent years was that although the clustering provided a good prediction of the large scale mean sea level pressure anomaly, the December was mild in Central Europe instead of the cold expectations between 2019 and 2022. An appropriate mean sea level pressure anomaly forecast on global scale with a relatively good prediction of the location of positive and negative anomalies might of course lead to regional effects in temperature conditions contrary to expectations, however, in 4 consecutive years?

The explanation can be found in *Fig. 10*. Since 2019 there has been a new phenomenon over the British Isles and Scandinavia in December: significantly negative mean sea level pressure anomaly for 4 years compared to the average of their respective clusters. This led, contrary to expectations, to mild December months between 2019 and 2022 in Central Europe and also in most parts of the continent by modifying the mean sea level pressure pattern in a sensitive area. In 2023, the relation to the cluster average could not be investigated since this September was unclassifiable (Cluster N), but mean sea level pressure was again well below average, and the area of negative anomaly over the continent seems to have merged with that over the British Isles (*Fig. 5*).

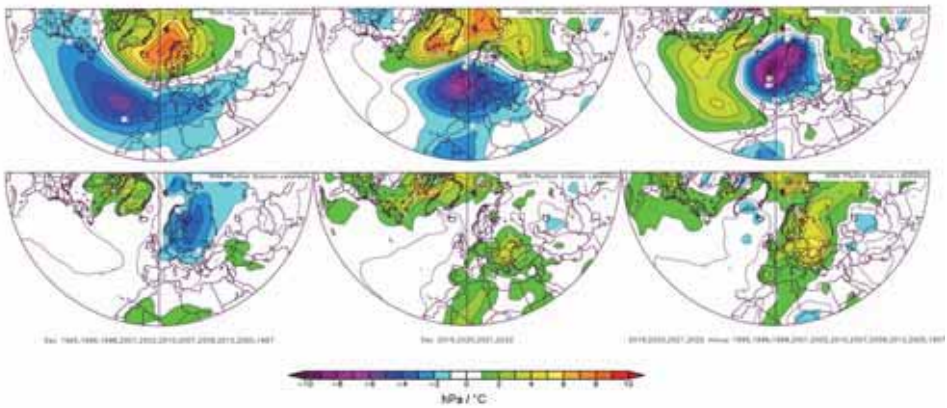

Fig. 10. Mean sea level pressure anomaly averaged for December of the cases in cluster H1 or H2 before 2018 (11 cases, left above), after 2018 (4 cases, in the middle above), their difference (right above), and relevant temperature anomalies (below).

Increase in the strength and the number of low-pressure systems, modification of their tracks in the region of the British Isles and Scandinavia might be another consequence of climate change, which is excellently illustrated by *Fig. 11*. A new climate regime seems to have started in 2019 in Central Europe regarding temperature anomaly for December. Before 2019, there was no overlapping in temperature anomaly values of December months following September months in different clusters: cases of cluster H1 were in the range of -2 to -4 °C, in 0 to -2 °C for cluster H2, in 0 to +1 °C for cluster E1, and in +1.5 to + 2.5 °C for cluster E2. These bands seem to have been increased by 3 to 4 °C after 2018.

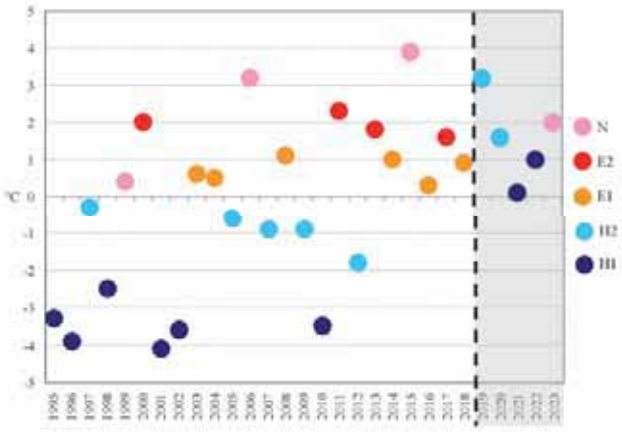

Fig. 11. Temperature anomaly for December in Central Europe between 1995 and 2023 colored as a function of the clusters

4. Summary and conclusions

The September-December Teleconnection (SDT) shows particularly strong regularities in the current positive AMO phase lasting since 1995, which makes it possible to divide years into clusters.

With the help of the clustering based on the mean sea level pressure anomaly in September in the Euro-Atlantic region, the state of the polar vortex in December can be predicted. September months in clusters of the type H are followed by December months with a negative AO index, those in clusters of the type E by December months with a positive AO index with an accuracy of nearly 90% for the significant cases. On the other hand, a forecast for the sign and strength of the temperature anomaly in Central Europe can be provided in most cases.

However, a new phenomenon has turned up, possibly connected to climate change. Since 2019, a strong negative mean sea level pressure anomaly can be found over the British Isles and Scandinavia for the cases in clusters H1 and H2 compared to their former cluster average. This could make our prime goal, forecasting the temperature for December in Central Europe, more difficult or in other cases, paradoxically even easier.

Acknowledgements: The authors thank for data/images provided by the NOAA/OAR/PSL, Boulder, Colorado, USA, from their Web site at https://psl.noaa.gov/.

References

Babolcsai, Gy. and *Hirsch, T.,* 2019: Teleconnection between mean sea level pressure in the North Atlantic for September, the AMO phase and mean temperature in Central Europe for December (1896–2015). *Meteorol. Appl. 26*, 267–274 https://rmets.onlinelibrary.wiley.com/doi/full/10.1002/met.1760

Cohen, J., M. Barlow, P.J. Kushner, and *K. Saito*, 2007: Stratosphere–troposphere coupling and links with Eurasian land surface variability. *J. Climate 20*, 5335–5343. https://doi.org/10.1175/2007JCLI1725.1

Kennedy, C. and *Lindsey*, R., 2014: How is the polar vortex related to the Arctic Oscillation? https://www.climate.gov/news-features/event-tracker/how-polar-vortex-related-arctic-oscillation

Kim, H.-J. and *Ahn, J.-B.*, 2015: Improvement in Prediction of the Arctic Oscillation with a Realistic Ocean Initial Condition in a CGCM. *J. Climate 28*, 8951–8967. https://doi.org/10.1175/JCLI-D-14-00457.1

Liu, X. and *Yanai, M.,* 2002: Influence of Eurasian spring snow cover on Asian summer rainfall, *Int. J. Climatol 22*, 1075–1089. https://doi.org/10.1002/joc.784

Marshall, J., Kushnir,Y., Battisti, D., Chang, P., Czaja, A., Dickson, R., McCartney, M., Saravanan, R., and *Visbeck, M.*, 2001: North Atlantic climate variability: phenomena, impacts and mechanisms. *Int. J. Climatol 21*, 1863–1898. https://doi.org/10.1002/joc.693

Yang, X.-Y., Yuan, X., and *Ting, M.*, 2016: Dynamical Link between the Barents-Kara Sea Ice and the Arctic Oscillation. *J. Climate 29*, 5103–5122. https://doi.org/10.1175/JCLI-D-15-0669.1

Ye, H. and *Bao, Z.*, 2001: Lagged teleconnections between snow depth in northern Eurasia, rainfall in Southeast Asia and sea-surface temperatures over the tropical Pacific Ocean, *Int. J. Climatol 21*, 1607–1621. https://doi.org/10.1002/joc.695

DOI:10.28974/idojaras.2025.3.3

IDŐJÁRÁS

Quarterly Journal of the HungaroMet Hungarian Meteorological Service
Vol. 129, No. 3, July – September, 2025, pp. 279–306

Cold-air pool development and covariance analysis of the measured meteorological parameters in the Mohos sinkhole, Bükk Plateau, Hungary

András Dobos*, **Réka Farkas**, and **Endre Dobos**

Department of Geography and Geoinformatics
University of Miskolc, Miskolc, Hungary

**Corresponding Author e-mail: dobosbandi@hotmail.com*

(Manuscript received in final form August 6, 2024)

Abstract— It is a well-known phenomenon that sinkholes, compared to their environment, have a relatively colder microclimate, due to the topographic conditions (closed depressions). Its geomorphological characteristics favors the development of cold-air pools and can cause significant temperature anomalies. This process has been documented in several papers before, but the detailed buildup and breakup, and especially the environmental covariates that drive these processes, are not well documented yet. This paper aims to summarize a three months period measurement (spring of 2023) in Northern Hungary, on the karst plateau of the Bükk Mountains. This plateau is characterized with a complex karst surface development, having interconnected sinkhole systems. The Mohos sinkhole – the largest sinkhole of the area with several contributing smaller sinkholes – was selected for the measurement campaign. A detailed terrain and remotely sensed database were built to characterize the geomorphology and its contribution to the development of the sinkhole's microclimatic system. A sensor system was developed and adopted to the local conditions using 10 directly measured or derived meteorological parameters (air temperature (200 cm, 40 cm), dew point, solar radiation, relative humidity, wind speed, daily evapotranspiration, vapor pressure deficit., and soil temperature), along with two comparison sites from the edge of the sinkhole and from a representative site of the Bükk Plateau, where no major microclimatic derivation factor was assumed. During this period, the Carpathian Basin was characterized by a significant variability of weather patterns, and was optimal to analyze the behavior of the sinkhole's microclimate system based on the regional weather trends and their atmospheric dynamics. Several temperature inversion events were developed and analyzed to describe the relationships between the cold-air pool development and the external meteorological affects. The events were classified into the commonly accepted categories. The results demonstrated that the time of the lowest recorded temperatures was partly independent from the general temperature regimes. The most important factors are the general geomorphological factors, favorable radiation

conditions, and lack of any external physical disturbance. It was also proved that the soil temperature had the largest correlation with the temperature change (r = 0.95), followed by the dew point (r = 0.92), vapor pressure deficit (r = 0.85), wind speed (r = 0.83) and the relative humidity (r = -0.8). That was also documented, that the near-surface dynamics play an important law in the behaviors of the sinkhole microclimate system, thus the buildup and breakup of the cold-air pool.

Key-words: closed basins, cold air, cold-air pool, microclimate, mountain plateau, radiation, sinkhole, temperature inversion, weather dynamics

1. Introduction

In limestone plateau environments, the process of dissolution creates various karst formations, such as sinkholes without outflow (*Hevesi*, 2002). As a result of their concave geometry, the colder, denser air masses converge towards the deepest points (the bottom of the sinkholes), where they are layered inversely. Sinkholes are characterized by a specific microclimate that is colder than their environment, if the conditions for the development of a cold-air pool are given. The operation of microclimate systems in sinkholes are influenced by the topographic factors, surface/land coverage, and atmospheric conditions. The karst plateau of the Bükk Mountains is rich in well-developed sinkholes, which are located between 650–850 m above sea level (located at lower elevation than most of the sinkholes examined in the international literature). With a normal temperature gradient, this altitude generates a cool mountain climate in the Carpathians that is considered cool in the low-average-altitude Carpathian Basin, although it is warmer than the climate of the broader Carpathian region.

However, due to their special microclimate, the sinkholes of the plateau can be characterized by a significant negative temperature anomaly at a regional level. The largest sinkhole on the Bükk Plateau (Hungary) is the Mohos sinkhole (furthermore: MS), where the Institute of Geography and Geoinformatics of the University of Miskolc began measurements in July 2022. The aim of the research is to quantify the climate trends of the sinkhole's microclimate system during long-term data collection and to provide information through case examples on the effects of various atmospheric events, surface coverage, and microtopographic factors on the temperature inversion inside the Mohos sinkhole. The article summarizes the results of the measurement of the spring, 2023. The analysis of the case examples takes into account the current weather conditions, whereas the measured data provide a complex representation of the processes occurring in the bottom of the sinkhole that affect the different air layers and their temperature.

The topographic conditions and different weather events play a decisive role in the formation, development, and breakup of the near-surface inversion that occurs in sinkholes. The meteorological and topographic conditions affect temperature inversion, and the microclimate generated by sinkholes shapes the

spatial and temporal development of the temperature inversion and influences the quality of the inversion buildup (*Whiteman* and *McKee*, 1982; *Dorninger et al*., 2011; *Dobos and Dobos*, 2023).

In the past, for more than 30 years, many measurements have been made worldwide, with the aim of gathering information about the daily evolution of the cold-air pool (*Aigner*, 1952; *Sauberer and Dirmhirn*, 1954; *Geiger*, 1965; *Whiteman*, 1990 and *Eisenbach et al*., 2003).

Findings concerning the strengthening and inhibiting factors, buildup and breakup periods, and the main characteristics of temperature inversion were elaborated as well. Usually, valleys or basins are the areas where temperature inversions are common. However, there was a methodological problem in the case of the examination of the microclimate in terms of the development of the daily wind pattern in primary form assets, such as larger basins and valleys. The downslope wind can affect the inverse air stratification before the local changes in the inflow and outflow conditions, thus influencing its natural evolution (*Pospichal et al*., 2003; *Steinacker et al*., 2007; *Salavec*, 2012). To have a better understanding, attention was directed towards the local, concave karst formations without outflow, that slope towards one point from all directions, namely the sinkholes (*Steinacker et al*., 2007).

The sinkholes also known as dolines, are well separated from the flow systems of their environments, so a specific microclimate can develop in them. The most characteristic feature of the typical microclimate of the sinkholes is the tendency for temperature inversion, which results in unambiguously low daily minimum temperature (hereafter Tmin) values compared to their surroundings (*Clements et al*., 2003; *Steinacker et al*., 2007).

The microclimate of the sinkholes, the interpretation of the measured temperature curves at different heights above the surface, and the direct and indirect factors affecting them have been partially understood through several periodic and permanent experiments and long-term studies. In fact, the absolute Tmin value in Central Europe was recorded at the limestone plateaus of the Eastern Alps, specifically in the Grünloch sinkhole, where a temperature of -52.6 ℃ was measured in 1932 (*Aigner*, 1952; *Sauberer* and *Dirmhirn*, 1954; *Eisenbach et al*., 2003, *Pospichal et al*., 2003). Another prominent example is the ‘Peter Sinks’ sinkhole in Utah in North America, which, due to its special location and dimensions, is studied extensively by meteorologists’ community (*Clements et al*., 2003; *Steinacker et al*., 2007; *Utah Climate Center*).

Within the climate system of karst mountains, there are microclimate systems, which formed due to the orographic condition and are capable of modifying the effects of solar radiation (shortwave), emission (longwave), and flow conditions (*Whiteman et al*. 2004). The Bükk Plateau sinkholes are typically sinkholes created by dissolution that, thanks to their specific topography, are able

to create unique, separate, tertiary (*Wagner*, 1964) microclimate locations by sinking into the surface of the karst plateau or into the dry valleys (*Keveiné Bárány*, 2011).

In Hungary, research on the microclimate of the Bükk Plateau's sinkholes began during the Austro-Hungarian Monarchy, with the aim of instrument calibration (*Dobos*, 2023). Until 2009, only periodic measurements were carried out on the plateau (*Bacsó* and *Zólyomi*, 1934; *Wagner*, 1954; *Keveiné Bárány*, 2011). Since 2009, a group of amateur meteorologists (by the lead of Róbert Kerékgyártó) have been operating a permanent monitoring network in some sinkholes (e.g., Vörösmeteor sinkhole) and in control points. The meteorological station of the University of Miskolc located in the Mohos sinkhole is the newest member of the Bükk Plateau monitoring system; it gathers data at a gap-filling location (*Dobos et al.*, 2024).

The factor which influences most the developing of cold-air pools are the external meteorological affects (wind and cloud), which can erode the partly built-up temperature inversion (*Dorninger et al*., 2011). Furthermore, the microclimate system of the sinkholes are also influenced by surface coverage, which determines the sky-view factor as well (*Whiteman et al*., 2004; *Zhang*, 2005; *Mackiewicz*, 2012). The less forested, open landscape has higher cumulated sky-view factor, with generally higher surface albedo, compared to the forested ones (*Bacsó* and *Zólyomi*, 1934; *Lehmann*, 1970). Therefore, the vegetation coverage within the system and its direct surroundings is considered the principal factor of the microclimate system. Inside the sinkhole, vegetation adjusts to the decrease in average temperature and to the aspect. The inversed layering of the vegetation is typical. Starting from the bottom of the sinkhole, where cold-tolerant communities are present, within small area a sharp change can be observed, and the vegetation gradually transforms into the regular communities which can be found at the given area, thus moving upwards the inversed vegetation moves towards normalization (*Horvat*, 1952; *Egli*, 1991; *Özkan et al.*, 2010; *Bátori et al.*, 2014a,b).

Snow covering changes the albedo, meaning that its effect on the sinkholes microclimate system is significant. Seasonal snow coverage results in noteworthy difference in the inversions temperature curve and dynamics that develops under similar atmospheric conditions. In addition, snow coverage highly affects the temperature of near-surface soil that is most exposed to atmospheric conditions. The extent of correlation between air and soil temperature decreases with the increase in snow thickness (*Goodrich*, 1982; *Thorn et al.*, 1999; *Beltrami*, 2001; *Sokratov and Barry*, 2001; *Decker et al.*, 2003; *Dobos*, 2024).

2. Materials and methods

2.1. Pilot area description

The investigated area includes the southern third part of Zsidó meadow (Bükk Plateau), the Mohos sinkhole and the contributing area to its microclimatic scope. The MS is the largest sinkhole, of the plateau having an area of 51.097 m². It is located in the Bükk Mountains, which are part of the of North Hungarian Mountains range and can be characterized as the southernmost member of the Northwestern Carpathians (*Kocsis*, 2018). The study area is located in the southwestern part of the platean – located at the southern edge of the northern part of the Bükk. Its elevation exceeds 900 m elevation (*Fig. 1*).

2.2. Data collection methodology

The data measured according to the meteorological standards are intended to ensure the global comparability and interpretability. An automatic meteorological station (iMETOS 3.3 with its default sensor set) was installed at the deepest point of the Mohos sinkhole. The station records the measured meteorological parameters at 2 m above the surface and the soil temperature (hereafter T(s)) at -5 cm. The logging interval is 10 minutes, during which time the instrument continuously collects measurements, so the average, minimum, and maximum values of the 10-minute interval are transmitted to the receiving side. The parameters measured and calculated by the station are the following (based on product portfolio of iMETOS): air temperature (°C, precision: ±0.8 °C), dew point (°C, ±0.3 °C), solar radiation (J/m², calibration against Kipp & Zonen CMP3 under daylight, abs. error max. 5%, typically 3%), vapor pressure deficit ((VPD) kPa, calculated), relative humidity (%; precision 0–80%: +/-2%; precision 80–100%: ±3%), precipitation (mm, resolution: 0.2 mm), wind speed (km/h, threshold: 1.1 m/s), daily evapotranspiration ((ETO) mm, calculated), and soil temperature (°C, ±0.1 °C), complemented with data related to the status of the station. The station transmits the measured data via a mobile network to the FieldClimate website.

The meteorological station iMETOS 3.3 has been placed in the following position in the bottom of the Mohos sinkhole: longitude (WGS1984): 20.463171, latitude (WGS1984): 48.065424, altitude (height of data recording): 825,5 m a.s.l.

The control measuring points (temperature data loggers, installed with a radiation shield in 2 m above the surface) are placed in the following altitude: K1 control point: 888 m, K2 control point: 855 m (see in Section 3.3). Control measurements are taking place in the Mohos sinkhole with the reason to determine the proportion of the air temperature (T) anomaly caused by thermal inversion.

Aside from the permanent monitoring location at the bottom of the MS (at the altitude of 825.5 m, centrum point of cold-air pool developing), there are two control points to provide reference data. Point K2 (855 m) is temporary, it is

located in the eastern outline of the MS (characterized by significant potential of temperature inversion by the model Cold Air Flow (*Schwab,* 2000)). Point K1 (888 m, without potential of temperature inversion by the model Cold Air Flow) is located on the northern side of the Bükk Plateau, at a mountain saddle formation, at Bánkút (*Fig.1*). The elevation difference between points MS and K2 is approximately equal to the difference between points K1 and K2.

In the case of the sinkhole's microclimate, it is also important to know the temperature of the air layers near the surface, so a temperature data logger was installed at 40 cm above the surface onto the meteorological station at the bottom of the sinkhole. The Voltcraft DL-240k data logger is calibrated at the factory; its measurement resolution is ±0.1 °C with ±1 °C accuracy. In order to record possible short-term events, the sensor operated with a 5-minute data recording interval. Such events can take place in the near-surface air flow system of the sinkhole, which are not always detectable at 2 m. The temperature data were recorded and processed on a °C-based scale.

The necessary data for building the digital surface model were collected on site with UAV survey. Georeferenced aerial images in the RGB+Infra range spectrum were taken with DJI Mavic 2 and 3 drones, which flew into the area specified in advance for the authorities. The records were processed with online software called PIX4D Cloud, from which a digital surface model (DSM), orthomosaics, 3D mesh, and point cloud were derived and downloaded.

3. Results

3.1. Delineation of the research area

Fig. 1, shows the digital elevation model (I., DEM) of the Bükk Plateau with the potential areas of cold-air pool within the control points, the digital surface model (II., DSM) and the orthomosaic (III.) image of the sinkhole and its contributing area.

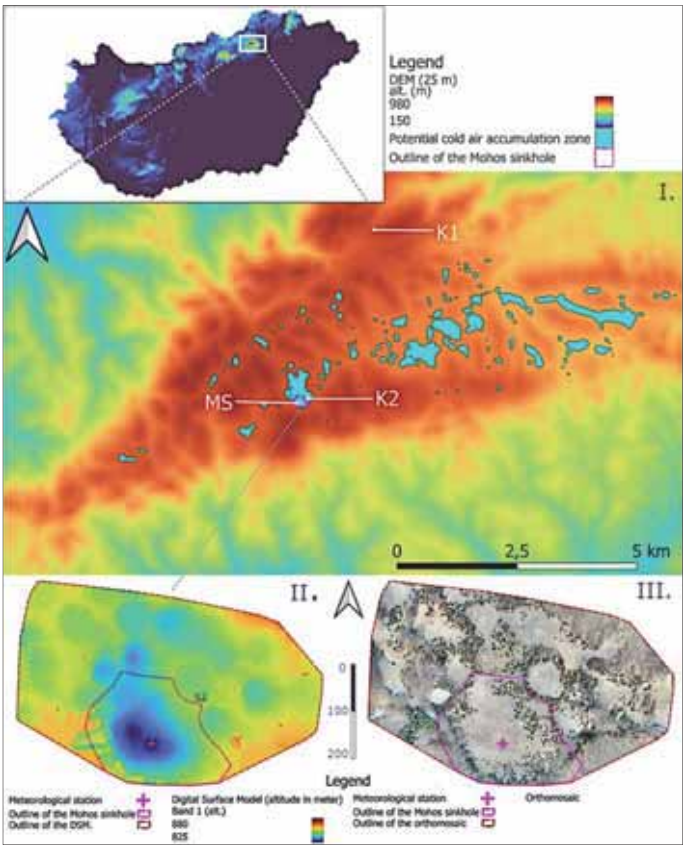

Fig. 1. I.: The location of the control points in the DEM (25 m resolution) of Bükk Plateau and its environment. The blue polygons with a black outline mark the potential areas of the cold air accumulation, calculated by SAGA GIS, tool Cold Air Flow. The Mohos sinkhole meteorological station is marked by MS (centrum area of cold air depositing, place of the meteorological station), the two control points are marked by K1 (area without significant inversion potential) and K2 (outline of the Mohos sinkhole). II.: The high resolution (2.7 cm) digital surface model (DSM) and III.: the orthomosaic of the research area. The broken red line marks the outline of the research area and the dashed pink line marks the outline of the Mohos sinkhole (ridge between the sinkholes). Text K2 in a DSM (left) marks the point of the control measurement (*Dobos*, 2023).

3.2. GIS analysis of the topographic environment of the Mohos sinkhole

The double base and protruding depth of the MS are visible in the southern quarter of *Fig. 1*. Next to it, a number of smaller sinkholes can be seen in the NW and NE directions from the sinkhole. The darker colours of the DSM image represent the double base of the Mohos sinkhole. The protection of the cold-air pools is capacitated by the double bottom of the sinkhole. The most significant elevation decrease begins in the vicinity of the bottom of the sinkhole with the lowest radiation potential within the sinkhole. With the exception of the surrounding steeper slopes around the bottom of the sinkhole, we encounter surfaces with a

much lower slope angle whose confluence point is the bottom itself (moderate blue in *Fig. 1*).

Thus, within the contributing area of the MS, which is most affected by the tertiary microclimate (*Wagner*, 1964; *Keveiné Bárány*, 2011), the less steep, more open-to-the-sky surfaces represent an area with good potential radiation (longwave emission) and high energy loss. The cold air, generated near the surface moves to the direction of the more protected sink bottom and accumulates in an inversely layered manner in the relatively steep twin base, which flattens out again at the bottom (*Fig. 2*).

Accordingly, the sinkhole has a sufficiently high, summarized 'sky-view factor' (index-number referring to the surface exposure to the sky), yet it is able to provide a more protected space for the buildup of the cold-air pool (*Whiteman et al.*, 2004). Due to the geometry of the MS and its surroundings, the microclimate resulting from emitted heat loss provides a favorable environment for the development of relatively low temperature values compared to the surrounding area. The orthomosaic shows that the vegetation also outlines the contours of the dolinas. The vegetation zone inversion, which is typical of larger sinkholes (*Pospichal et al.*, 2003), can also be observed in the Mohos sinkhole (*Figs. 1* and *2*).

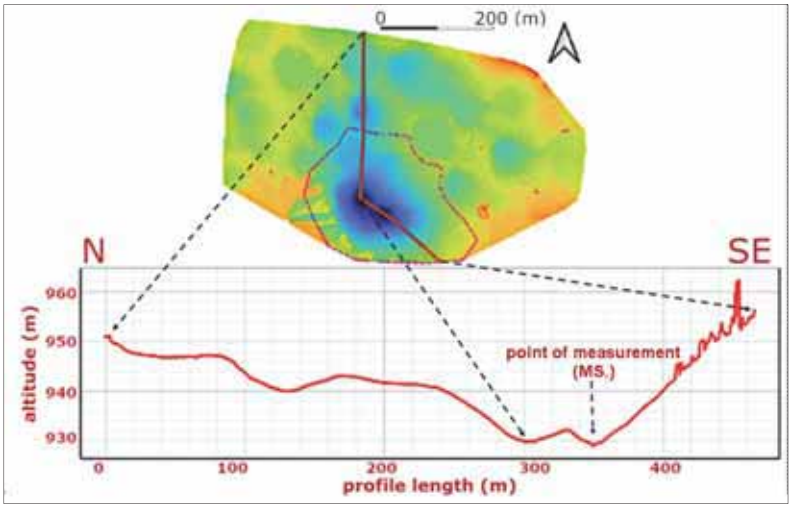

Fig. 2. The elevation (surface) profile (in meter) of the bottom line (from N to SE) of Mohos sinkhole and the environments flow system (marked by a red line across the DSM). The elevation profile was calculated from the DSM's surface, thus it also shows the vegetation on the upper part of the sinkhole's slope (*Dobos*, 2023).

3.3. Control measurements

For comparison, 7 cases were chosen randomly from the periods when thermal inversion was present at the MS. During these 7 cases the average difference of MS and K2 point was 7.4 °C, while the average difference (calculated from the 7 days) of MS compared to the control point K1 was 13.8 °C (*Table 1*). The differences between the MS and K1 (p=0.0016) and the MS and K2 (p=0.04) were statistically significant. The recorded control values unambiguously confirm the negative temperature anomaly of the Mohos sinkhole in the Zsidó meadow. Moreover, they clearly represent the milder temperature nature compared to the MS, and the definitely present cold temperature anomaly of the Zsidó meadow, compared to the areas not characterized by significant temperature inversion tendencies, but located at a similar elevation (K1).

Table 1. Minimum temperatures (daily Tmin) of the Mohos sinkhole (MS) and control stations and their differences on randomly chosen representative days. The data collection happened in 2 meter above the surface by the same methodology

Altitude	825.5 m	855 m	888 m			
Date of measurements	MS daily Tmin (°C)	K2 daily Tmin (°C)	K1 daily Tmin (°C)	MS dif. compared to K2 (°C)	MS dif. compared to K1 (°C)	Snow cover (cm)
January 9, 2024	-22.31	-15.7	-9.4	-6.61	-12.91	2–4
January 10, 2024	-22.95	-16.3	-8.6	-6.65	-14.35	2–4
January 11, 2024	-21.14	-13.8	-6.1	-7.34	-15.04	2–4
April 13, 2024	-6.26	0.7	9.1	-6.96	-15.36	no
April 21, 2024	-13.7	-6.1	-0.3	-7.6	-13.4	no
April 26, 2024	-12.39	-4.9	-0.7	-7.49	-11.69	no
May 10, 2024	-7.64	1.4	6.3	-9.04	-13.94	no
			average difference: (°C)	-7.38	-13.81	

3.4. Meteorological summary

Information on the regional weather trends of the investigated period is important to interpret the resulted values measured in the MS. The spring of 2023 included alternating, significantly warmer and colder periods compared to the average, and the average temperature rarely adjusted to the long-term average. Overall, the entire

investigated period can be characterised as having temperatures close to average or slightly below the average. Based on the measurement network of the Hungarian Meteorological Service (HungaroMet, 2023a) March brought above-average temperatures (<+1.5 °C) and precipitation in the northeastern region of Hungary. The lowest temperature was -9.2 °C (HungaroMet, 2023a, Zabar, at 4th and 17th of March). April brought below-average (<-2 °C) temperatures and above-average precipitation, while May had a negative temperature anomaly of -1 °C and slightly below-average precipitation. The T-min. recorded by the national official monitoring system in April was -7.8 °C (HungaroMet, 2023b, Kékestető, at 5th of April), while in May, it was -1.9 °C (Hungaromet, 2023a, Zabar, at 9th of May).

3.5. Data processing of the Mohos sinkhole meteorological station for the period March 1 – May 31, 2023

Data from the entire examined period are illustrated in *Fig. 3*. Periods that are colder than the national average do not always cause below-average, 'egregiously' cold temperature values in sinkholes. The development of the cold-air pools and Tmin values that are considered low in the given environment, are the necessary conditions for heat radiation to be present. These conditions are clear sky and wind lull. Periods characterized by nationally and regionally measured negative temperature anomalies are often linked to highly dynamic meteorological events, such as weather fronts. In this case, in addition to the homogenizing wind that prevents inversion, cloudy and rainy weather is also typical. A good example of this is the period of April 1–11, when there was a stable negative temperature anomaly nationally and regionally for a long time, but despite the low dew point, the atmospheric dynamics did not allow the sinkhole's microclimate system to prevail. So, the cold-air pool could only develop for a short time, causing a relatively small daily temperature fluctuation. The period May 15–20 is an example for a similar event (*Fig. 3*).

Apart from the sinkhole's microclimate and its environment's low temperature values, the existence of the radiation conditions is more important than the anomaly towards which the regional weather is moving in the long-term average. As an example, the period of March 1–5 can be mentioned. This period had minimum values below -10 °C each day, and the daily Tmin value dropped below -15 °C four times, which resulted in slightly above-average national and regional anomalies. On March 5, a meteorological front system arrived (HungaroMet, 2023a) and by March 8, the high atmospheric dynamics made the inversion buildup impossible, and the regular daily temperature fluctuation also nearly ceased (*Fig. 4*). The period of March 1–8 (*Fig. 4*) spectacularly illustrates the difference caused by the effect of the microclimate system of the MS between a period characterized by optimal nocturnal radiation and low atmospheric dynamics (March 1–5), and a non-optimal period characterised by strong atmospheric dynamics (March 5–8) (*Fig. 4*). From March 1 to 5 there are 5 cases

of inversion buildups, representing different types. From March 5 to 8 there is a period characterized by a high level of atmospheric dynamics, without inversion build up in the investigated sinkhole.

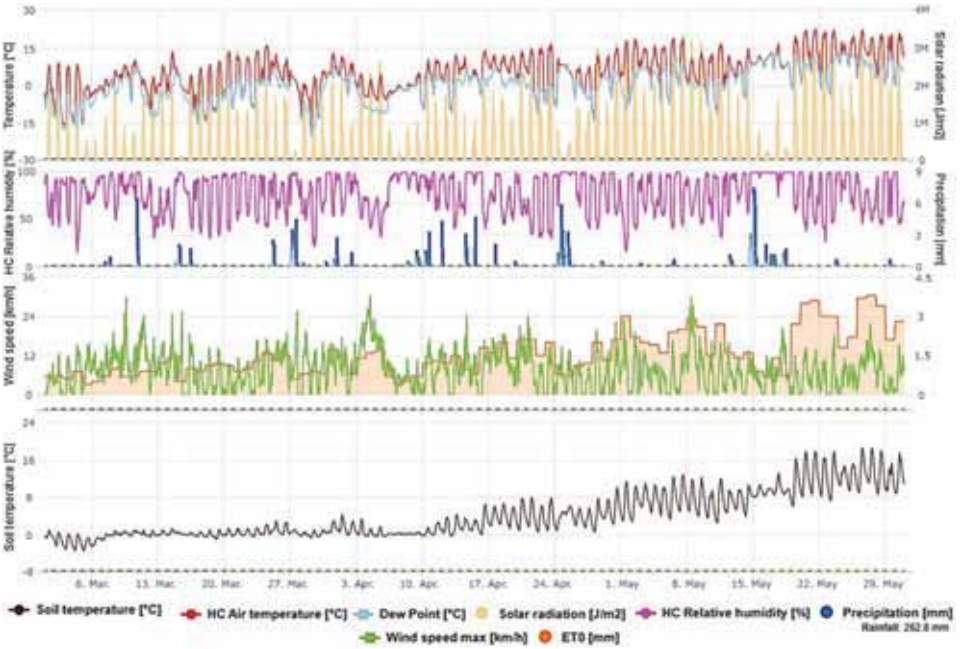

*Fig. 3.*Meteorological parameters measured in 10-minute resolution at the MS station, 2 m above the surface, in the period of marcj 1 – May 31,2023: air temperature (°C), dew point (°C), solar radiation (J/m²), relative humidity (%), precipitation (mm) wind gust (km/h), daily ETO (mm/day), and soil temperature (°C).

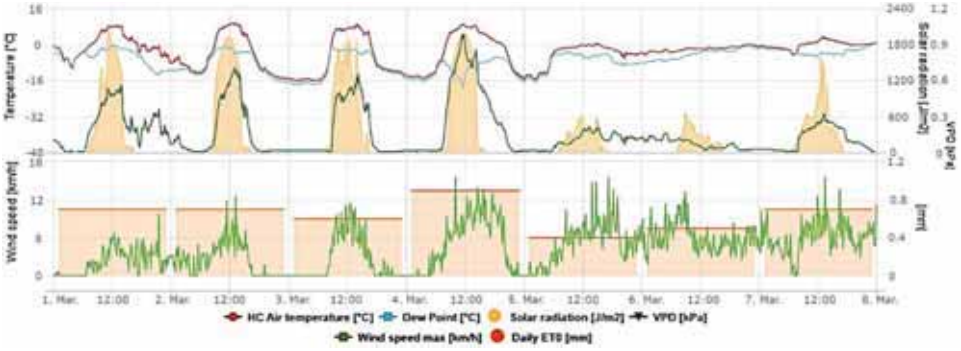

Fig. 4. Meteorological parameters measured in the bottom of the MS, 2 m above the surface, in the period of March 1–8, 2023: air temperature (°C), dew point (°C), solar radiation (J/m²), VPD (kPa), wind gust (km/h), and daily ETO (mm) in hourly resolution.

The period of March 16–24 brought a strong positive temperature anomaly. A negative temperature anomaly was typical for two days, then a strong positive temperature anomaly was observed starting on March 18. However, the temperature inversion was able to develop in the examined area, which meant locally low minimum temperature values, in some cases with values below -10 °C. The period ended on March 24 due to a cold front branch of an incoming weather front system. Following the front, a colder arctic air mass flooded the Carpathian Basin and remained until the March 31 (HungaroMet, 2023a). Minimum values below -10 °C returned to MS. On March 29, the absolute minimum temperature value (-19 °C) of the spring of 2023 was recorded (*Fig. 3*).

To summarize, the most favourable periods for the microclimate to prevail in the MS, which, in local conditions, bring low minimum values and significant daily temperature fluctuations, were March 1–5, March 15t–24, March 27–30, April 9–14, April 20–29, May 1–15, May 19t–23, and May28–31. The value of the relative humidity was determined by the physical characteristics of regional air masses in more dynamic periods from an atmospheric point of view, while in the case of the sinkhole microclimate, it was affected by daily local parameters. In the spring of 2023, 262.4 mm precipitation fell in the MS, distributed evenly. The amount of daily evapotranspiration varied based on the combined effects of the solar radiation, relative humidity, and wind. The lowest values were present at the beginning of the period, in calm weather, with lower solar radiation values. The highest values were measured at the end of the period, with higher solar radiation values and wind. The temperature of the upper layer (-5 cm) of the soil in the bottom of the sinkhole was adapted to the air temperature, including irradiation (shortwave) and radiation (longwave) conditions. At the beginning of the period, with lower solar radiation values, the temperature fluctuation of the typically frozen near-surface soil layer was significantly lower than at the end of the period, despite the similar daily air temperature fluctuations. The reason of this is the increase in the amount and length of daily solar radiation, the own shadow of the sinkhole, and the fact that the heat gain of the thawed soil cover is not hindered by the ice present in the pores of the soil grains. The ground was not covered with snow during the investigated period (*Fig. 3*).

3.6. Typical values of the examined months

The monthly average temperature (*Table 2*) in March 2023, calculated from 10-minute average temperatures, according to the values recorded at 2 m in the MS, was 0.64 °C, while it was 3.5 °C in April, and 9.7 °C in May. The growth of the average temperature was not linear. The highest daily temperature was 16.8 °C in March, 17.8 °C in April, and 23.8 °C in May. The lowest daily temperature was -19.0 °C in March, -13.3 °C in April and -10.7 °C in May. This means that the Tmin value of all three spring months was below -10 °C. The value of the lowest dew point was -21 °C, implying that there was only a 2 °C difference between the

Tmin and the dew point. The relative humidity varied between 99.3% and 11.2%, the average value was 75.4–77.8%; almost the same interval characterized the examined months. The average solar radiation value was 361,720 J/m² in March, 430,911 J/m² in April and 684,024 J/m² in May. The increase in the measured value is not linear, because although the length of the days in the spring period theoretically increases on an equal scale, the absolute incoming solar radiation is greatly modified by the cloud cover and topographical conditions. In the case of the MS, the mountain ridge around has an elevated importance in the reduction of the solar radiation during the winter half year. The highest average daily wind speed was 8.6 km/h, 10.1 km/h, and 10.8 km/h in March, April and May, while the highest absolute wind speed was 29.9 km/h, 30.6 km/h, and 30.2 km/h in March, April, and May. The minimum soil temperature T(s) was -3.6 ℃ in March, -0.4 ℃ in April and 2.2 ℃ in May. The average T(s) in March was exactly 0 ℃; it was 2.5 ℃ in April and 9.8 ℃ in May. The average value of the near-surface T(s) for all three months is within 1 ℃ of the air temperature. This leads to the conclusion that the T(s), although it fluctuates in a smaller value range, follows the daily path of the air temperature and changes with its approximate average (*Table 2*).

Table 2. Summary table of measured parameters in the Mohos sinkhole

Mohos sinkhole (2 m)	Air temperature [°C]			Dew Point [°C]		Solar radiation [J/m²]	Relative humidity [%]			Precipitation [mm]	Wind speed max. [km/h]	Soil temperature [°C]		
Date	avg	max	min	avg	min	avg	avg	max	min	sum	max	avg	max	min
March 2023	0.6	16.8	-19.0	-3.9	-21.0	361720	75.4	99.2	11.8	76.6	29.9	0.0	3.3	-3.6
April 2023	3.5	18.0	-13.3	-0.5	-14.7	430911	78.3	99.3	27.1	98.2	30.6	2.5	10.7	-0.4
May 2023	9.7	23.8	-10.7	5.0	-14.5	684024	77.1	99.3	11.2	88.0	30.2	9.8	19.1	2.2

3.7. Comparison of the coldest days by each month

Fig. 5 shows the Tmin curves of March, April, and May in 2023, measured at 2 m. The process of the buildup of the temperature inversion can be characterized as late in the case of March and slightly disturbed in April and May. The daily temperature fluctuation on the coldest day of each month was 23.7 °C in March, 23.9 °C in April, and 28.5 °C in May. The cooling phase of the curves, depicted between 18:00 p.m. and 09:00 a.m. (CET) is steepest in the case of March, while on the coldest days of April and May, the temperature cooled from the initial

values of 6.1 °C and 11 °C to -13.3 °C and -10.7 °C. Their curves intersected around 21:00 and peaked at 5:10 and 4:10, with a difference of 2.6 °C. They exit the chart at 09:00, at 6.5 °C and 11.7 °C.

The running dynamics of the curve of the lowest temperature in March differ significantly from the minimum temperature curves of the following months. At 01:20, the temperature, which had been almost stagnant until then, began to drop intensively. Then, in 40 minutes, it cooled down to 5.9 °C. It 'peaked' -19 °C, at 06:20. The March temperature curve left the chart area at -3.1 °C at 09:00. The time of occurrence and the interval of the warming phase of the three curves illustrate the shortening of the nights in the spring period and the duration of the potential longwave radiation periods. The monthly Tmin shifted by roughly 1 hour during the examined period.

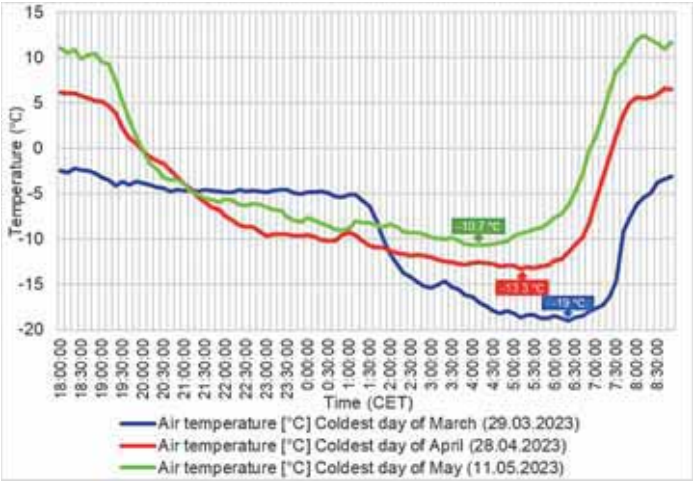

Fig. 5. Tmin curves of the coldest days of each month, recorded in the bottom of the MS, 2 m above the surface in the same time scale from 18:00 p.m. to 8:30 a.m. (CET).

Table 3 contains the daily data for the coldest days of each month in the spring period of 2023. Out of the three examined days, only in the case of March did the daily average temperature fall below 0 °C, and in all other cases, the daily Tmax value stayed above freezing. In no case did the temperature of the air layer located at 2 m reach the dew point. The amount of daily absolute solar radiation tends to increase from 492,750 J/m² to 1,010,200 J/m² as the summer solstice approaches. The minimum value of the daily vapor pressure deficit (VPD) (in kPa) is always 0 kPa during the most significant part of the nocturnal longwave radiation period, and the maximum value varies between 0.2 kPa and 0.5 kPa

towards the end of the period. The daily minimum value of the relative humidity was the most favorable for strong longwave emission in March (18%). This feature is also reflected in the dew point values, as the difference between Tmin and the dew point in March was 2 °C, while other minimum values characterized by a higher relative humidity remained below it. The maximum wind speed of 19.8 km/h recorded on the Tmin day in April was the highest of the three analyzed days. The T(s) only dropped below 0 °C on the Tmin day in March. The station did not register precipitation during neither of these days.

Table 3. Summary table of the coldest days of 2023 of each month by the relevant measured parameters recorded in the bottom of the MS, 2 m above the surface

Mohos sinkhole (2 meters)	Air temperature [°C]			Dew Point [°C]		Solar radiation [J/m²]	VPD [kPa]		Relative humidity [%]			Precipitation [mm]	Wind speed max. [km/h]	Soil temperature [°C]		
Date	avg	max	min	avg	min	avg	avg	min	avg	max	min	sum	max	avg	max	min
March 29, 2023	-6.2	4.7	-19.0	-14.2	-21.0	492750	0.2	0.0	61.4	94.9	18.8	0.0	14.0	0.0	1.1	-0.7
April 28, 2023	1.9	13.2	-13.3	-3.8	-14.7	853825	0.3	0.0	69.9	98.2	37.0	0.0	19.8	3.9	8.1	0.3
May 11, 2023	5.2	17.8	-10.7	-2.2	-11.7	1010200	0.5	0.0	65.5	96.7	28.4	0.0	16.2	7.1	12.4	2.2

3.8. Comparison of the five coldest days

The T-curves show the temperature change of the inversion that can be determined at a height of 2 m above the surface. In the analyzed interval from 16:00 p.m. (through the night) to 8:30 a.m., in all cases, the T-curve of the five coldest days of spring 2023 show the diverse development of the cold-air pool in the MS (*Fig. 6*). Among, the coldest days, three recorded cases fell during the intervals of March 3–5 and the 17 and 29.

The development curve of March 3 (sunrise at 06:14, sunset at 17:25) was undisturbed, apart from one short period disturbed by wind. Good radiation conditions with clear, wind lull weather (*Dorninger et al.,* 2011; *Dobos,* 2023; *Dobos* and *Dobos,* 2023) was prevailed. As a result, the daily Tmin value was -16.2 °C. Within the comparison interval, the starting temperature was 0.6 °C, the

minimum value was -16.2 ℃, and the exit value was -0.5 ℃, so the absolute temperature fluctuation of the parsed interval resulting in undisturbed development was 16.8 ℃.

The curve of March 4 (sunrise at 06:13, sunset at 17:27) shows a slight but constant disturbance; the breakup of the inversion is much earlier than on March 3. Within the comparison interval, the starting temperature was 5.4 ℃, the minimum value was -15.2 ℃, and the exit value was 3.8 ℃, so the absolute temperature fluctuation of the interval resulting in the development of the inversion was 20.6 ℃. This temperature inversion occurred despite the slight disruption of the mixing event affecting its development, it is even higher than the previous interval's fluctuation value.

The curve of March 5 (sunrise at 06:11, sunset at 17:28) indicates the later onset of the inversion buildup within the potential longwave emission period (late buildup) (*Dorninger et al.,* 2011; *Dobos,* 2023; *Dobos* and *Dobos,* 2023). The reason of that is that the level of significant disturbance decreased long after the beginning of the potential longwave radiation period. The breakup of the curve occurred the earliest on the March 5 of the five coldest days examined. Within the comparison interval, the starting temperature was 4.6 ℃, Tmin was -15.5 ℃, and the exit value was -1.4 ℃, so the absolute thermal fluctuation of the interval resulting in the buildup was 20.1 ℃. The T-curve indicates a significant and permanent disturbance that affects the development of the temperature inversion, but does not eliminate its existence, because the resistivity of cold-air pool against the external affect is co-evolved with the level of the development (*Petkovšek,* 1992; *Rakovec et al.,* 2002).

The temperature curve showing the formation of Tmin on March 17 (sunrise at 05:46, sunset at 17:46) is a typical example of mixing events. Mixing events are invoked by external influences (wind, clouds) that have an intense effect on the potential period that enables the formation of the inversion, and when they cease, the cold-air pool stabilizes again (*De Wekker et al.,* 2006; *Dorninger et al.,* 2011; *Dobos,* 2023; *Dobos* and *Dobos,* 2023).

The initial value of the temperature curve at 16:00 was 1.2 ℃; it cooled down to -11 ℃ by 20:30. Then, the temperature increased to -3.5 ℃ by 22:30, and until 1:00, it fluctuated in a narrow range depending on the strength of the wind disturbance. After the abatement and termination of the mixing event, the daily Tmin value stood at -15.5 ℃ at 5:40, after the wind was moderated again. Following that, the temperature started to rise temperately and then steeply, the mixing event intensified again and then, due to the insolation, it left the area of the diagram at 1.9 ℃.

The coldest day of the spring period, in addition to the case of the late buildup of the cold-air pool, occurred on March 29 (sunrise at 06:22, sunset at 19:03), with a daily Tmin of -19 ℃. The complex case study of the coldest day of the measured period is described in the following chapter.

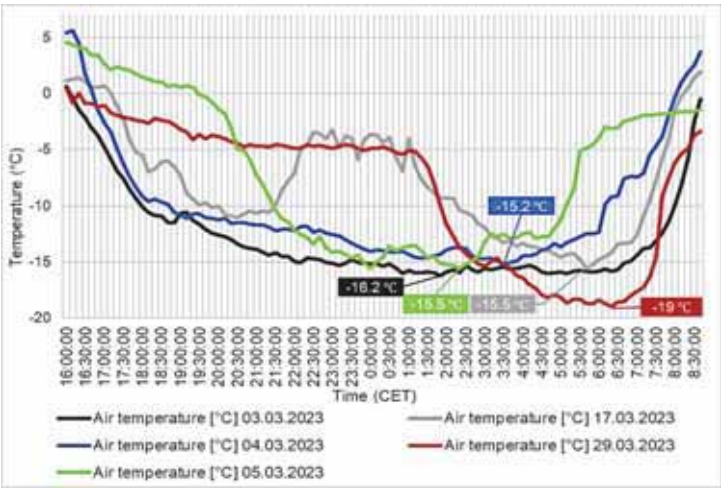

Fig. 6. Air temperature curves of the five coldest days of the period of the spring of 2023, recorded in the bottom of the MS, 2 m above the surface, in a same time scale from 16:00 p.m. to 8:30 a.m. (CET).

4. Case study of the coldest event of the spring of 2023

4.1. Covariance analysis of the measured meteorological parameters in case of late inversion buildup

The recorded data of the absolute Tmin day are listed in *Table 4*. The average temperature on March 29 was -6.2 ℃; the temperature extremes were 4.7 ℃ and -19 ℃. The average temperature, measured at 40 cm above the surface was -8.5 ℃; the temperature extremes were 3.6 ℃ and -20.8 ℃ (at 40 cm only the temperature was recorded).

Table 4. Summary table of the coldest day by all relevant measured parameters

Mohos sinkhole (2 meters)	Air temperature [°C]			Dew Point [°C]		Solar radiation [J/m²]	VPD [kPa]		Relative humidity [%]			Precipitation [mm]	Wind speed max. [km/h]	Soil temperature [°C]		
Date	avg	max	min	avg	min	avg	avg	min	avg	max	min	sum	max	avg	max	min
March 29, 2023	-6.2	4.7	-19.0	-14.2	-21.0	492750	0.2	0.0	61.4	94.9	18.8	0.0	14.0	0.0	1.1	-0.7

Fig. 7 and *Tables 4–6* present the processed database. The examination period presented in the tables covers the period between March 28, 2023 18:00 a.m. and March 29, 2023 09:00 p.m. A variance analysis was performed (*Microsoft Office Professional Plus 2016, Anova: Single Factor* function) to characterize the correlations and statistical covariances of the measured parameters. The results of the ANOVA are summarized in *Table 5*, which quantitatively illustrate the main characteristics of the dataset for the 10-minute averages of the measured values. There were 90 measurements observed for the period. The values of the variation analysis between groups according to the factors are the following: sum of squares (SS) = 478,427.54, degrees of freedom (df) = 5, mean squares = 95,685.51 and F statistic = 2361.1. The P-value is 0 and the F criterion is 2.23. The values within the groups, according to the factors, are SS = 21,640.77, df = 534 and MS = 40.52. Overall, SS = 539 and df = 539. The source of variation shows a significant variance (ANOVA) based on the factor F and P-value where P (0) < 0.05 and F (2361.101) > F crit (2.230896).

Table 5. Table of ANOVA analysis of the database described in Section 4, based on the investigated microclimate event (late buildup of cold-air pool) in the day of the coldest Tmin.

ANOVA Summary

Groups	*Count*	*Sum*	*Average*	*Variance*
Air temperature (°C)	90	-829.16	-9.21289	36.92435
Dew point (°C)	90	-1183.2	-13.1467	19.8996
VPD (kPa)	90	8.45	0.093889	0.005772
Relative humidity (%)	90	6716.72	74.63022	170.2659
Wind speed max. (km/h)	90	389.4	4.326667	15.99951
Soil temperature (°C)	90	-25.4	-0.28222	0.05968

ANOVA

Source of Variation	*SS*	*df*	*MS*	*F*	*P-value*	*F crit*
Between groups	478427.54	5	95685.51	2361.101	0	2.230896
Within groups	21640.777	534	40.5258			
Total	500068.31	539				

4.2. Correlation analysis of the measured variables in case of late inversion buildup

The correlation analysis of the variables of the investigated microclimate event (*Table 6*, *Fig. 7*) concerns an example of the late buildup (*Dorninger et a*l., 2011) of temperature inversion. The mutual altering of individual variables is more significant within a more dynamic, multifactorial event. Thus, the processing of the microclimate case resulting in the coldest temperature of the spring of 2023 within the selected time scale (the same as the previous) is suitable for the correlation analysis. The solar radiation value is not present in *Table 6*, because of the insolation's non-representative proportion in the examined period, especially in case of late buildup of the cold-air-pool. In the case of correlation analysis, the analysis of an entire period of solar radiation (shortwave) and emission (longwave radiation) would be ideal to use. However, it illustrates the late buildup type of the analyzed temperature inversion case, by presenting the difference between the end of the insolation and the start of the inversion build up (dropping of the T-curves).

Table 6. Correlation analysis of measured variables used in the case described in Section 4.2, based on the investigated microclimate event (late buildup of cold-air pool) in the day of the coldest Tmin.

Correlation	Air Temperature (°C)	Dew point (°C)	VPD (kPa)	Relative humidity (%)	Wind speed max (km/h)	Soil temperature (°C)
Air Temperature (°C)	1					
Dew point (°C)	0.92330214	1				
VPD (kPa)	0.852487159	0.589986648	1			
Relative humidity (%)	-0.796427533	-0.50718294	-0.9898845	1		
Wind speed max (km/h)	0.829947887	0.741720119	0.76561716	-0.717710297	1	
Soil temperature (°C)	0.952531281	0.840751343	0.86311717	-0.813203582	0.776117482	1

According to *Table 6*, the variable that correlates the most with air temperature is the soil temperature ($r = 0.95$), followed by the dew point ($r = 0.92$), VPD ($r = 0.85$), wind speed ($r = 0.82$), and the relative humidity ($r = -7.2$. The correlation with the air temperature is strong for all variables ($r \geq 0.7$). The dew point correlates strongest with the air temperature ($r = 0.92$). It is followed by the soil temperature ($r = 0.84$) and wind speed ($r = 0.74$), which still has a strong correlation. The correlation of the VPD ($r = 0.58$) and relative humidity ($r = -0.51$) with the dew point are moderate. The correlation of the VPD with relative humidity is the strongest ($r = 0.99$), followed by the soil temperature ($r = 0.86$), air temperature ($r = 0.85$), and wind speed ($r = 0.76$). The VPD's covariation with the dew point is medium ($r = 0.59$). Excluding the dew point ($r = -0.51$), the degree of covariation of the relative humidity is strong for all variables, and its range is negative. The correlation of the relative humidity with the VPD is the strongest ($r = 0.99$), since the relative humidity and the momentary difference in the amount of moisture needed to saturate the given air mass have an effect on each other. The VPD is followed by the soil ($r = -0.81$) and air ($r = 0.8$) temperatures and wind speed ($r = 0.72$), which have a strong correlation. The degree of mutual alternation is the smallest among the variables that are strongly correlated with the relative humidity. The correlation of the wind speed with all examined variables is strong without exception. However, a correlation value above 0.8 is only obtained for the air temperature. The covariance values of the other variables are concentrated within a narrow range from $r = 0.71$ to 0.77. The correlation of soil temperature with air temperature is the strongest ($r = 0.95$), however, it should be mentioned that the degree of covariation would be low in the case of snow cover. The degree of covariation of the soil temperature with additional variables is also high in all cases. Overall, it can be said that the studied variables correlate the best with the air temperature (without snow covering, but in case of 2–4 cm snow, $r = 0.57$ and in case of 35 cm snow $r = 0.29$ in -5 cm (*Dobos*, 2024)), but the covariation among almost all variables is strong. The exceptions are the correlations of the dew point with the VPD ($r = 0.58$) and with the relative humidity ($r = 0.51$), which only resulted medium range values. In the period examined in this subsection, there are no weak relationships between the variables. The late buildup type of cold-air pool (temperature inversion) is characterized by the fact that the disturbing events (wind, clouds) that prevent the development disappear late in the potential nocturnal emission period. Thus, causing a delay but creating the conditions for the development of the cold-air pool, which are a clear night sky and calm winds. On the night from 28th to 29th of March, 2023, a typical case of late buildup took place in the Mohos sinkhole (*Fig. 7*).

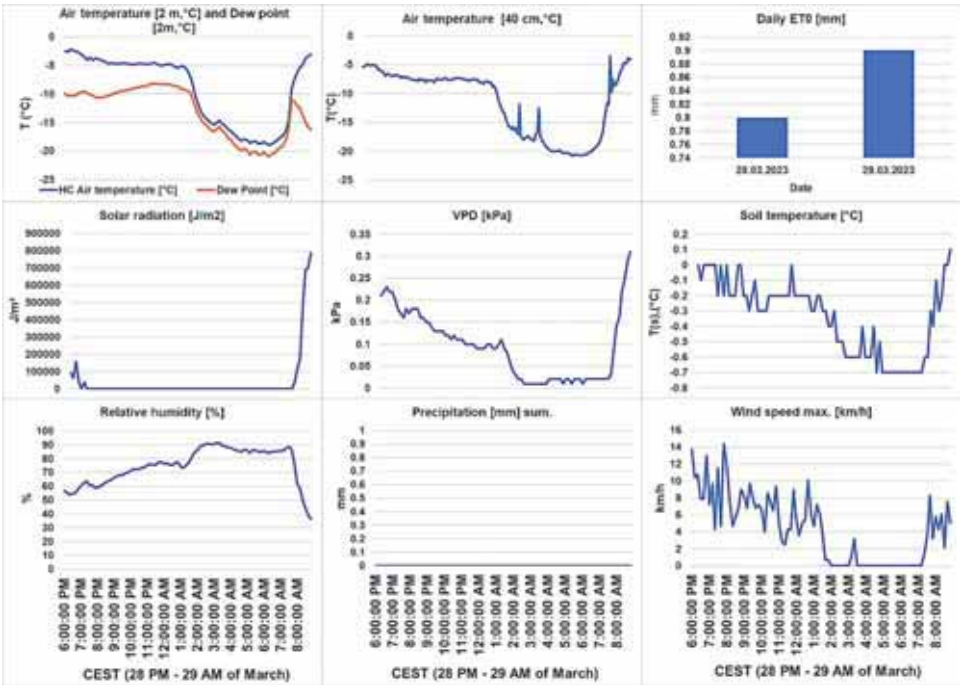

Fig. 7. Typical case of the late buildup of the temperature inversion in the night of March 28–29, 2023 (CEST), in 10 minutes resolution (except the daily evapotranspiration). The presented parameters are the next: air temperatures at 200 cm and 40 cm in °C; dew point at 200 cm in °C; daily evapotranspiration (ETO) at 200 cm, in mm/day (sum.); solar radiation at 200 cm in J/m², vapor pressure deficit (VPD) at 200 cm in kPa; soil temperature at -5 cm under the surface, in °C; relative humidity at 200 cm in %; precipitation at 200 cm in mm (sum) and wind speed at 200 cm in km/h.

The first step of the graphical analysis is the comparison of the air temperature data measured at 200 cm and 40 cm above the surface (from the sinkhole's bottom) in the examined period. The rakes of the T-curves were similar; however, the air layer near the surface were much more unstable and sensitive to external effects than the air layer at 200 cm. The entry value of the temperature curve measured at 40 cm at 18:00 was -5.4 °C, while the one measured at 200 cm was -2.5 °C. The measured difference was almost 3 °C, which remained until the rapid temperature drop starting at 1:00; when the air temperature was -8 °C at 40 cm and -5 °C at 200 cm. At this point, the wind speed began to moderate rapidly, and the dew point and VPD also began to fall as the temperature decreased under conditions that became favorable for the buildup of the cold-air pool. The relative humidity of the rapidly cooling air moved towards saturation and peaked at 91.62% at 3:10. Following that, the air temperature began

to slowly decrease. Between 03:10 and 03:30, a 20-minute windy period broke the dynamics of the undisturbed microclimate system of the sinkhole, causing a slight warming, with a peak value of -14.4 ℃ at 200 cm at 03:20. The behavior of the air currents detected at 2 m explains the dynamics of the temperature curve at 200 cm, but there was no significant change in the dynamics of the air layer detected near the surface at the same time. In the near-surface temperature (40 cm), between 02:40 and 03:00, a strong warming can be observed from -17.1 ℃ to -11.8 ℃, followed by a cooling up to -17.4 ℃. After that, between 03:35 and 04:00, there was also a significant warming and then a cooling from -18.2 ℃ to -12.5 ℃ and back to -18.1 ℃. The third obvious affect happened near the surface, during the warming period at 07:40, when a maximum wind gust was recorded at 200 cm in the morning and disturbed the near surface air layers. None of the variables measured at 200 cm showed a clear covariation with the change in the air temperature at 40 cm above the surface. From this, it can be concluded that in the late build-up phase, there was a case of lower disturbance in the MS, which stopped the temperature inversion near the surface for short periods (*Dorninger et al.,* 2011; *Dobos,* 2023; *Dobos* and *Dobos,* 2023). The inverse air layering, according to the air density, was immediately restored with the reduction of the stratification of the near-surface air currents, after the cold-air masses close to the surface from the direction of the sinkhole's slopes returned to the bottom of the sinkhole. Following the Tmin occurred at -20.8 ℃ at 06:20 at 40 cm, the near-surface temperature curve leaves the diagram area at -4 ℃. The data of the variables recorded at 200 cm confirm the values indicated by the correlation matrix, implying that the instantaneous covariation of the parameters measured in the given air layer are strong, they respond without exception to external atmospheric effects. It should be emphasized that the fluctuation of the T(s) follows the fluctuation of the near-surface T-curve with a slight delay, especially in the case of outlier disturbances. After the impact of insolation at 7:40, the T and T(s), the dew point and the VPD rise rapidly, the relative humidity starts to decrease accordingly, the microclimate system of the sinkhole is less effective inside the sinkhole, and the turbulent air currents caused by convection are partially eliminated; the temperature inversion forms in the sinkhole, and the temperature inversion disappears or moves to the shaded side of the sinkhole. The temperature inversion persists until the end of the examined period (09:00). The presence of various turbulent airflows is a significant factor in the erosion of the cold-air pool. The eventual outcome of this is proportional to the stability of the cold-air pool and the buoyant force of the turbulent airflow and vertical wind shear (*Petkovšek,* 1992; *Rakovec et al.,* 2002). The threshold for overturning the equilibrium effect is the Richardson's critical value ($R^2 = 0.25$), which can erode the temperature inversion (*Kunze et al.,* 1990; *Glickman,* 2000; *Dorninger et al.,* 2011).

5. Statistical summary of the data measured in the Mohos sinkhole in the spring of 2023

The air temperature-based daily (*Table 7*) and monthly (*Table 8*) summary tables of the spring measurement period of the Mohos sinkhole in 2023 present the quantitative and statistical characteristics of the investigated period in meteorologically relevant categories. The average temperature, calculated on the basis of 10-minute averages for the analyzed period, is 4.6 ℃. There is a 16-fold difference between the average temperatures of the coldest and warmest months. The monthly Tmin was always below -10 ℃, the absolute minimum value of the measured period was -19 ℃ at 2 m (-20.8 ℃ at 40 cm) and Tmax was 23.8 ℃. The average of the daily Tmin values in all three months is in the negative range, and for the entire examined period it is -4.4 ℃. There is a 11-fold difference between the average daily Tmin values of the coldest (March) and warmest (May) months. The monthly average of Tmax values, which are less affected by the microclimate system as spring progresses, does not show such a large difference. The reason of this is that the main affected parameters of the sinkhole microclimate system are the extremely low daily Tmin values compared to their environment. The monthly temperature fluctuation in all cases exceeds 30 ℃; in the case of March, it is 35 ℃. The coldest daily average is -6.3 ℃. The average temperature of every day in the month of May is positive (*Table 7*).

Table 7. The statistical summary of the measured air temperature values in monthly distribution, recorded in the bottom zone of the MS, 2 m above the surface in ℃ scale

Mohos sinkhole (2 m) Investigated period	March 2023	April 2023	May 2023	Sum. (all 92 days)
10-minute average ℃	0.6	3.6	9.7	4.6
Tmin ℃	-19.0	-13.3	-10.7	-19.0
Tmax ℃	16.8	18.0	23.8	23.8
Tmin avg. ℃	-7.9	-4.7	-0.7	-4.4
Tmax avg. ℃	8.8	10.6	18.3	12.6
Monthly absolute temperature fluctuation ℃	35.8	31.3	34.5	42.8
Coldest daily average temperature ℃	-6.3	-3.6	3.46	-6.3

During the examined 92-day period (*Table 8*), there were 74 frozen days (Tmin ≤ 0 ℃) in the MS, which means that 80.4% of the days were below freezing within the period. Only two days in March did not have below-freezing temperatures. The average daily temperature was equal or less than 0 ℃ 19 times

(20.7% of all days). From the summary, two days (2.2%) remained below the daily Tmax value of 0 °C (Tmax ≤ 0 °C). The station registered 40 daily minimum values below -5 °C (Tmin ≤ -5 °C) in March; this happened 14 times in April and 7 times in May (43.5% of the all 92 days). The station also measured 13 daily minimum values below -10 °C (Tmin ≤ -10 °C) in March; 3 times in April and 1 time in May (18.5% of the all 92 days). The temperature dropped below -15 °C (Tmin ≤ -15 °C) only in March, but this did occur on six days in March (6.5% of the all 92 days). The station did not measure a value of -20 °C or below that at 2 m, it was only registered once, close to the surface (40 cm) (*Table 8*).

Table 8. The statistical summary of the measured air temperature values, in daily resolution, recorded in the bottom zone of the MS, 2 m above the surface in °C scale

Mohos sinkhole (2 m) Investigated period	March 2023	April 2023	May 2023	Sum. (all 92 days)	%
Average daily temperature ≤ 0 °C	14	5	0	19	20.7
Tmax ≤ 0 °C	1	1	0	2	2.2
Tmin ≤ 0 °C	29	27	18	74	80.4
Tmin ≤ -5 °C	19	14	7	40	43.5
Tmin ≤ -10 °C	13	3	1	17	18.5
Tmin ≤ -15 °C	6	0	0	6	6.5
Tmin ≤ -20 °C	0	0	0	0	0.0

6. Conclusions

The data show that in the first third of the measurement period, the expected minimum daily temperature value was close to -10 °C; reaching or exceeding this value was not considered as outlier in the MS (Fig. 3). Daily Tmins below -15 °C were experienced only in March. The mentioned values occurred serially at the very beginning of the period and then in a spot-like manner (*Fig. 4*). There are significant increases in the daily average of the minimum temperature for the examined months; however, in all cases and overall, the average of the daily T-min values remained in the negative temperature range. The temperature fluctuation of the entire examined period was 42.8 °C. The absolute Tmax was 23.8 °C, and Tmin was -19 °C; the T-values were extreme in the negative direction compared to the national averages. The processed case examples are in agreement with the literature; they confirm the results and test methodology of previous studies (*Whiteman et al.,* 2004*; Steinacker et al.,* 2007; *Dorninger et al.,* 2011). The examined temperature inversion presented a build-up, stood, and broke drown manner according to the characteristic features of the identifiable

development type in each case. In some cases, the partial persistence of the temperature inversion during the day was also recorded (*Keveiné,* 2011).

The air temperature correlates strongly with almost all measured parameters, showing the complex nature of cold-air pool development. The highest correlation rate was observed with the soil temperature having an $r = 0.95$. Although the T(s) fluctuates in a smaller value range, it follows the daily path of the air temperature and changes with its approximate average. The correlation with the dew point is $r = 0.92$, the VPD has $r = 0.85$, the wind speed has $r = 0.83$ and the relative humidity has $r = -0.8$. There was no precipitation in the timescale of the case processing, thus the relationship with the other parameters, based on this period are unexaminable. It can be established, that in case of significant microclimatical events, the air temperature has the highest, while dew point and the relative humidity have the lowest correlation with each of the other measured parameters. This result, in agreement with the literature, assumes a low interaction between the inversion build-up and the momentary level of the relative humidity, as long as the air saturation does not exceed the condensation threshold. The reason of that is the fog formation which reduces the value of the longwave surface radiation (*Whiteman et al.,* 2007; *Dorninger et al.,* 2011).

It is important to note, that the degree of covariation of the T(s) with the other measured parameters in the case study was analyzed in conditions without snow covering. The qualitative presence of the snow covering basically affects the degree of correlation of the T(s) with the air temperature (*Goodrich,* 1982; *Thorn et al.,* 1999; *Beltrami,* 2001; *Sokratov* and *Barry,* 2001; *Decker et al.,* 2003).

By the temporary control measurements, the average anomaly levels (between MS and K2, and MS and K1) of the research area are in alignment of the results of what the *Cold Air Flow* model suggested (*Table 1, Fig. 1*). Moreover, based on the measurements, in case of stable inversion build-up, the temperature difference of the daily Tmin values between the bottom of the sinkhole and the K1 and K2 control points do not depend on snow coverage.

Although the near-surface layers of the temperature inversion are exposed to the effect of cold air masses flowing near the surface from the sides of the sinkhole, which often cause momentary disturbances, the regeneration occurs almost immediately after the lower disturbance event. The near-surface air layers are more protected against the external meteorological effects from outside of the sinkhole (*Dorninger et al.,* 2011). By all means the behavior of the near-surface air layers are the most independent regarding the microclimate system of the closed depressions. Further measurements are needed to have a better understanding on them.

Out of the seven selected days with extremely low Tmin values, four (March 17 and 19, April 28, and May 11) dates were below the long-term average temperature, two had average (March 4 and 5), and one had higher than the long-term average temperature in the Hungary (March 3). The days of the official national minimum temperatures recorded by the Hungarian Meteorological

Service never matched with the ones when the Mohos sinkhole minimum records were measured. None of the sinkhole minimums were measured in the nationally recorded colder weather situations. It was concluded, that in case of the sinkhole microclimate, the regional weather anomalies have less impact on the build-up of cold-air pools than the local atmospheric dynamics and their characteristics and expressions. The presence of a topographic microclimate system in the Bükk Plateau's Mohos sinkhole was generally present based on the measured data from the spring of 2023. The data contained the lowest measured temperature value that was detected in the country during the examined period (including the non-official data) (HungaroMet, 2023a).

Acknowledgment: We would like to acknowledge the contribution of the University of Miskolc, Institute of Geography and Geoinformatics for allowing me to use the meteorological station. I also want to thank Róbert Kerékgyártó for sharing with me the data of K1 control point and for the sources of history of science. I also wish to thank the Bükk National Park (BNPI) for kindly granting permission to carry out measurements in the strictly protected area.

References

Aigner, S., 1952: Die Temperaturminima im Gstettnerboden bei Lunz am See, Niederösterreich (The minimum temperatures in the Gstettner basin near Lunz, Lower Austria). *Wetter Leben*, Special Issue *1*, 34–37.

Bacsó, N. and *Zólyomi B.*, 1934: Mikroklíma és növényzet a Bükk-fennsíkon. *Időjárás 38*, 177–196. (In Hungarian)

Bátori, Z., Csiky, J., Farkas, T., Vojtkó, E.A., Erdős, L., Kovács, D., Wright, T., Körmöczi, L., and *Vojtkó, A.*, 2014a: The conservation value of karst dolines for vascular plants in woodland habitats of Hungary: refugia and climate change. *Int. J. Speleology 43*(1), 15–26. http://dx.doi.org/10.5038/1827-806X.43.1.2

Bátori, Z., Farkas, T., E Vojtkó, A., Maák, I. E., and *Vojtkó, A.* 2014b: Veszélyeztetett növényfajok Magyarország erdős és gyepes többreinek lejtői mentén. *Kanitizia 21*(3–4), 53–62. (In Hungarian)

Beltrami, H., 2001: On the relationship between ground temperature histories and meteorological records: a report on the Pomquet station. *Glob. Planet. Change 29*(3–4), 327–348. http://dx.doi.org/10.1016/S0921-8181(01)00098-4

Clements, C. B., Whiteman, C. D. and *Horel, J.D.*, 2003: Cold air pool structure and evolution in a mountain basin: Peter Sinks, Utah. *Appl. Meteor. 42*, 752–768. http://dx.doi.org/10.1175/1520-0450(2003)042%3C0752:CSAEIA%3E2.0.CO;2

De Wekker, S. F. J., and *Whiteman, C. D.*, 2006: On the time scale of nocturnal boundary layer cooling in valleys and basins and over plains. *J. Appl. Meteorol. 45*, 813–820. http://dx.doi.org/10.1175/JAM2378.1

Decker, K. L. M., Wang, D., Waite, C., and *Scherbatskoy, T.*, 2003: Snow removal and ambient air temperature effects on forest soil temperatures in northern Vermont. *Soil Sci. Soc. Amer. J. 67*(4), 1234–1242, https://doi.org/10.2136/sssaj2003.1629

Dobos, A., 2023: A légköri események és a domborzati viszonyok hatása az inverziós légrétegződés kialakulására a Bükk-fennsíki Mohos-töbörben, M.S. thesis, Dept. of Geography and Geoinformatics, University of Miskolc. (In Hungarian) http://midra.uni-miskolc.hu:80/?docId=43397

Dobos, A. and *Dobos, E.*, 2023: Légköri események hatása az inverziós légrétegződésre a Bükk-fennsíki Mohos-töbör eseti példáin keresztül. Bányászati, Kohászati és Földtani Konferencia, 70–75., ISSN 2784-093X. (In Hungarian)

Dobos, A., 2024: A lég- és talajhőmérsékleti viszonyok együttváltozásának vizsgálata a hóborítottság és talajfagy mértékének alapján a Bükk-fennsíki Mohos-töbörben. Bányászati, Kohászati és Földtani Konferencia, 57–63., ISSN 2784-093X.(In Hungarian)

Dobos, A., Kerékgyártó, R., and Dobos, E. (2024). A 2022-2023-as téli szezon összefoglaló elemzése a Bükk-fennsíki Mohos-töbör és Vörösmeteor-töbör mérései alapján. *Légkör 69*, 33–40. (In Hungarian) http://doi.org/10.56474/legkor.2024.1.5

Dorninger, M., Whiteman, C.D., Bica, B., Eisenbach, S., Pospichal, B., and *Steinacker, R.*, 2011: Meteorological events affecting cold-air pools in a small basin. *J. Appl. Meteorol. Climatol 50*, 2223–2234, http://dx.doi.org/10.1175/2011JAMC2681.1

Egli, B.R., 1991: The special flora, ecological and edaphic conditions of dolines in the mountains of Crete. *Botanika Chronika 10*, 325–335.

Eisenbach, S., Pospichal, B., Whiteman, C. D., Steinacker, R., and *Dorninger, M.*, 2003: Classification of cold air pool events in the Gstettneralm, a sinkhole in the Eastern Alps. In Extended Abstracts, Int. Conf. on Alpine Meteorology and MAP-Meeting, Brig, Switzerland. *MeteoSwiss Publ. 66*, 157–160.

FieldClimate.com: https://www.fieldclimate.com/ (03.06.2024)

Geiger, R., 1965: The climate near the ground. Harvard University Press. Massachusetts, Cambridge.

Glickman, T.S. (Ed.)., 2000: Glossary of meteorology. American Meteorological Society.

Goodrich, L.E., 1982: The influence of snow cover on the ground thermal regime. *Canadian Geotech. J. 19*, 421–432. http://dx.doi.org/10.1139/t82-047

Hevesi, A., 2002: Természetföldrajzi Kislexikon. Műszaki Könyvkiadó, Budapest. (In Hungarian)

Horvat, I., 1952: Die Vegetation der Karstdolinen. *Hrvatski geografski glasnik 14*(1), 1–22. (In German)

HungaroMet, 2023a: Napijelentés kiadvány: (03.06.2024.) (In Hungarian) https://www.met.hu/idojaras/aktualis_idojaras/napijelentes/

HungaroMet, 2023b: Elmúlt hónapok időjárása: (03.06.2024.) (In Hungarian) https://www.met.hu/eghajlat/magyarorszag_eghajlata/eghajlati_visszatekinto/elmult_honapok_idojarasa/

Keveiné Bárány, I., 2011: Néhány adat a bükki töbrök mikroklímájához. A Miskolci Egyetem Közleményei, A sorozat, Bányászat, 82. (In Hungarian)

Kocsis K. (főszerk.) 2018. Magyarország Nemzeti Atlasza – Természeti környezet. Budapest, MTA CSFK Földrajztudományi Intézet. (In Hungarian)

Kunze, E., Williams, A. J., and *Briscoe, M. G.*, 1990: Observations of shear and vertical stability from a neutrally buoyant float. *J. Geophys. Res.: Oceans, 95*(C10), 18127–18142. http://dx.doi.org/10.1029/JC095iC10p18127

Lehmann A., 1970: Tarvágás által okozott ökológiai változások az abaligeti karszton. *Pécsi Műszaki Szemle 25*, 15–21. (In Hungarian)

MeteoPont.hu: http://bukk.meteopont.hu/ (03.06.2024.)

Operating Instructions of DL-240k temperature data logger. (03.06.2024.) https://asset.conrad.com/media10/add/160267/c1/-/gl/001931526ML01/hasznalati-utmutato-1931526-homerseklet-adatgyujto-2001372-c-pdf-funkcio-voltcraft-dl-240k.pdf ,

Ozkan, K., Gulsoy, S., Mert, A., Ozturk, M., and *Muys, B.*, 2010: Plant distribution-altitude and landform relationships in karstic sinkholes of Mediterranean region of Turkey. *J. Environ. Biol. 31*(1), 51.

Petkovšek, Z., 1992: Turbulent dissipation of cold air lake in a basin. *Meteorol. Atmosph Phys. 47*(2–4), 237–245, http://dx.doi.org/10.1007/BF01025620

PIX4Dcloud: (03.06.2024.) https://cloud.pix4d.com/drive

Pospichal, B., Eisenbach, S., Whiteman, C. D., Steinacker, R., and *Dorninger, M.*, 2003: Observations of the cold air outflow from a basin cold pool through a low pass. International Conference on Alpine Meteorology, Brig, Switzerland.

Product Portfolio of iMETOS 3.3: (2023.05.20) https://efesaro.com/catalogos/Catalogo_Pessl.pdf

Rakovec, J., Merše, J., Jernej, S., and *Paradiž, B.*, 2002: Turbulent dissipation of the cold-air pool in a basin: Comparison of observed and simulated development. *Meteorol. Atmosph Phys 79*(3), 195–213.

SAGA-GIS Tool Library Documentation (v7.8.0), Tool Cold Air Flow: (03.06.2024.) https://saga-gis.sourceforge.io/saga_tool_doc/7.8.0/sim_air_flow_0.html ,

Salavec, P., 2012: Inverzió és légszennyezés, valamint az égetés hatása a levegő minőségére falusi környezetben. *Tolmácsi Kisbíró 11*, 2–3. (In Hungarian)

Sauberer, F. and *Dirmhirn, I.*, 1954: Über die Entstehung der extremen Temperaturminima in der Doline Gstettner-Alm. *Archiv für Meteorologie, Geophysik und Bioklimatologie, Serie B, 5*, 307–326. http://dx.doi.org/10.1007/BF02242757

Schwab, A., 2000: Reliefanalytische Verfahren zur Abschaetzung naechtlicher Kaltluftbewegungen. Freiburger Geographische Hefte, 61.

Sokratov, S.A., and. *Barry, R.G*., 2002: Intraseasonal variation in the thermoinsulation effect of snow cover on soil temperatures and energy balance. *J. Geophys. Res.: Atmosph. 107*.D10: ACL-13, http://dx.doi.org/10.1029/2001JD000489

Steinacker, R., Whiteman, C.D., Dorninger, M. B., Pospichal, S., Eisenbach, A.M., Holzer, P., Weihs, E., Mursch-Radlgruber, A., and Baumann, K., 2007: A sinkhole field experiment in the Eastern Alps. Bull. Amer. Meteorol. Soc. 88, 701–716, http://dx.doi.org/10.1175/BAMS-88-5-701

Thorn, C.E., Schlyter, J.P.L., Darmody, R.G., and *Dixon, J.C.*, 1999: Statistical relationships between daily and monthly air and shallow-ground temperatures in Kärkevagge, Swedish Lapland. *Permafrost and Periglacial Processes, 10*(4), 317–330. http://dx.doi.org/10.1002/(SICI)1099-1530(199910/12)10:4%3C317::AID-PPP329%3E3.0.CO;2-S

Utah Climate Center, https://climate.usu.edu/PeterSinks, 03.06.2024.

Wagner, R., 1964: Lufttemperaturmessungen in einer Doline des Bükk-Gebirges. *Zeitschr. für Angewandte Meteorologie 5*(3–4), 192–199.

Whiteman, C.D. and *McKee, T.B.*, 1982: Breakup of temperature inversions in deep mountain valleys: Part II. Thermodynamic model. *J. Appl. Meteor. 21*, 290–302. http://dx.doi.org/10.1175/1520-0450(1982)021%3C0290:BOTIID%3E2.0.CO;2

Whiteman, C.D., De Wekker, S. F. J., and *Haiden, T.*, 2007: Effect of Dewfall and Frostfall on Nighttime Cooling in a Small, Closed Basin. *J.Appl. Meteorol. Climatol. 46*(1), 3–13 http://dx.doi.org/10.1175/JAM2453.1

Whiteman, C.D., Haiden, T., Pospichal, B., Eisenbach, S., and *Steinacker, R.*, 2004: Minimum temperatures, diurnal temperature ranges, and temperature inversions in limestone sinkholes of different sizes and shapes. *J.Appl. Meteorol. Climatol. 43*(8), 1224–1236, http://dx.doi.org/10.1175/1520-0450(2004)043%3C1224:MTDTRA%3E2.0.CO;2

Whiteman, C.D., 1990: Observations of thermally developed wind systems in mountainous terrain. In: (Ed. *Blumen, W.*) Atmospheric Processes over Complex Terrain, Meteorological Monographs 23 No. 45, American Meteorological Society, Boston, Massachusets, 5–42, http://dx.doi.org/10.1007/978-1-935704-25-6_2

Zhang, T., 2005: Influence of the seasonal snow cover on the ground thermal regime: An overview. *Rev. Geophys. 43*(4), http://dx.doi.org/10.1029/2004RG000157

DOI:10.28974/idojaras.2025.3.4

IDŐJÁRÁS

Quarterly Journal of the HungaroMet Hungarian Meteorological Service
Vol. 129, No. 3, July – September, 2025, pp. 307–337

Bioclimate conditions in the Mura-Drava-Danube Transboundary Biosphere Reserve – case study from Serbia

Jelena Dunjić [1], **Vladimir Stojanović** [1], **Dragan Milošević** [2], **Milana Pantelić** [1,*], **Sanja Obradović** [3], and **Milica Vasić** [3]

[1] *University of Novi Sad, Faculty of Sciences, Chair of Geoecology*
Trg Dositeja Obradovića 3, Novi Sad, Serbia

[2] *Wageningen University and Research, Meteorology and Air Quality Group*
6705 Wageningen, Netherlands

[3] *University of Novi Sad, Faculty of Sciences, Department of Geography, Tourism and Hotel Management;*
Trg Dositeja Obradovića 3, Novi Sad, Serbia

**Corresponding Author e-mail: milanap@dgt.uns.ac.rs*

(Manuscript received in final form September 17, 2024)

Abstract—The territory of the Mura-Drava-Danube Transboundary Biosphere Reserve is large and includes natural and built-up areas that local communities and tourists use during their outdoor work-related or recreational activities. These activities are affected by the outdoor thermal conditions, especially in the age of changing climate. In this paper we investigate micrometeorological and outdoor thermal comfort conditions in different natural and built-up environments at the area of the Bačko Podunavlje Biosphere Reserve. We chose one clear and calm day every month from October 2020 to June 2021, and performed measurements simultaneously at three different locations: settlement, riverside, and lake at midday hours. The results showed that thermal conditions differ between the different built-up and natural areas, and built-up areas tend to experience up to 7% less cold stress during the colder period than the other two sites according to the physiological equivalent temperature (PET) index. On the other hand, built-up area experiences more frequent strong and extreme heat stress during the warmer months. These and more detailed results presented in the paper indicate the most comfortable periods for outdoor activities in different natural or built-up environments.

Key-words: Mura-Drava-Danube Transboundary Biosphere Reserve, micrometeorological measurements, thermal comfort, physiological equivalent temperature (PET), modified physiological equivalent temperature (mPET)

1. Introduction

Biosphere reserves are *'learning places for sustainable development'*. They serve as testing grounds for interdisciplinary approaches to understanding and dealing with changes and interactions between social and ecological systems, in addition to conflict prevention and management of biodiversity. They are places that tackle global challenges by providing local solutions. The main idea that is promoted by establishing biosphere reserves is to offer solutions reconciling the conservation of biodiversity with its sustainable use. There are currently 738 biosphere reserves in 134 countries, including 22 transboundary sites (*https://en.unesco.org*).

According to *Pool-Stanvliet* and *Coetzer* (2020), biosphere reserves have a responsibility to promote and support interdisciplinary and transdisciplinary research that is relevant to society. The complex interaction between people and the natural environment is embedded in biosphere reserves, and it is this interconnectedness that drives sustainability science. Their aim is to conserve biodiversity, demonstrate sustainable development, undertake research and monitoring, and educate and train at the local level.

In the large area of Bačko Podunavlje Biosphere Reserve (BPBR), there are both natural areas and built-up areas - settlements whose population lives and works inside the biosphere reserve area. Built-up areas mainly consist of mid-rise family houses, which are not very densely built. Natural areas inside the BPBR are complex and different in terms of vegetation types, species, and presence of water bodies (see details in Section 2.1). Along with the global climate change issues, various types of land use and land cover influence the microclimatological conditions and thermal characteristics in different areas of the biosphere reserve. Climate change impacts land use by altering vegetation patterns, affecting agricultural practices, and shifting biodiversity, and can lead to both challenges, such as increased extreme weather events and water scarcity, and opportunities, such as extended growing seasons and new agricultural prospects. The area of BPBR is large with multiple types of human activities, such as agriculture, forestry, fishing, tourism, etc. Tourism activities in biosphere reserves are encouraged as a part of their sustainable development strategy (*Mondino* and *Beery*, 2019). As stated by *Jamaliah* and *Powell* (2017), ecotourism development in biosphere reserves require further adaptation planning and policies, to ensure robust and proactive measures that are capable of responding to climate change threats. Nature based touristic activities, such as activities in biosphere reserves are mostly performed outdoors, so they require fine weather and comfortable thermal conditions (*Milošević et al.*, 2020). Impacts on these biological systems are driven by natural processes, such as climate change and human development. Therefore, knowledge about climate and biometeorological conditions in specific areas is important for adequate planning of human activities and sustainable development of the area. Analyses

of the instrumental records represent the best available means to document recent climate change (*Hamilton et al.,* 2020).

In this study we analyzed the 10-year data from the nearby Sombor official meteorological station. The data from Sombor official station included morning, midday, and evening records (0700, 1400, 2100 CET). Based on that data we selected midday hours as the hours when most human activities take place. Additionally, we performed a series of micrometeorological measurements in three different sites inside the Bačko Podunavlje Biosphere Reserve (BPBR). The sites represent different types of environments, one built-up, and two natural sites: blue and green. These sites were selected because of their specific natural conditions, but also because of the activities of the local population that live and work in this area, and visitors who often come to the riverside and lake for recreation.

Site specific micrometeorological studies were already used in various studies and areas. Some of them examined the impact of different level of built-up areas and the presence of green and blue areas (e.g., *Milošević et al.* 2022a, 2022b; *Vasić et al.,* 2022), or effects of artificial and natural shade including the efficiency of different types and location of the vegetation (e.g., *Colter et al.* 2019; *Milošević et al.* 2017), or the effects of different cooling strategies (e.g., *Vanos et al.,* 2020; *Anderson et al.,* 2022). These studies indicate that there are differences in thermal conditions even if they are located at a close distance from each other. However, most of the studies that are dealing with natural and protected areas rely on the data obtained from the official weather stations, without assessment of site-specific thermal conditions (*Bleta et al.,* 2014; *Brosy et al.* 2014; *Basarin et al.,* 2014, 2018; *Pecelj et al.,* 2017; *Błażejczyk et al.,* 2021a). Consequently, usually the analyses were done using the average monthly or daily data. As stated in *Basarin et al.* (2014), daily and hourly values of air temperature, relative humidity, wind speed, precipitation, and cloud cover would be beneficial for better understanding different bioclimatic conditions of the area. These are the gaps that present study fills. Even though previous studies do not provide site specific data, they provide very useful insight into long-term conditions.

There are fewer studies dealing with bioclimatic conditions of non-urban areas compared to the studies that assess urban bioclimatic conditions. However, the ones that do bioclimatic analysis of the non-urban areas, usually use indices such as physiological equivalent temperature (PET) (*Farajzadeh* and *Matzarakis*, 2012; *Basarin et al.,* 2014; *Milošević et al.,* 2020), or universal thermal climate index (UTCI) (*Basarin et al.*, 2017; *Pecelj et al.*, 2017; *Błażejczyk et al.,* 2021b). It is found that these indices are suitable for bioclimatic assessment, because they are easy to understand and use ºC as a unit which is familiar for majority of people.

The aim of this study is to evaluate the impact of different surroundings (built-up area, green-blue area, and blue area) of a protected area on human

bioclimatic conditions, using the measured data from specific micro-locations. Such measurements give insight into the specific microclimatological conditions of the area, that have an impact on human outdoor activities. The main objective of measurements was to identify the most convenient environments in midday hours during the different seasons (autumn, winter and summer). The study of *Błażejczyk et al.* (2021a) shows that for active forms of recreation in natural environments, autumn, winter, and spring months are more convenient than summer months due to very oppressive weather in summer months, especially in south (Serbia, southern Ukraine). Due to the fact that weather/climate influences and affects people during their activities, it is useful to examine the bioclimatic conditions, and to apply a classification and assessment (*Matzarakis*, 2006, 2010). Micrometeorological measurements of this kind provide valuable information for human activities planning according to the most comfortable hours of the day, which contributes to sustainable development of the area (*Milošević et al.*, 2020). Investigating bioclimatic conditions in these sites contributes to planning mentioned activities and sustainable management of the area.

2. Study area, data, and methods

2.1. Study area

The Bačko Podunavlje Biosphere Reserve (BPBR) is situated on the peripheral northwestern part of Serbia, western part of the Autonomous Province of Vojvodina, that is in the west of its geographical-historical unit – Bačka. Towards the inner part of Serbia, the border of the biosphere reserve is drawn towards the borders of cadastral municipalities of numerous settlements. Biosphere reserve covers an area of 176,635 ha, within which there are three zones: a core (11,242 ha), a buffer zone (45,744 ha), and a transition zone (119,649 ha). Since 2021, the Bačko Podunavlje Biosphere Reserve has been an integral part of the the first transboundary UNESCO Biosphere Reserve (Mura-Drava-Danube Biosphere Reserve), that stretches across five countries Austria, Slovenia, Croatia, Hungary, and Serbia (*UNESCO,* 2022). The population of the biosphere reserve is estimated at 147, 405 inhabitants. They live in 26 settlements (according to the results of the latest census in 2011), in the town of Sombor and municipalities Odžaci, Bač, and Bačka Palanka (*Obradović et al.*, 2021).

Natural and cultural values of the Bačko Podunavlje Biosphere Reserve are, through the territories of the neighboring countries, connected with 700 kilometers long ecological corridor along the Mura, Drava, and Danube rivers. The Mura-Drava-Danube Biosphere reserve is also known by the informal name “European Amazon” (*Stojanović*, 2018). The area of the Bačko Podunavlje Biosphere Reserve is the largest conserved floodplain complex in

the upper course of the Danube River in Serbia, and one of the largest floodplains along the middle section of the Danube. The area has a specific combination of ecological conditions: it is situated in the contact zone between the central and southeastern European forest zone with steppes, and it has characteristic hydrological dynamics. The primary habitats are: alluvial forests, Pannonian salt steppes and salt marshes, mesotrophic standing waters, natural eutrophic lakes, muddy river shores, alluvial wetlands, wet meadows, sand deposits, river islets, sand shores, floodplains, oxbows, abandoned river beds, meanders (*UNESCO,* 2016). The floodplain complex along the Danube has rich fauna, in particular: Bechstein's bat (*Myotis bechsteinii*), otter (*Lutra lutra*), and red dear (*Cervus elaphus*). A prime butterfly area (PBA) called "Gornje Podunavlje"exists in Bačko Podunavlje Biosphere Reserve: In total, 156 taxa of butterflies have been recorded in this area. The floodplain is also very important as a fish spawning site (*UNESCO,* 2022). The area of the BPBR includes five protected areas: the Gornje Podunavlje Special Nature Reserve, the Karađorđevo Special Nature Reserve, the Tikvara Nature Park, the Šuma Junaković Nature Heritage Site, and the Bukinski Hrastik Regional Nature Park (*Tucakov,* 2018).

According to the Köppen-Geiger climate classification, this region has a Cfb climate (temperate climate, fully humid, and warm summers, with at least four Tmon ≥ + 10 °C) (*Kottek et al.,* 2006). The mean monthly air temperature ranges from −0.1 °C in January to 21.9 °C in July. The mean annual precipitation is 612 mm. Average wind speeds are from 1.7 m/s for SSW direction to 3.1 m/s for N direction (*Milošević et al.,* 2020).

2.2. Data and methods

In this study we used two datasets:

1. For background information we used long-term data from Sombor meteorological station, for the period 2010–2019.
2. For the specific bioclimatic assessment in three particular sites, monthly series of micrometeorological measurements (from October 2020 to June 2021) was performed using Kestrel 5400 Heat Stress Meter.

General long-term climate characteristics of the BPBR area are assessed with data from the official meteorological station of Sombor (45° 46' N 19° 09' E, 88 m a.s.l.). This station is operated by the Republic Hydrometeorological Service of Serbia and is closest to the area of interest (63–66 km away from all three locations). Sombor meteorological station is located in natural surroundings bordering the suburban area (*Milošević et al.,* 2020). Since the distance of the Sombor official station from the areas of interest is quite large, micrometeorological campaign was performed monthly from October 2020 to June 2021. The measurement sites are located at a short distance from each other inside the Bačko Podunavlje Biosphere Reserve, but they are different in terms

of vegetation types, presence of water bodies, and a level of build-up area. These locations include village Vajska (built-up area), lake Provala (blue area), and Berava as southern part of small river Živa, in the past meander of the Danube (blue and green area) (*Fig. 1*).

The measurement campaigns were planned and conducted in the following manner. We chose one clear and calm day every month from October 2020 to June 2021, and performed measurements simultaneously at three different locations: settlement Vajska (grey/ built-up area), riverside Berava (green-blue area), and lake Provala (blue area). Measurements were performed from 12:00 to 15:00 p.m. (Central European Time CET). Midday hours were selected for measurements, because during these hours wind speeds and cloud cover are low. Measurement data for November 2020 and March 2021 were not presented due to the high percent of missing values (>5%) for globe temperature (T_g), which affect the calculation of mean radiant temperature (T_{mrt}) and consequently the PET and mPET outcome. The analysis of the results was done by splitting the results in colder (October, December, January, February) and warmer (April, May, June) months.

We used three mobile Kestrel 5400 Heat Stress Trackers (*Fig. 1*) to measure air temperature (T_a in °C), relative humidity (*RH* in %), wind speed (v in m^{-1}), and globe temperature (T_g in °C) with one-minute temporal resolution. 1-minute values were later averaged to 15-minute values for the analysis. The measurements were performed at approximately 1.1 m height representing the center of gravity of the human body for standing subjects (ISO 7726, 1998). The Kestrel Heat Stress Trackers were deployed at least 10 minutes before the start of the measurement time to allow sensors to adjust to the atmospheric conditions at the site. The instruments were calibrated according to the manufacturers specifications, and their accuracy complies with ISO 7726 (1998) standards for sensor measurement range and accuracy (*Table 1*). Similar measurement settings were already used in previous studies (*Milošević et al.*, 2020, 2022).

Fig. 1. Study area and measurement instruments in three different sites: 1) blue-green area – riverside Berava; 2) blue area – lake Provala and 3) built-up area – settlement Vajska (Source: photos by authors; *figure by Stojanović* and *Savić*, 2013)

Table 1. Accuracy, resolution, and range of Kestrel 5400 Heat Stress Tracker sensors

Sensor	**Accuracy (+/-)**	**Resolution**	**Range**
Air temperature	0.5 ºC	0.1 ºC	-29.0 to 70.0 ºC
Relative humidity	±2% RH	0.1% RH	10 to 90 % 25 ºC non-condensing
Wind speed	Larger than 3% of reading, least significant digit of 20 ft/min	0.1 m/s	0.6 to 40.0 m/s
Globe temperature	1.4 ºC	0.1 ºC	-29.0 to 60.0 ºC

For the bioclimatic analysis and outdoor thermal comfort assessment, mean radiant temperature (T_{mrt}), physiologically equivalent temperature (PET) and modified physiologically equivalent temperature (mPET) were selected. T_{mrt} is calculated using the formula from *Thorsson et al.,* (2007):

$$Tmrt = \left[(\mathrm{T}g + 273.15)^4 + \frac{1.1 \cdot 10^8 \cdot v^{0.6}}{\varepsilon \cdot D^{0.4}} \cdot (Tg - Ta) \right]^{1/4}$$

where air temperature, T_a, globe temperature, T_g, and wind speed, v were obtained from in situ measurements, D represents the globe diameter (mm), and ε is the globe emissivity.

With the calculated T_{mrt}, and measured values for T_a, *RH*, and *v*, including default values for personal characteristics (age, height, weight, clothing, and work metabolism), we calculated PET and mPET values for each of the measurement sites. The physiologically equivalent temperature (PET) index is one of the most commonly used thermal indices in temperate climates (*Pecelj et al.*, 2021; *Coccolo,* 2016), and it uses widely known unit (°C), which makes the interpretation of the results easier for people less familiar with human biometeorology (*Brosy et al.*, 2014). According to *Höppe* (1999), PET represents "the air temperature at which, in a typical indoor setting (without wind and solar radiation), the energy budget of the human body is balanced with the same core and skin temperature as under the complex outdoor conditions to be assessed". PET index is based on a two-node thermo-physiological heat-balance model (Munich Energy-balance Model for Individuals (MEMI)), and the mean radiant temperature (T_{mrt}) (*Höppe,* 1999).

The modified physiologically equivalent temperature (mPET) is developed by *Chen* and *Matzarakis* (2018). It uses a multi-node heat transport model equal to the Fiala model (*Fiala et al.,* 2001), and a self-adapting multi-layer clothing model, which simulates water vapor resistance. Due to the integration of clothing variability according to the thermal conditions, mPET gives improved, more realistic representation of human thermal comfort (*Chen* and *Matzarakis*, 2018). The calculations of both PET and mPET indices were performed using the RayMan model (*Matzarakis et al.*, 2007, 2010b). PET classes are categorized according to thermal sensation and physiological stress level of humans (*Matzarakis* and *Mayer,* 1996) and are presented in the *Table 2*. mPET uses the same classification scale.

Table 2. PET index threshold values for the thermal sensation and the physiological stress level of humans (after *Matzarakis* and *Mayer*, 1996).

PET (°C)	Thermal sensation	Physiological stress level
<4.1	Very cold	Extreme cold stress
4.1–8.0	Cold	Strong cold stress
8.1–13.0	Cool	Moderate cold stress
13.1–18.0	Slightly cool	Slight cold stress
18.1–23.0	Comfortable	No thermal stress
23.1–29.0	Slightly warm	Slight heat stress
29.1–35.0	Warm	Moderate heat stress
35.1–41.0	Hot	Strong heat stress
>41.0	Very hot	Extreme heat stress

3. Results

3.1. Background information

The data for background information on weather conditions in the study area are obtained from the official weather station in Sombor. This weather station records the values of meteorological conditions at 7:00, 14:00, and 21:00 (CET). *Fig. 2* shows average values of air temperature and relative humidity for the period 2010–2019.

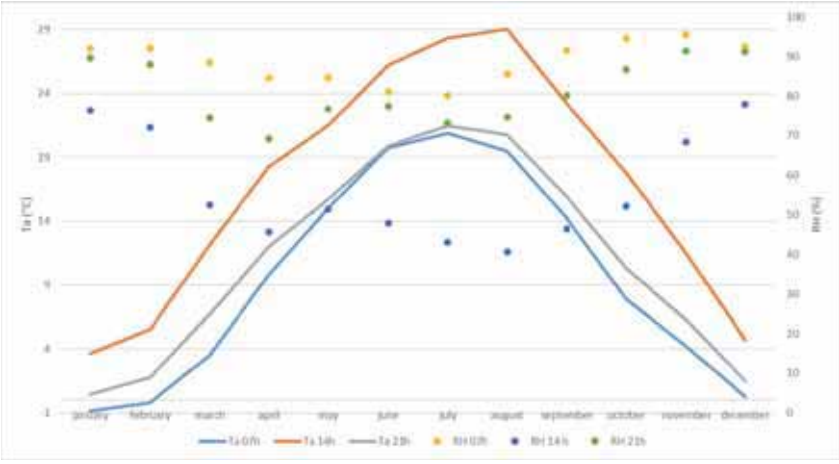

Fig. 2. Climate data obtained from Sombor official meteorological station (average values of T_a and *RH*) for the period 2010-2019 at 7:00, 14:00 and 21:00 (CET).

The results show that the temperatures are positive most of the time, except for the early morning temperatures in January and February. As expected, the highest T_a and the lowest *RH* are observed in the midday hours (14:00). It can also be noticed that the dynamics of *RH* values are showing direct inverse relationship to air temperature, which has already been reported in previous studies (e.g., *Yang et al.*, 2020; *Dunjić et al.*, 2021).

If we compare 10-year (2010-2019) average monthly midday hour (14:00) T_a and *RH* values from the official weather station (in Sombor) with the average measured T_a and *RH* values in the three selected sites: 1) blue-green area – riverside Berava; 2) blue area – lake Provala, and 3) built-up area – settlement Vajska, we can notice that the values are slightly different (*Table 3*).

Table 3. 10-year average monthly midday (14:00) T_a and *RH* values (official weather station Sombor) and average measured T_a valuesin three selected sites in the biosphere reserve

Site	October	December	January	February	April	May	June
Sombor	17.7	4.7	3.6	5.5	18.3	21.5	26.2
Site 1-R	20.5	4.8	4.8	14.5	22.6	25.9	30.7
Site 2-L	19.4	4.7	5.6	13.5	22.0	25.6	31.4
Site 3-S	20.0	5.0	5.4	13.1	23.9	26.5	30.8

Higher air temperatures in the specific sites in the biospehere reserve during the measurement days compared to the 10-year monthly average from the official weather station is observed in almost all months except for the winter months, December and January. This is due to the selection of the micrometeorological measurement days, where calm and clear days were chosen. Data from the official weather station in Sombor represent averaged monthly data at 14:00 (CET), from the 10-year period, which included clear and cloudy days. When it comes to micrometeorological measurements, calm and clear days are usually selected, because they secure minimal wind interference, stable atmospheric conditions, accurate solar radiation measurements, and reduced possibilities for errors by the device. Stable conditions provide that measurements are representative to the selected micro-location, because many instruments tend to be sensitive to rapid changes in environmental conditions (strong winds, precipitation, cloud cover that block or diffuse solar radiation, etc.), which can cause errors or require frequent recalibration (*Arya*, 2001; *Oke*, 1987). Other reason for this difference is that official weather station is located not very close to the measurement sites, but that is the closest that exists. The official weather station in Sombor is approximately 65 km away from the measurement locations, so T_a and *RH* data obtained from this station served as

the background referent dataset but cannot be representative for the microclimatological conditions at the certain sites. Therefore, we performed a series of micrometeorological measurements, to provide more detailed assessment of bioclimatic conditions inside the biosphere reserve.

3.2. Micrometeorological measurements

3.2.1. Air temperature

In the colder period (October, December 2020, and January, February 2021), the highest average air temperature was observed at the riverside (T_{aver}=11.15 ºC). In the other two locations (settlement and lake), the average air temperatures in the colder period were slightly lower (T_{aver}=10.9 ºC and 10.77 ºC respectively). The maximum average air temperature was also recorded at the riverside (T_{max}=23.4 ºC), while lower average maximum temperatures were observed at the lake Provala (T_{max}=21.90 ºC), and settlement Vajska (T_{max}=20.95 ºC). At the settlement measurement site, the highest minimum temperatures were recorded (T_{min}=2.90 ºC). The largest temperature range (20.80 ºC) and standard deviation (6.80) were observed at the riverside measurement location (*Table 4*).

In the warmer period, however, the highest average air temperature was observed in the settlement (T_{aver}=27.11 ºC), while at the other two locations average air temperatures were lower and quite similar (T_{aver}=26.42 ºC at the riverside, and 26.37 ºC at the lake). The highest extreme air temperatures (maximum and minimum) were also observed in the settlement (T_{max}=33.25 ºC, and T_{min}=22.55 ºC), while slightly lower maximum and minimum air temperatures were observed at other locations. The lake measurement site had the largest temperature range (12.99 ºC). Standard deviations were lower in warmer period compared to the colder period, and their values ranged from 3.07 (settlement) to 4.08 (lake).

Table 4. Main statistical characteristics of air temperature (T_a), globe temperature (T_g), relative humidity (*RH*), wind speed (*v*), Mean Radiant Temperature (T_{mrt}), physiologically equivalent temperature (PET) and modified physiologically equivalent temperature (mPET) in diverse urban environments of the Bačko Podunavlje Biosphere Reserve in the colder period (measurement period October, December, January, February; 12-15 CEST), and in the warmer period (measurement period April, May, June; 12–15 CEST).

	Ta			Tg			RH			v			Tmrt			PET			mPET		
Envir.	**S**	**R**	**L**	**S**	**R**	**L**	**S**	**R**	**L**	**S**	**R**	**L**	**S**	**R**	**L**	**S**	**R**	**L**	**S**	**R**	**L**
Colder period (October, December, January, February; 12-15 p.m. CEST)																					
Aver.	10.90	11.15	10.77	19.95	18.05	17.92	56.67	57.81	58.08	0.97	1.24	1.29	39.41	34.67	36.17	18.14	15.49	15.60	19.50	17.17	17.29
max	20.95	23.40	21.90	34.32	33.20	31.75	79.20	81.40	82.10	1.57	2.18	2.43	64.88	59.77	68.48	35.40	33.70	32.10	32.70	31.50	30.40
min	2.90	2.60	3.67	6.44	3.87	4.90	36.95	39.60	39.85	0.41	0.00	0.00	9.88	3.14	7.06	3.90	-0.30	0.90	7.80	3.90	5.10
range	18.05	20.80	18.23	27.88	29.33	26.85	42.25	41.80	42.25	1.15	2.18	2.43	55.00	56.63	61.42	31.50	34.00	31.20	24.90	27.60	25.30
stdev	6.24	6.80	6.17	9.59	9.54	8.81	13.14	14.22	13.58	0.29	0.46	0.59	17.57	16.34	18.51	10.88	11.04	10.32	8.62	8.91	8.29
Warmer period (April, May, June; 12-15p.m. CEST)																					
Aver.	27.11	26.42	26.37	40.15	39.44	39.59	40.52	42.10	42.09	0.72	0.93	1.07	59.49	61.98	63.60	41.37	41.07	41.38	37.72	37.45	37.76
max	33.25	32.45	32.79	49.75	51.25	49.90	57.13	68.80	64.71	1.27	2.00	2.11	75.39	78.68	87.32	52.60	54.90	55.70	46.30	48.20	49.00
min	22.55	19.70	19.80	28.30	27.80	28.52	29.76	29.69	28.25	0.00	0.00	0.17	28.30	27.80	33.86	27.60	26.80	27.60	26.50	26.90	26.90
range	10.70	12.75	12.99	21.45	23.45	21.38	27.37	39.11	36.46	1.27	2.00	1.94	47.09	50.88	53.45	25.00	28.10	28.10	19.80	21.30	22.10
stdev	3.07	3.59	4.08	5.16	6.60	6.71	8.81	10.41	10.25	0.23	0.45	0.55	9.51	12.92	14.35	6.00	7.44	8.48	4.58	5.72	6.59

Note: Abbreviations of measurement locations are as follows: S - settlement, R - riverside, L - lake

More detailed insight into temporal variability of air temperature at the three measurement locations is presented in *Figs. 3* and *4*, where the differences between the air temperatures between measurement sites are presented. In the colder period, air temperature differences recorded in December were quite similar at all locations, and their variability was low (between -1 °C and 1 °C) during the measurement hours. Similar results were observed in the January measurement campaign, but with a higher temperature range (between -2 °C, in the early afternoon, and 1.5 °C). In October, the air temperatures, in general, were higher than in other months from the colder period. Therefore, the air temperature differences were higher and more dynamic than in other colder months. The greatest differences were observed between the riverside and lake (~10 °C), where the air temperature was higher by the lake, in the early afternoon hours, but later in the midafternoon, the air temperature was higher by the riverside. Similar dynamics but with a lower temperature range were observed between the settlement and the lake. Inverse dynamics was observed between the settlement and river, where in the early afternoon, air temperatures were higher in the settlement than by the riverside, but lower in the settlement than by the riverside in the later afternoon. In February, the most intensive differences were observed in temperature differences between the riverside and lake (up to almost 9 °C). Similar dynamics, but with a lower temperature range

were noticed when observing the differences between the other two locations. The observed differences in air temperature between the locations can be attributed to different topoclimatic conditions, but also to local weather patterns. Different topoclimatic conditions at each site contribute to diffeences in air temperature and its variability. For example, the lake site has a moderating effect on temperature, leading to higher temperatures in its surroundings during the early afternoon as the water absorbs and slowly releases heat. On the other hand, the riverside experiences more dynamic temperature changes due to the moving water, which may cool the surrounding area in the early afternoon but can warm up quickly later in the day as solar radiation increases. The differences observed between the settlement and the riverside and lake sites can also be linked to topoclimatic influences, such as urban heat retention in the settlement due to built-up structures and slightly reduced vegetation. The inverse dynamics observed between the settlement and the riverside sites likely result from the differences in heat retention. Local weather patterns such as varying cloud cover, wind patterns, or humidity levels could enhance or mitigate the temperature differences at specific times of day. Additionally, the influence of the broader climate conditions cannot be neglected, as it sets the overall context, within which these topoclimatic and weather-related effects occur.

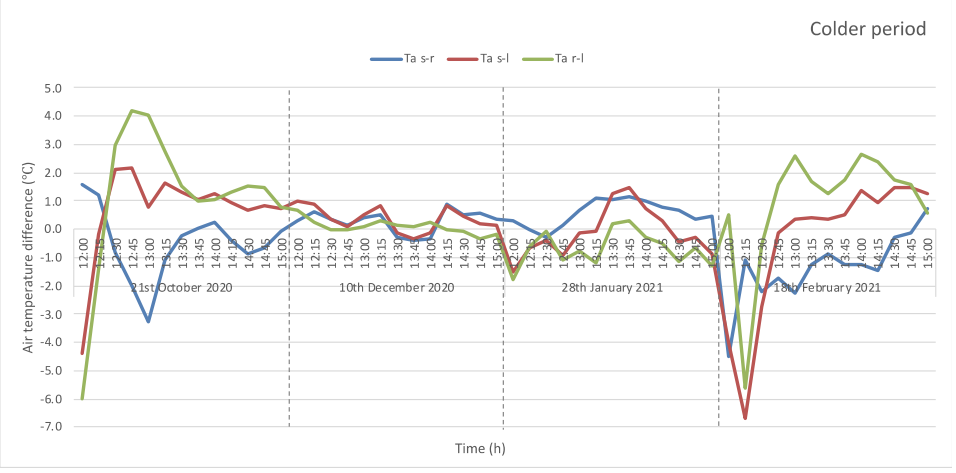

Fig. 3. Temporal variability of differences in air temperature at the three measurement locations in the colder period.

In the warmer period (*Fig. 4*), the dynamics between temperature differences were also observed but with the lower ranges than in the colder months. The highest temperature differences were observed in May 2021,

between the riverside and lake measurement locations (up to 8 °C). In April 2021 and June 2021, the most intensive differences (up to 4 °C and 5 °C, respectively) occurred between settlement and riverside, in the early afternoon.

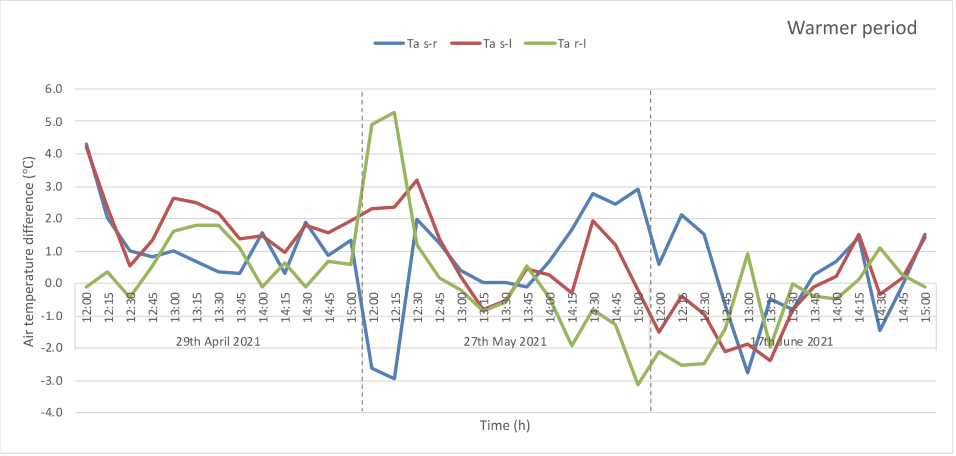

Fig. 4. Temporal variability of differences in air temperature at the three measurement locations in the warmer period.

3.2.2. Relative humidity

In the colder period (October, December, 2020 and January, February, 2021), average relative humidity values were the same at the lake and riverside measurement sites (RH_{aver}=58%), and slightly lower in the settlement (57%). Similarly, the highest maximum and minimum relative humidity values were observed at the lake measurement site, followed by the riverside and the settlement site (*Table 3*).

In the warmer period (April, May, and June 2021), the average relative humidity values at the riverside and lake sites were the same (42% and 42%), while at the settlement site, a slightly lower value of average relative humidity was observed (41%). The values of maximum and minimum *RH* were observed at the riverside site, and this site showed a larger range than the other two locations (*Table 3*).

Temporal dynamics of *RH* in colder period (Fig. 5) show the greatest differences between the riverside and lake measurement sites in the earlier hours (around noon). In February the differences between the two sites go up to ~14%, and higher levels are observed at the lake site. The lowest differences occur

between the settlement and riverside sites (up to ~7% higher *RH* in settlement earlier hours). In the colder period, it is possible that at some sites *RH* values are different than expected. For example, at the settlement site in the early afternoon hours *RH* is higher than at the riverside site. This is likely to happen when the temperature in settlement is higher during the night hours, which causes higher overnight moisture retention in the air, and the moisture is not fully evaporated by noon which leads to higher *RH* values in the settlement site. Additionally, built-up structures in the settlement act as barriers that reduce wind speed and affect mixing of the air. With less wind, moisture tends to stay trapped near the surface of the settlement area which can cause higher *RH* values.

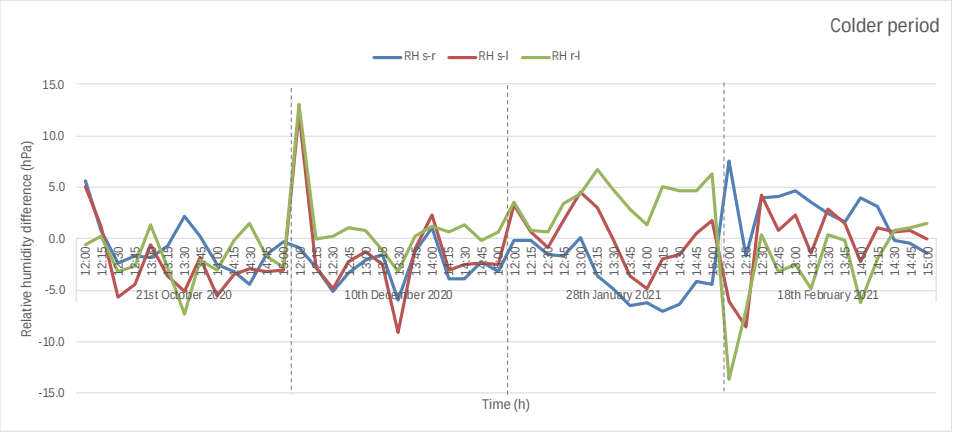

Fig. 5. Temporal variability of differences in relative humidity at the three measurement locations in the colder period.

Temporal dynamics of *RH* in the warmer period (Fig. 6) is similar as in the colder period. The greatest differences are observed between the settlement and riverside sites in April, when *RH* was up to 14% higher at the riverside than in the settlement.

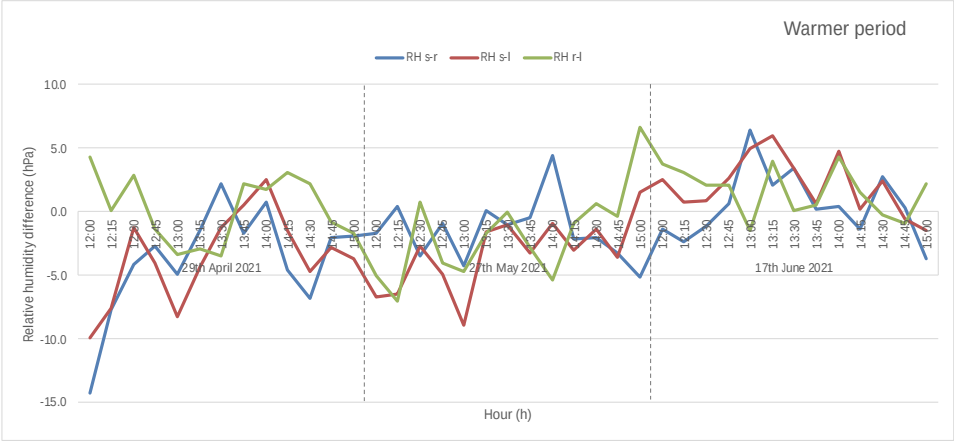

Fig. 6. Temporal variability of differences in relative humidity at the three measurement locations in the warmer period.

3.2.3. Globe temperature

In the colder period, on average, T_g was up to 2 °C higher in the settlement than in the other two locations (*Table 3*). Maximum and minimum T_g values are also observed in settlement. However, in the warmer period, the average difference between the measurement sites was lower (less than 1 °C). It is nteresting that maximum and minimum T_g values were observed at the riverside site. However, the differences are very low (less than 1 °C). More detailed temporal dynamics of T_g is showed in *Figs. 7* and *8*.

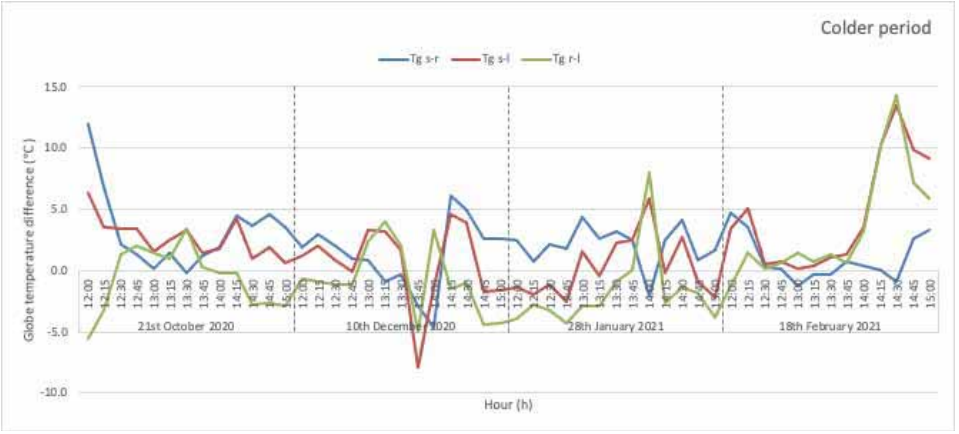

Fig. 7. Temporal variability of differences in globe temperature at the three measurement locations in the colder period.

Temporal dynamics in the colder period shows that larger differences between the sites occurred in the later measurement hours. The largest difference in T_g (~14 ºC) was observed between the riverside and lake site in February in the later measurement hours (*Fig. 7*). This could be due to the temporal cloud cover presence at the lake site that reduced the impact of solar radiation, which affected globe temperature that absorbs radiant heat from all directions, allowing the thermometer to give an integrated measure of the thermal environment (ASHRAE, 2017).

In the warmer period, the largest differences were observed in June around noon, when T_g was 21 ºC higher by the lake than by the riverside. In the earlier warmer months, T_g showed low differences among the measurement sites (*Fig.* 8).

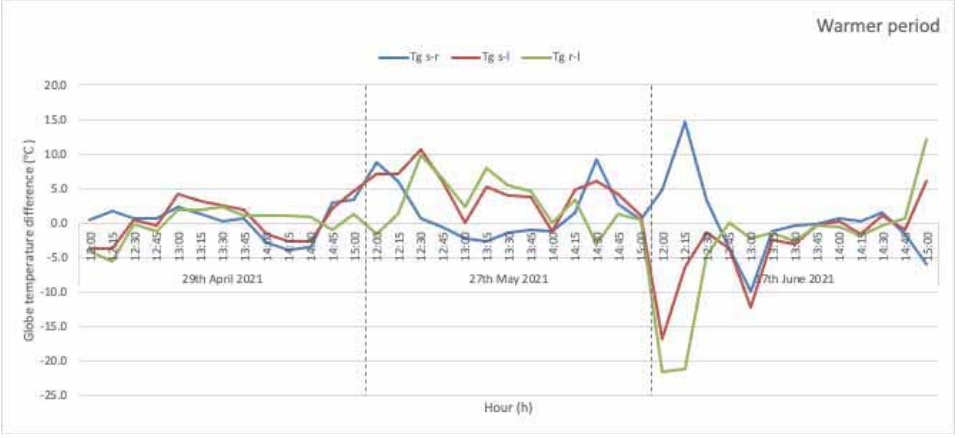

Fig. 8. Temporal variability of differences in globe temperature at the three measurement locations in the warmer period.

3.2.4. Wind speed

In this type of microclimate measurements, usually calm and clear days are selected (e.g. *Milošević et al.*, 2020, 2022a, 2022b). Therefore, we selected calm days with lower wind speeds for this measurement campaign. As it is shown in *Table 3*, the higher average and maximum wind speeds in both colder and warmer periods were observed by the lake (v_{aver}=1.29 m/s), followed by the riverside site (v_{aver}=1.24 m/s). In the settlement the average windspeeds were the lowest (v_{aver}=0.97 m/s). This is due to the nature of the measurement sites, and slight differences in the presence of natural and built barriers (vegetation, buildings). The differences did not show any regular pattern between the sites, so a detailed temporal analysis is not provided.

3.3. Bioclimatological parameters

3.3.1. Mean radiant temperature

The highest average values of T_{mrt} in the colder period are observed in the settlement ($T_{mrt\ aver}$ = 39.41 ºC), followed by the lake site ($T_{mrt\ aver}$ = 36.17 ºC), and slightly lower values are observed at the riverside site ($T_{mrt\ aver}$ = 34.67 ºC). Maximum values, however, are calculated at the lake site ($T_{mrt\ max}$ = 68.48 ºC), followed by the settlement site ($T_{mrt\ max}$ = 64.88 ºC), and the riverside site ($T_{mrt\ max}$ = 59.77 ºC). In the settlement, the highest minimum values are recorded ($T_{mrt\ min}$ = 09.88 ºC), followed by the lake site ($T_{mrt\ min}$ = 07.06 ºC), and the riverside site ($T_{mrt\ min}$ = 03.14 ºC) in the colder period (*Table 3*).

In the warmer period, the highest average T_{mrt} is calculated for the lake site ($T_{mrt\ aver}$ = 63.60 ºC), followed by the riverside site ($T_{mrt\ aver}$ = 61.98 ºC) and the settlement ($T_{mrt\ aver}$ = 59.49 ºC) (*Table 3*).

Temporal analysis of T_{mrt} in colder period indicates that in most colder months the settlement had higher T_{mrt} values compared to two other sites. It also shows that the greatest differences occurred in later measurement hours. However, the largest difference is observed between riverside and lake in February afternoon, and the measured difference was 44.6 ºC (*Fig. 9*). The lake site is likely to have lower T_{mrt} due to the cooling effect of larger water body, that can absorb significant thermal mass and release it slower than vegetated areas, and built-up areas. On the other hand, settlement site experiences higher T_{mrt} due to the presence of buildings and roads, that can absorb and re-emit the heat faster.

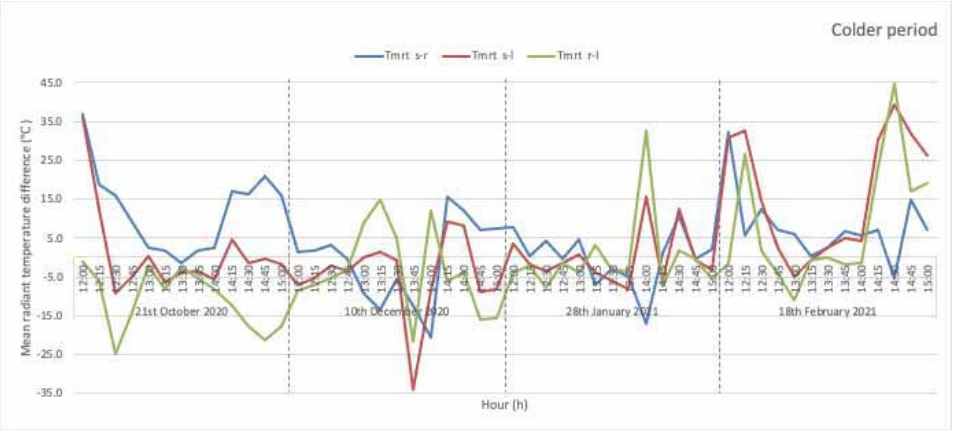

Fig. 9. Temporal variability of differences in mean radiant temperature at the three measurement locations in the colder period.

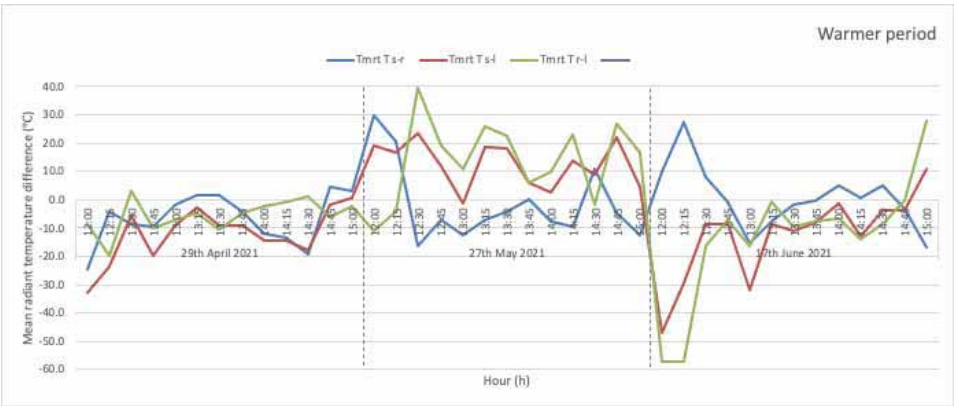

Fig. 10. Temporal variability of differences in mean radiant temperature at the three measurement locations in the warmer period.

Temporal analysis in the warmer period (Fig. 10) shows that the dynamics of T_{mrt} differences among the sites is lower than in the colder period, especially in April. In May, the highest differences between the riverside site and the lake site are observed (up to 40 ºC). In June, the difference in T_{mrt} between the riverside and lake site peaked, but in opposite direction, which means that the values of T_{mrt} at the lake site were 57 ºC higher than at the riverside site around noon. By the end of the measurements, the differences between the sites were lower. In all three warmer months, the most prominent differences occurred in the early measurement hours, around noon. That indicated the influence of the different shading effects on T_{mrt} on each site (*Milošević et al.*, 2022b) in times of high exposure to solar radiation (*Aminipouri et al.*, 2019).

3.3.2. PET and mPET – colder period

Table 3 shows that in the colder period, the highest average PET and mPET values are recorded at the settlement site (PET_{aver} = 18.14 ºC; $mPET_{aver}$ = 19.50 ºC) followed by the lake and riverside site where very similar average PET values are calculated (PET_{aver} = 15.60 ºC and PET_{aver} = 15.49 ºC, respectively). Similar results are observed for the mPET index values for the lake and riverside site ($mPET_{aver}$ = 17.29 ºC and $mPET_{aver}$ = 17.17 ºC, respectively). This means that on average, settlement is under no thermal stress, while lake and riverside site are under slight cold stress (13-18ºC), in colder months. The highest maximum PET values are also recorded in the settlement site (PET_{max}=35.4 ºC), which indicates that strong heat stress occasionally happens in the colder months in the settlement site. However, maximum mPET value is lower in settlement ($mPET_{max}$=32.7 ºC), indicating the presence of moderate heat stress. In other sites, there is occasional moderate heat stress, when maximum PET and mPET

values are recorded. Minimum PET values (<4.1 ºC) show that there is extreme cold stress observed in all three sites during the colder period (*Table 3*). Minimum mPET values indicate the presence of an occasional extreme cold stress only at riverside site, while at the settlement site and lake sites, minimum mPET values indicate the occurrence of strong cold stress (*Table 3*). These results of short term, location-specific micro-measurements are in good accordance with the previous study by *Basarin et al.* (2014) that examined PET in the broader area of Gornje Podunavlje Special Nature Reserve, using the long-term data from the official Sombor meteorological station. They reported the occurrence of extreme cold stress (PET_{aver}<4 °C) in the period from December to February.

Temporal analysis of PET in the colder period is shown in *Fig. 11a*. In October, the differences between the measurement sites were larger in the beginning of the measurement hours, around noon. The greatest difference was recorded between the settlement site and riverside site (peak $PET_{diff\ s\text{-}r}$ =14.6ºC). In the other three months (December, January, and February), the greatest differences occurred in the afternoon, around 2 p.m. During most of the measurement time, settlement site showed higher PET values comparing to both the riverside site and lake site. However, riverside site and lake site PET values did not show regular pattern in the colder period, but the PET values difference between them was the largest ($PET_{diff\ r\text{-}l}$ =16.6ºC). These results are in good accordance with the T_{mrt} results.

Fig. 11b shows temporal variation of mPET values during the measurement hours. An almost identical trend as with PET values can be observed. The difference between the PET and mPET index values is that mPET values are slightly lower compared to the PET values.

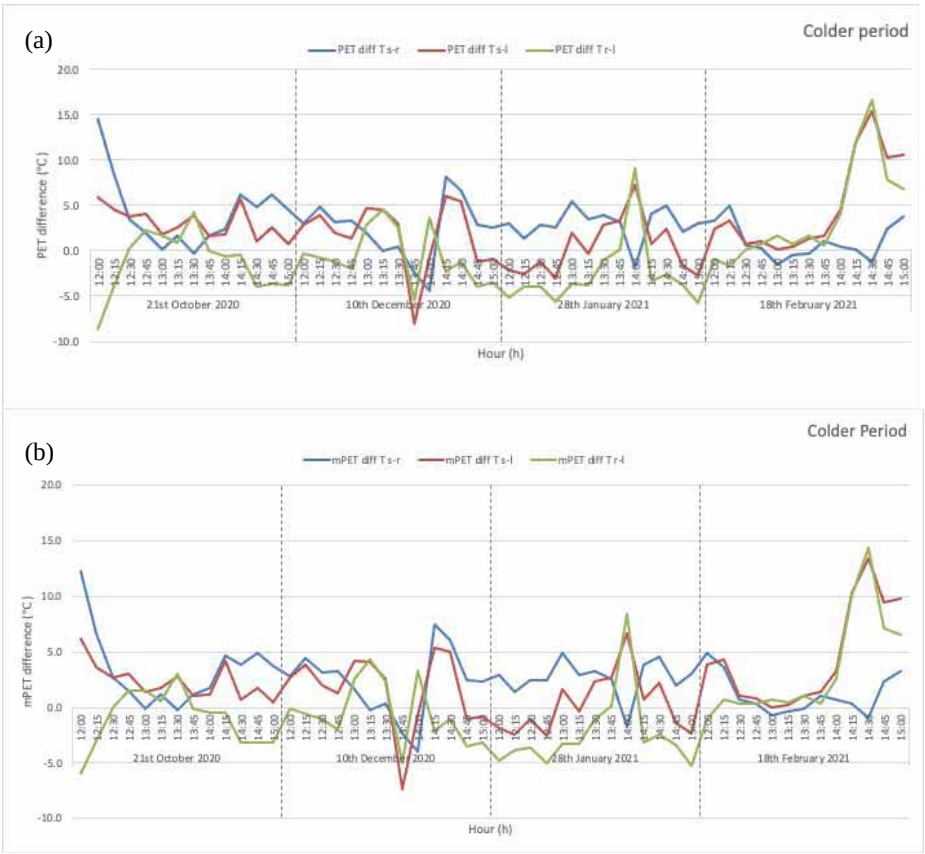

Fig. 11. Temporal variability of differences in PET (a) and mPET (b) values at the three measurement locations in the colder period.

Fig. 12a shows frequency analysis (%) of physiological stress according to the PET index in all three measurement sites. The results show that at the majority of the time, all three sites experience some level of cold stress, 58%, 56%, and 51%, at the lake, riverside, and settlement, respectively. Riverside site experiences extreme cold stress 23% of the time, while settlement site experiences moderate cold stress 29% of the time. However, there is a significant percent of heat stress for all three sites as well (46% at the settlement, 48% at the riverside, and 36% at the lake site) even though this is defined as colder period.

Fig. 12b shows the frequency of different levels of thermal stress according to the mPET index. According to the mPET values, all sites experience cold

stress at almost half of the measurement time (53%, 49%, and 58% at the riverside, settlement, and lake site, respectively). Extreme cold stress occurs only at the riverside site very rarely (4%). Similarly to the PET values, mPET values show significant percent of heat stress, 39%, 46%, and 35% for the riverside, settlement, and lake site, respectively. High percent of the heat stress at the measurement sites occur because October is included in the colder period, and the thermal conditions were not as cold as in the other colder months (*Fig. 12*).

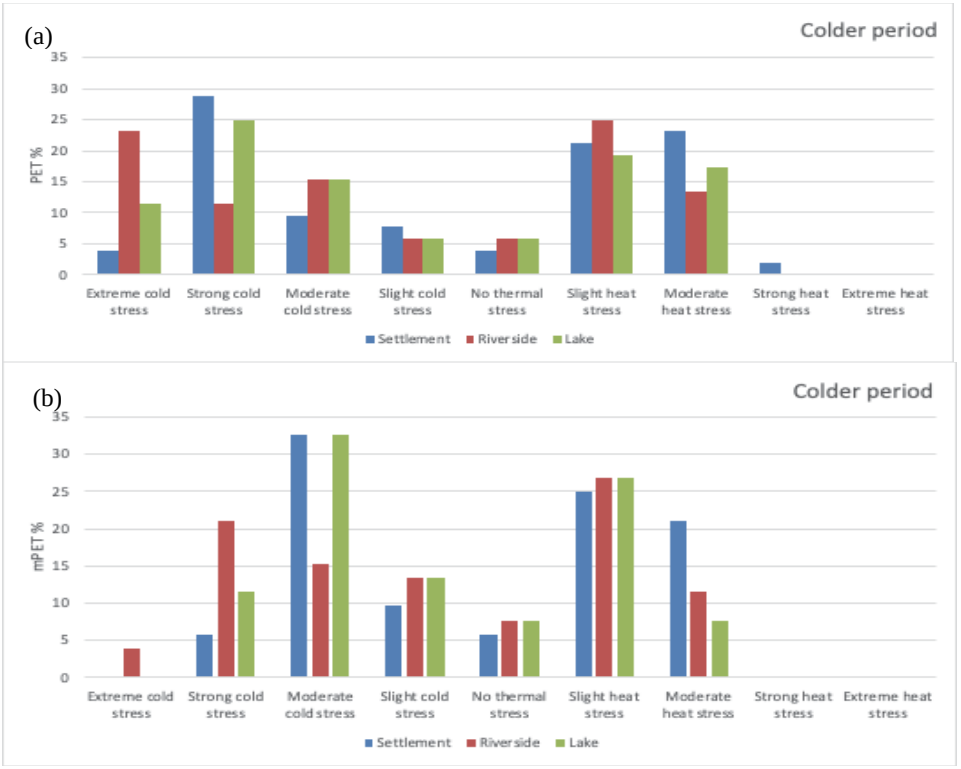

Fig. 12. Frequency analysis (%) of physiological stress according to PET (a) and mPET (b) indices at three measurement locations in colder period.

3.3.3. PET and mPET – Warmer period

In the warmer period, average PET values are quite similar for all of the three sites, with the differences less than 1 ºC. All three sites experience extreme heat stress during the warmer months in the midday hours (PET_{aver} = 41.37 ºC -

settlement, $PET_{aver} = 41.07$ ºC - riverside, $PET_{aver} = 41.38$ ºC -lake). Maximum PET values are recorded at the lake site ($PET_{max} = 55.7$ ºC) followed by the riverside site ($PET_{max} = 54.9$ ºC), and the settlemet site ($PET_{max} = 52.6$). Minimum PET values are similar for all three sites (differences less than 1 ºC), and it means that even when taking minimum PET values for all three sites in the warmer period during the midday hours, there is slight heat stress (*Table 3*).

mPET values for the warmer period show strong heat stress for all three sites, and the differences between the sites are also less than 1ºC ($mPET_{aver} = =37.72$ ºC - settlement, $mPET_{aver} = 37.45$ ºC - riverside, $mPET_{aver} = 37.76$ ºC - lake). Maximum mPET values for all three sites also indicate extreme heat stress, and similarly to the PET values, mPET values are the greatest at the lake site ($mPET_{max} = 49$ ºC), followed by the riverside site ($mPET_{max} = 48.2$ ºC), and settlement site ($mPET_{max} = 46.3$ ºC). Also, minimum mPET values are rather similar at all three sites, and also indicate the presence of the slight heat stress (*Table 3*).

Temporal analysis of PET values in the warmer period (*Fig. 13a*) shows that the dynamics of PET differences among the sites is lower than in the colder period, especially in April. In May, the differences between the measurement sites were slightly larger (up to 13.8 ºC between the riverside and lake sites). In June, the difference in PET values between the riverside and lake site peaked in opposite direction, meaning that the values of PET at the lake site were 26 ºC higher than at the riverside site around noon. By the end of the measurements, the differences between the sites were lower. The results are in good accordance with the results of the T_{mrt} analysis.

Fig. 13b shows temporal variation of mPET values during the warmer period. Almost identical trend as with PET values is recorded. The difference between the PET and mPET index values is that mPET values are slightly lower compared to the PET values. This trend is also noticed at the analysis of the colder period values of PET and mPET.

Fig. 13. Temporal variability of differences in PET (a) and mPET (b) values of the three measurement locations in the warmer period.

Frequency analysis of the PET values (*Fig. 14a*) in the warmer period show that all the measurement sites experienced some level of heat stress during the measurement campaigns in the warmer months. The settlement and riverside sites experienced extreme heat stress almost at 50% of the measured period. At the lake measurement site, strong heat stress was the most frequent thermal sensation. Slight and moderate heat stresses were noticed at about 10% of the measurement period. This means that all three sites experienced most frequently strong and extreme strong heat stress during the warmer months and during the midday hours (12–15h).

Frequency analysis of the mPET index (*Fig. 14b*) shows also that in the warmer period all sites are under some level of heat stress. The interesting thing is that the lake site according to the mPET index experiences moderate, strong, and extreme heat stress almost equally frequent. On the other hand, the settlement and riverside sites are under strong and extreme heat stress is more than 70% of the time in the midday hours.

It can be concluded that the lake site has more comfortable conditions compared to the settlement and riverside sites, due to the less frequent exposure to extreme heat stress. However, strong heat stress is often present at the lake site as well.

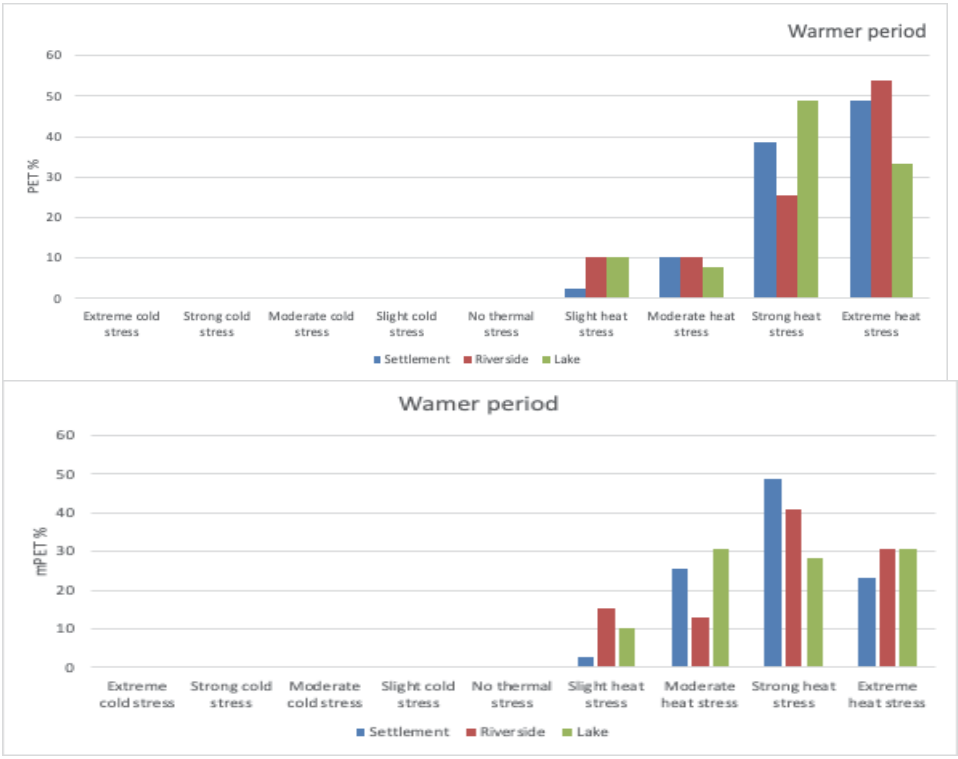

Fig. 14. Frequency analysis (%) of physiological stress according to PET (a) and mPET (b) indices at the three measurement locations in the warmer period.

4. Discussion

Natural areas such as the Mura-Drava-Danube Biosphere Reserve represent the corridor formed by the Danube and its tributaries, the Mura and Drava rivers, that forms a unique biotope network that is the habitat for many rare animal and plant species, and thus represents the most valuable continuous river landscape in Central Europe (*Mohl et al.*, 2020). At the same time, the definition of biosphere reserve states the importance of providing space for human activities as well. Therefore, it is important to analyze climate and bioclimate

characteristics of the area, with respect to the natural and built-up environment and land use types at the specific sites. In our study, we selected two different natural sites and one built-up site to perform bioclimatic analysis using human thermal comfort indices PET and mPET. The results show that thermal conditions between them are different in different parts of the year. The observed differences in bioclimatic parameters across the sites, although not always following a regular pattern, highlight the complexity of microclimatic interactions within the biosphere reserve. These differences suggest that local factors such as vegetation cover, water proximity, and human activities play significant roles in shaping the bioclimatic conditions.

Bioclimatic analysis of physiological stress according to PET index in all three measurement sites show at that majority of the time, all three sites experience some level of cold stress, 58%, 56%, and 51%, at the lake, riverside and settlement sites, respectively. The settlement site experiences up to 7% less cold stress than the riverside and lake sites. However, there is a significant percentage of heat stress for all three sites as well (46% at the settlement, 48% at the riverside, and 36% at the lake site), even though this is defined as colder period. This could be explained by the fact that October was included in the colder period for the analysis, and temperatures in October are higher than in the rest of the colder months.

Bioclimatic analysis in the warmer period shows that all the measurement sites experienced some level of heat stress during the measurement campaigns in the warmer months. The settlement and riverside sites experience extreme heat stress almost at 50% of the measured period. At the lake measurement site, strong heat stress was the most frequent thermal sensation. Slight and moderate heat stresses were noticed at about 10% of the measurement period. This means that all three sites experience most frequently strong and extremely strong heat stress during the warmer months and during the midday hours (12–15h), but the settlement site experiences up to 7% more strong and extreme heat stress categories than the other two sites.

Bioclimatic analysis in this article is done using micrometeorological data, which is obtained by measurements in clear and calm days. It can vary in the circumstances when stronger wind, cloud cover, and precipitation are present. 10-year background data from the official weather station in Sombor show that the cloud cover is the lowest in summer months, and the highest in winter months, and the average cloud cover during the year is 5.3/10.

Previous studies (*Farajzadeh* and *Matzarakis*, 2012; *Basarin et al.*, 2014; *Milošević et al.,* 2020) have also used the PET index to investigate bioclimatic conditions of different natural areas enable the comparison with the present study. For example, *Basarin et al.* (2014) assessed long-term bioclimatic conditions in the Special Nature Reserve „Gornje Podnavlje“, which is part of the Mura-Drava-Danube Biosphere Reserve. They reported that the most comfortable thermal conditions for outdoor ativities occur in the autumn and spring months of the year. During the period from November until February,

cold stress occurs in the reserve in more than 60% of the time (*Basarin et al.*, 2014). These results are in good accordance with the results from the present study, that also reports certain amount of cold stress in the colder part of the year (October to February) in both natural sites, and comfortable conditions only in the settlement site (according to PET_{aver}). *Basarin et al.* (2014) reported the highest amounts of heat stress during the meteorological summer season (June, July, and August), however, when analyzing the PET values of the midday hours (14h), they reported that heat stress occurs from May to September, and the periods with no thermal stress are observed in October and April. These results are confirmed in this study for the warmer period (April, May and June). In the study by *Milošević et al.* (2020) it is shown, that there are differences in thermal sensation and comfort at the same site but in different vegetation structures. They reported that there are differences in microclimatic conditions between the sites at even smaller distances in autumn (October 2019), where the most comfortable conditions during the midday hours are in the areas with the higher vegetation (forests), while in the more open areas, there is slight discomfort observed. In the present study, the differences between the different natural and built-up environments are emphasized.

Bioclimatic analysis provides us with very useful information about the differences in human thermal sensations that occur between the sites at different periods of the year. This is the first study that analyzed thermal conditions of the specific sites inside the large area of the transnational biosphere reserve, that are often used by local population and visitors. The information obtained indicates that the activities in the investigated sights should be organized according to the most comfortable period (*Milošević et al.*, 2020) of the year. For example, in the colder period of the year, tourists' activity should be encouraged in the more urbanized areas, promoting cultural heritage and social diversity of the BPBR. On the other hand, in the summer months, thermal conditions are more favorable at the lake site. Given the recreational function of the site, this is a reasonable choice. Local communities that perform other activities in the area, could also use this information to organize their work activities, if possible, in such manner that they avoid longer exposure in the midday hours in warmer months to prevent themselves from the heat stress related health issues.

Micrometeorological measurements of this kind provide valuable information for tourism zoning and visitors distribution according to the most comfortable periods of the year, which contributes to sustainable management of tourism activities (*Milošević et al.*, 2020). Though this study is the first micrometeorological field measurement conducted in this region, it gave important insights into micrometeorological differences between different natural and built-up environments. In order to contribute to long-term strategic planning of the activities and their sustainable management, longer measurements campaigns, more measurement sites in Serbian part, but also in parts of the reserve that belongs to other countries would be beneficial.

5. Conclusion

The area of BPBR is large and it belongs to an even larger area of the Drava-Mura-Danube Transboundary Biosphere Reserve. In the large area of the biosphere reserve, people are involved in all kinds of activities that require certain thermal conditions. In this study we gave the overview of the bioclimate conditions, in the colder and warmer parts of the year for specific, but different sites, to provide comprehensive results for all the users of the biosphere reserve area, including local population and visitors.

However, the study has its limitations, simultaneously the recommendations for future investigation.

- Measurement hours could be prolonged in order to identify the most comfortable time of the day for each location in different seasons. This implies that measurements should be done in all months of the year. Additionally, measurements in different weather types and climates could be performed.
- It would be useful to do similar studies in other countries that are part of the Mura-Drava-Danube Transboundary Biosphere Reserve and to compare the results.
- Bioclimatic questionnaire survey that accompanies the measurements would give more complete information about the thermal sensation of the locals and visitors the reserve.

The fact that the area selected for this study is a part of the first transnational park, the Mura-Drava-Danube Transboundary Biosphere Reserve indicates, that there is a significant potential that it becomes more popular for visits. Investigating climate conditions in the Bačko Podunavlje Biosphere Reserve (BPBR) might be the basis for planning human activities in order to preserve diverse natural and built-up areas in the BPBR in the age of climate change, as well as for sustainable use of natural resources of these fragile ecosystems. Extreme bioclimate conditions that occur in this area at certain hours can be considered as unsuitable for the activities of visitors and local population, while hours of lower levels of thermal stress or no thermal stress can be considered as good bioclimate conditions. Recognizing the variations in bioclimatic conditions is crucial for effective management of the protected area, as it emphasizes the need for tailored strategies that consider the unique microclimates of different zones within the reserve. The importance of these differences lies in their potential to influence decision-making processes related to habitat management, species conservation, and visitor activities. Integrating bioclimatic considerations into management plans can enhance the sustainability and usability of the biosphere reserve, aligning with the broader goals of conservation and sustainable development.

Acknowledgment: This research was supported by the Provincial Secretariat for Higher Education and Scientific Research, Autonomous Province of Vojvodina (Project 142-451-3485/2023-01/01). The authors gratefully acknowledge the financial support of the Ministry of Science, Technological Development and Innovation of the Republic of Serbia (Grants No. 451-03-66/2024-03/ 200125 & 451-03-65/2024-03/200125). The authors also acknowledge the financial support of the Ministry of Education, Science and Technological Development of the Republic of Serbia (Grant No. 451-03-9/2021-14/ 200125).

References

Aminipouri, M., Rayner, D., Lindberg, F., Thorsson, S., Knudby, A.J., Zickfeld, K., Middel, A. and *Krayenhoff, E.S.*, 2019: Urban tree planting to maintain outdoor thermal comfort under climate change: The case of Vancouver's local climate zones. *Build. Environ. 158*, 226–236. https://doi.org/10.1016/j.buildenv.2019.05.022

Anderson, V., Gough, W. A., Zgela, M., Milosevic, D., and *Dunjic, J.*, 2022: Lowering the Temperature to Increase Heat Equity: A Multi-Scale Evaluation of Nature-Based Solutions in Toronto, Ontario, Canada. *Atmosphere* 13(7), 1027. https://doi.org/10.3390/atmos13071027

Arya, S.P., 2001: Introduction to Micrometeorology (2nd ed.). Academic Press.

ASHRAE, 2017: *Handbook Fundamentals*. American Society of Heating, Refrigerating and Air-Conditioning Engineers (ASHRAE).

Basarin, B., Kržič, A., Lazić, L., Lukić, T., Đorđević, J., Janićijević Petrović, B. Ćopić S., Matić D, Hrnjak I. and *Matzarakis, A.*, 2014: Evaluation of bioclimate conditions in two special nature reserves in Vojvodina (Northern Serbia). *Carpathian J. Earth Environ.Sci. 9* (4), 93–108. https://www.researchgate.net/publication/287307211_Evaluation_of_bioclimate_conditions_in_two_special_nature_reserves_in_Vojvodina_Northern_Serbia

Basarin, B., Lukić, T., Bjelajac, D., Micić, T., Stojićević, G., Stamenković, I., Đorđević J., Đorđević T. and *Matzarakis, A.*, 2018: Bioclimatic and climatic tourism conditions at Zlatibor Mountain (Western Serbia). *Időjárás 122*, 321–343. https://doi.org/10.28974/idojaras.2018.3.6

Błażejczyk, A., Pecelj, M., Błażejczyk, K. and *Skrynyk, O.*, 2021a: Weather suitability for outdoor tourism in three European regions in first decades of the twenty-first century. *Int. J. Biometeorol. 65*, 1339–1356. https://doi.org/10.1007/s00484-020-01984-z

Błażejczyk, K., Nejedlik, P., Skrynyk, O., Agnieszka, H., Skrynyk, O., Błażejczyk, A., and *Mikulova, K.*, 2021b: Influence of geographical factors on thermal stress in northern Carpathians. *Int. J. Biometeorol. 65*, 1553–1566. https://doi.org/10.1007/s00484-020-02011-x

Bleta, A., Nastos, P. T. and *Matzarakis, A.*, 2014: Assessment of bioclimatic conditions on Crete Island, Greece. *Reg. Environ. Change 14*, 1967–1981. https://doi.org/10.1007/s10113-013-0530-7

Brosy, C., Zaninovic, K., and *Matzarakis, A.*, 2014: Quantification of climate tourism potential of Croatia based on measured data and regional modeling *Int. J. Biometeorol. 58*, 1369–1381. https://doi.org/10.1007/s00484-013-0738-8

Chen, Y.C. and *Matzarakis, A.*, 2018: Modified physiologically equivalent temperature—Basics and applications for western European climate. *Theor. Appl. Climatol. 132*, 1275–1289. https://doi.org/10.1007/s00704-017-2158-x

Coccolo, S., Kämpf, J., Scartezzini, J.L. and *Pearlmutter, D.*, 2016: Outdoor human comfort and thermal stress: A comprehensive review on models and standards. *Urban Climate 18*, 33–57. https://doi.org/10.1016/j.uclim.2016.08.004

Colter, K.R., Middel, A. C. and *Martin, C.A.*, 2019: Effects of natural and artificial shade on human thermal comfort in residential neighborhood parks of Phoenix, Arizona, USA. *Urban Forestry Urban Green. 44*, 126429. https://doi.org/10.1016/j.ufug.2019.126429

Dunjić, J., Milošević, D., Kojić, M., Savić, S., Lužanin, Z., Šećerov, I. and *Arsenović, D.*, 2021: Air Humidity Characteristics in "Local Climate Zones" of Novi Sad (Serbia) Based on Long-Term Data. *ISPRS Int. J. Geo-inf. 10*(12), 810. https://doi.org/10.3390/ijgi10120810

Farajzadeh, H. and *Matzarakis, A.*, 2012: Evaluation of thermal comfort conditions in Ourmieh Lake, Iran. *Theor. Appl. Climatol. 107*(3), 451–459. https://doi.org/10.1007/s00704-011-0492-y

Fiala, D., Lomas, K., and *Stohrer, M.*, 2001: Computer prediction of human thermoregulatory and temperature responses to a wide range of environmental conditions. *Int. J. Biometeorol. 45*, 143–159. https://doi.org/10.1007/s004840100099

Hamilton, J.P., Whitelaw, G.S., and *Fenech, A.*, 2001: Mean annual temperature and total annual precipitation trends at Canadian biosphere reserves. *Environ. Monitor. Assess. 67*(1), 239–275. https://doi.org/10.1023/a:1006490707949

Höppe, P., 1999: The physiological equivalent temperature–a universal index for the biometeorological assessment of the thermal environment. *Int. J. Biometeorol.* 43(2), 71–75.

ISO 7726, 1998: Ergonomics of the thermal environment—instruments for measuring physical quantities. International Standard, 2nd edn. International Organization for Standardization (ISO), Geneva.

Jamaliah, M.M. and *Powell, R.B.*, 2017: Ecotourism resilience to climate change in Dana Biosphere Reserve, Jordan. *J. Sustain. Tourism 26*(4), 519–536. https://doi.org/10.1080/09669582.2017.1360893

Kottek, M., Grieser, J., Beck, C., Rudolf, B. and *Rubel, F.*, 2006: World map of the Köppen-Geiger climate classification updated. *Meteorol. Zeit.* 15(3), 259–263. https://doi.org/10.1127/0941-2948/2006/0130

Matzarakis, A. and *Mayer, H.*, 1996: Another kind of environmental stress: thermal stress. *WHO newsletter* 18, 7–10.

Matzarakis A., 2006: Weather- and climate-related information for tourism. *Tour Hosp Plan Dev 3*, 99–115.

Matzarakis, A., Rutz, F. and *Mayer, H.*, 2007: Modelling radiation fluxes in simple and complex environments—application of the RayMan model. *Int. J. Biometeorol. 51*(4), 323–334. https://doi.org/10.1007/s00484-006-0061-8

Matzarakis A., 2010a: Climate change: temporal and spatial dimension of adaptation possibilities at regional and local scale. In: (ed. *Schott C*) Tourism and the implications of climate change: issues and actions, Emerald Group. *Bridging Tourism Theory Practice 3*, 237–259. https://doi.org/10.1108/S2042-1443(2010)0000003017

Matzarakis, A., Rutz, F. and *Mayer, H.*, 2010b: Modelling radiation fluxes in simple and complex environments: basics of the RayMan model. *Int. J. Biometeorol. 54*(2), 131–139. https://doi.org/10.1007/s00484-009-0261-0

Milošević, D. D., Bajšanski, I. V. and *Savić, S. M.*, 2017: Influence of changing trees locations on thermal comfort on street parking lot and footways. *Urban forest. Urban Green. 23*, 113–124. https://doi.org/10.1016/j.ufug.2017.03.011

Milosević, D., Dunjić, J., and *Stojanović, V.*, 2020: Investigating micrometeorological differences between saline steppe, forest-steppe and forest environments in northern Serbia during a clear and sunny autumn day. *Geographica Pannonica* 24 (3), 176–186. https://doi.org/10.5937/gp24-25885

Milošević, D., Middel, A., Savić, S., Dunjić, J., Lau, K. and *Stojsavljević, R.*, 2022a: Mask wearing behavior in hot urban spaces of Novi Sad during the COVID-19 pandemic. *Sci. Total Environ. 815*, 152782. https://doi.org/10.1016/j.scitotenv.2021.152782

Milošević, D., Trbić, G., Savić, S., Popov, T., Ivanišević, M., Marković, M., Ostojić M., Dunjić J., Fekete R. and *Garić, B.*, 2022b: Biometeorological conditions during hot summer days in diverse urban environments of Banja Luka (Bosnia and Herzegovina). *Geographica Pannonica 26*(1), 29–45. https://doi.org/10.5937/gp26-35456

Mohl, A., Korn-Varga, I. and *Györfi, E.*, 2020: The ecological corridor Mura-Drava-Danube and future five-country biosphere reserve. IUCN Guidelines for Conserving Connectivity through Ecological Networks and Corridors, Series 30, 104–106.

Mondino, E. and *Beery, T.*, 2019: Ecotourism as a learning tool for sustainable development. The case of Monviso Transboundary Biosphere Reserve, Italy. *J. Ecotourism 18*(2), 107–121. https://doi.org/10.1080/14724049.2018.1462371

Oke, T. R., 1987: Boundary Layer Climates (2nd ed.). Routledge.

Obradović, S., Stojanović, V., Kovačić, S., Jovanovic, T., Pantelić, M. and *Vujičić, M.*, 2021: Assessment of residents' attitudes toward sustainable tourism development-A case study of Bačko Podunavlje Biosphere Reserve, Serbia. *J. Outdoor Recreat. Tourism 35*, 100384. https://doi.org/10.1016/j.jort.2021.100384

Pecelj, M., Đorđević, A., Pecelj, M., Pecelj-Purković, J., Filipović, D. and *Šećerov, V.*, 2017: Biothermal conditions on Mt. Zlatibor based on thermophysiological indices. *Arch. Biol. Sciences 69*(3), 455–461. https://doi.org/10.2298/ABS151223120P

Pecelj, M., Matzarakis, A., Vujadinović, M., Radovanović, M., Vagić, N., Đurić, D. and *Cvetkovic, M.*, 2021: Temporal analysis of urban-suburban PET, mPET and UTCI indices in Belgrade (Serbia). *Atmosphere 12* (7), 916. https://doi.org/10.3390/atmos12070916

Pool-Stanvliet, R., and *Coetzer, K.*, 2020: The scientific value of UNESCO biosphere reserves. *South African J. Sci. 116*(1-2), 1–4. https://doi.org/https://doi.org/10.17159/sajs.2020/7432

Stojanović, V. and *Savić, S.*, 2013: Management challenges in special nature reserve'Gornje Podunavlje'and preparations for its proclamation of biosphere reserve. *Geographica Pannonica 17*(4), 98–105. https://doi.org/10.5937/GeoPan1304098S

Stojanović, V., 2018: What we have and what we are proud of. In (Ed. *Zagorac*), Bačko Podunavlje Biosphere reserve – Nature with people. Novi Sad: Provincial secretariat for urban planning and environmental protection. Institute for nature conservation of Vojvodine Province.

Thorsson, S., Lindberg, F., Eliasson, I., and *Holmer, B.*, 2007: Different methods for estimating the mean radiant temperature in an outdoor urban setting. *Int. J. Climatol. 27*, 1983–1993. https://doi.org/10.1002/joc.1537

Tucakov, M., 2018: Functions of the Biosphere Reserve. In (Ed. *Zagorac*), Bačko Podunavlje Biosphere Reserve - Nature with people. Novi Sad: Provincial secretariat for urban planning and environmental protection. Institute for nature conservation of Vojvodine Province.

UNESCO, 2016: Bačko Podunavlje Biosphere Reserve Nomination Form. Man and the Biosphere (MAB) Programme – Biosphere reserve nomination form – January 2013 – June, 2016.

UNESCO, 2022: Bačko Podunavlje Biosphere Reserve, Serbia. Retrieved January 19, 2022, from https://en.unesco.org/biosphere/eu-na/backo-podunavlje

Vanos, J.K., Wright, M.K., Kaiser, A., Middel, A., Ambrose, H. and *Hondula, D.M.*, 2020: Evaporative misters for urban cooling and comfort: effectiveness and motivations for use. *Int. J. Biometeorol. 66*, 357–369. https://doi.org/10.1007/s00484-020-02056-y

Vasić, M., Milošević, D., Savić, S., Bjelajac, D., Arsenović, D., and *Dunjić, J.*, 2022: Micrometeorogical measurements and biometeorogical survey in different urban settings of Novi Sad (Serbia). *Bull. Serbian Geograph. Soc. 102*(2), 45–66. https://doi.org/10.2298/GSGD2202045V

Yang, X., Peng, L. L., Chen, Y., Yao, L., and *Wang, Q.*, 2020: Air humidity characteristics of local climate zones: A three-year observational study in Nanjing. *Build. Environ. 171*, 106661. https://doi.org/10.1016/j.buildenv.2020.106661

DOI:10.28974/idojaras.2025.3.5

IDŐJÁRÁS

Quarterly Journal of the HungaroMet Hungarian Meteorological Service
Vol. 129, No. 3, July – September, 2025, pp. 339–355

K-means clustering of precipitation in the Black Sea Region, Türkiye

Aslı Ulke Keskin[1], **Gurkan Kır**[1], and **Utku Zeybekoglu**[2,*]

[1]*Faculty of Engineering, Ondokuz May University*
55139, Atakum, Samsun, Türkiye

[2]*Boyabat Vocational School of Higher Education*
Sinop University
57200 Boyabat, Sinop, Türkiye

**Corresponding Author e-mail: utkuz@sinop.edu.tr*

(Manuscript received in final form May 31, 2024)

Abstract— In recent years, there has been a significant uptick in the frequency of disasters stemming from the impacts of global climate change. In response, both nationally and internationally, various studies are being conducted to mitigate these effects. Classifying regions affected by climate change into similar classes based on climate parameters is crucial for applying consistent methodologies in studies conducted within these regions. This approach will help determine the most appropriate strategies for mitigating the effects of climate change in these regions. The study utilized observational records of annual precipitation from 31 stations in the Black Sea Region, sourced from the Turkish State Meteorological Service, covering the data spans the period between 1982 and 2020. Cluster analysis was conducted using the k-means algorithm. The optimal cluster among those formed was determined through the silhouette index analysis. The study suggests that the optimal number of clusters is 2.

Key-words: clustering, precipitation, silhouette analysis, k-means

1. Introduction

Climate, characterized by extreme values of meteorological parameters such as precipitation, temperature, and wind, represents the collective state of the atmosphere for a specific location over a defined time interval (*Demircan et al.*, 2017). Until the mid-1950s, long-term averages of these parameters were generally assumed to remain unchanged. As we progress into the 20th century, rapid industrial developments have resulted in the unplanned consumption of natural resources, increased environmental pollution in tandem with population growth, and the release of substantial amounts of greenhouse gases into the atmosphere. Consequently, greenhouse gases, with their heat-retaining capacity, have begun to induce changes in climate parameters over time. These alterations in climate parameters are commonly referred to as global climate change (*Turkes*, 2010; *Ozkoca*, 2015). On a global scale, climate change manifests its local effects through various disasters such as floods, droughts, and storms. Global climate change, the focus of numerous articles in recent years, is intensifying its impact day by day, negatively affecting human life in economic and social spheres. Consequently, studies aimed at understanding climate change and implementing measures to address it are becoming increasingly crucial. Most studies conducted in the context of climate change reveal that there are changes in the intensity and distribution of precipitation throughout the year, rather than significant changes in total annual precipitation values. In this context, the change in standard duration precipitation for Izmir meteorological station on a station basis was studied by *Karahan* (2012), on a regional scale for the Southeastern Anatolia Region by *Karahan et al.* (2008), for the Aegean Region by *Karahan* (2011, 2019), and for the Eastern Black Sea Region meteorological stations by *Karahan et al.* (2015). The mentioned studies used different methods, and it was shown that there were changes in precipitation intensities in the first and second half of the measurement period. Similarly, *Zeybekoglu* and *Karahan* (2018) presented increasing and decreasing trends in standard duration rainfall intensities for all meteorological stations operated by the Turkish State Meteorological Service (TSMS) at the national scale. Additionally, *Karahan* (2022) conducted a detailed analysis of the increasing and decreasing trends in rainfall intensities, as well as the dates of occurrence of deterioration in rainfall intensity.

The classification of regions based on similar climate parameters is believed to contribute to various studies such as combating climate change, protecting water resources, and land use planning. *Erinc* (1949) classified precipitation and temperature data from 53 meteorological stations in Türkiye into four different climate zones using the Thornthwaite method. This study marks the first comprehensive and detailed classification of Türkiye's geography with sufficient data. *Turkes* (1996) classified precipitation data of Türkiye using the Normalization Procedure method proposed by Kraus in 1977. In the study, seven different regions were identified during the period 1930–1993. *Kulkarni* and *Kripalani* (1998) identified similarity classes of Indian rainfall data using the

Fuzzy c-means method. They divided 306 meteorological observation stations into four different clusters using rainfall data for the period 1871–1984. *Unal et al.* (2003) determined the similarity classes of temperature and precipitation data covering the period between 1951–1998 in Türkiye using five different clustering methods. The study concluded that the Ward's method was the most effective among the preferred methods. *Soltani* and *Modarres* (2006) categorized precipitation data from 28 meteorological stations in Iran into similar classes using hierarchical and non-hierarchical clustering methods. The study identified eight different classes, employing Ward's method and the k-means algorithm. *Sonmez* and *Komuscu* (2008) utilized the k-means algorithm in their study to identify precipitation regions in Türkiye. They analyzed monthly total precipitation series obtained from 148 meteorological stations covering the period 1977-2006, identifying six different precipitation regions. *Sahin* (2009) utilized monthly average temperature, monthly relative humidity, and monthly total precipitation data from 150 meteorological stations to determine similar climate classes in Türkiye. They employed the Ward's, Kohonen artificial neural network, and fuzzy artificial neural network methods to identify seven different regions. *Dikbas et al.* (2012) identified six different precipitation regions in Türkiye using the fuzzy c-means method with records from 188 stations spanning 1967–1998. *Sahin* and *Cigizoglu* (2012) determined sub-climatic and sub-precipitation regime classes in Türkiye using the Ward's and fuzzy artificial neural network methods. They analyzed precipitation, temperature, and humidity data from 232 meteorological stations for the period 1974–2002, identifying seven precipitation regime zones and seven climate zones. *Fırat et al.* (2012) identified 7 different regions with similar characteristics using the k-means method for the similarity classes of annual total precipitation measured at 188 precipitation observation stations in Türkiye, covering the period 1967–1998. *Iyigün et al.* (2013) conducted a cluster analysis study using precipitation, temperature, and relative humidity data, employing the Ward's method. The data were obtained from 244 meteorological stations in Türkiye, covering the period from 1970 to 2010. As a result of the study, *Iyigün et al.* (2013) identified 14 different clusters. *Rau et al.* (2017) divided the rainfall data of the Peruvian Pacific slope and coast into regions with similar characteristics. They utilized the regional vector method and the k-means algorithm, identifying nine different rainfall regions. *Zeybekoglu* and *Ulke Keskin* (2020) conducted a clustering analysis of precipitation intensity series using the fuzzy c-means algorithm, incorporating latitude, longitude, and altitude values of observation stations. They found that 95 meteorological observation stations in Türkiye formed five different clusters. Additionally, the authors clustered various hydrometeorological parameters of the same study area using clustering algorithms and silhouette index analysis (*Kir at al.*, 2023a, b, c). According to temperature observations, clusters with similar characteristics were determined using k-means and FCM algorithms. According to silhouette index analysis, the optimal number of clusters was determined as 5 for k-means and

4 for FCM; however, the 5-cluster approach suggested by k-means was deemed the most ideal distribution (*Kir et al.,* 2023a). Similar stations based on wind speed characteristics were determined using both K-Means and FCM. According to silhouette index analysis, the optimal number of clusters was determined as 5 and 4 for k-means and FCM, respectively; however, the 5-cluster approach determined by k-means was suggested as the most ideal distribution (*Kir et. al.,* 2023b). In the authors' research (*Kir et al.,* 2023c), clusters with similar characteristics were formed using FCM based on precipitation records from stations in the region. According to the silhouette index analysis of the clusters they created, they concluded that the most appropriate approach is a 4-cluster distribution (*Kir et al.,* 2023c).

In the literature, numerous studies have been conducted in Türkiye and abroad on the determination of climate classes. When examining these studies, it is evident that precipitation and temperature are predominantly emphasized as climate parameters. Additionally, the evaluation of results obtained by using fuzzy c-means and k-means methods together with silhouette analysis is not very common in climate studies (*Kir,* 2021). Accordingly, the aim of this study is to cluster meteorological observation stations in the Black Sea Region with similar characteristics using the k-means algorithm based on precipitation records. The most appropriate number of clusters was determined through Silhouette index analysis for different cluster numbers with the k-means algorithm.

2. Materials and methods

2.1. Materials

In this study, annual total precipitation records for the period 1982–2020 (39 years) from 31 observation stations operated by Turkish State Meteorological Service in the Black Sea Region were utilized. It was ensured that the data had a record length of at least 30 years for statistical adequacy (*Kite,* 1991).

The observation stations used in the study are located in 17 different provinces in the Black Sea Region. Eleven of the stations are located in the Western Black Sea (Düzce, Akçakoca, Bolu, Zonguldak, Bartın, Amasra, Kastamonu, İnebolu, Bozkurt, Tosya, Sinop), 10 in the Central Black Sea (Samsun, Bafra, Çorum, Osmancık, Amasya, Merzifon, Tokat, Zile, Ordu, Ünye), and the remaining 10 in the Eastern Black Sea region (Giresun, Şebinkarahisar, Trabzon, Akçaabat, Gümüşhane, Bayburt, Rize, Pazar, Artvin, Hopa).

In the Black Sea Region, where the precipitation regime is oriented in the north-south direction, precipitation is observed in all seasons. The precipitation regime in areas close to each other can exhibit significant differences. While the average annual precipitation in Rize, one of the provinces with the highest precipitation in the region, is 2284 mm, the average annual precipitation in Trabzon, which is right next to it, is 846 mm. The precipitation rate in the Black

Sea Region is high in the east (e.g., Rize: 2284 mm; Hopa: 2329 mm), but it decreases towards the Central Black Sea with the decrease in elevation (e.g., Samsun: 716 mm; Amasya: 465 mm; Çorum: 450 mm). In the Western Black Sea, the precipitation rate increases again with elevation (e.g., Zonguldak: 1227 mm; Bartın: 1051 mm). Additionally, when the data used in the study are evaluated, the average annual precipitation of the Black Sea Region is 901 mm. The geographical distribution of the stations is shown in *Fig. 1*, while the geographical location of the stations and basic statistical information on meteorological observations are provided in *Tables 1* and *2*.

Fig. 1. Spatial distribution of the stations.

Table 1. Geographical details of the stations

Station	Latitude (N)	Longitude (E)	Elevation (m)
Düzce	40°50'37.3"	31°08'55.7"	146
Akçakoca	41°05'22.2"	31°08'14.6"	10
Bolu	40°43'58.4"	31°36'07.9"	743
Zonguldak	41°26'57.3"	31°46'40.5"	135
Bartın	41°37'29.3"	32°21'24.8"	33
Amasra	41°45'09.4"	32°22'57.7"	73
Kastamonu	41°22'15.6"	33°46'32.2"	800
İnebolu	41°58'44.0"	33°45'49.0"	64
Bozkurt	41°57'34.9"	34°00'13.3"	167
Tosya	41°00'47.5"	34°02'12.1"	870
Çorum	40°32'46.0"	34°56'10.3"	776
Osmancık	40°58'43.3"	34°48'04.0"	419
Sinop	42°01'47.6"	35°09'16.2"	32
Amasya	40°40'00.5"	35°50'07.1"	409
Merzifon	40°52'45.5"	35°27'30.6"	754
Samsun	41°20'39.0"	36°15'23.0"	4
Bafra	41°33'05.4"	35°55'28.9"	103
Tokat	40°19'52.3"	36°33'27.7"	611
Zile	40°17'45.6"	35°53'25.8"	719
Ordu	40°59'01.7"	37°53'08.9"	5
Ünye	41°08'34.8"	37°17'34.8"	16
Giresun	40°55'21.7"	38°23'16.1"	38
Şebinkarahisar	40°17'13.9"	38°25'09.5"	1364
Gümüşhane	40°27'35.3"	39°27'55.1"	1216
Trabzon	40°59'54.6"	39°45'53.6"	25
Akçaabat	41°01'57.0"	39°33'41.4"	3
Bayburt	40°15'16.9"	40°13'14.5"	1584
Rize	41°02'24.0"	40°30'04.7"	3
Pazar	41°10'39.7"	40°53'57.5"	78
Artvin	41°10'30.7"	41°49'07.3"	613
Hopa	41°24'23.4"	41°25'58.8"	33

Table 2. Basic statistics of rainfall records (mm)

Station	Mean	Std. Dev.	Min.	Max.	Var.	Skew.
Düzce	818.43	124.54	527.0	1084.9	0.15	0.05
Akçakoca	1127.62	175.42	742.6	1460.7	0.16	-0.06
Bolu	562.52	87.20	382.5	754.5	0.16	0.05
Zonguldak	1226.74	187.03	818.8	1740.1	0.15	0.76
Bartın	1051.11	161.86	753.1	1350.3	0.15	0.14
Amasra	981.62	180.33	660.6	1412.6	0.18	0.53
Kastamonu	521.17	119.95	338.2	870.5	0.23	0.93
İnebolu	1053.78	136.43	728.0	1330.0	0.13	-0.26
Bozkurt	1185.50	238.58	498.2	1595.7	0.20	-1.00
Tosya	476.32	100.40	250.8	735.5	0.21	0.34
Çorum	450.19	88.94	242.9	633.8	0.20	0.06
Osmancık	423.41	117.67	234.6	794.4	0.28	0.82
Sinop	718.52	133.87	333.3	1008.1	0.19	-0.30
Amasya	465.32	88.68	293.4	682.0	0.19	0.58
Merzifon	444.35	93.29	225.1	703.3	0.21	0.50

Table 2. continued

Station	Mean	Std. Dev.	Min.	Max.	Var.	Skew.
Samsun	716.47	93.16	562.8	999.1	0.13	0.86
Bafra	763.16	162.47	424.0	1141.4	0.21	0.37
Tokat	444.26	72.10	313.3	593.0	0.16	0.09
Zile	444.82	90.04	237.4	639.0	0.20	0.25
Ordu	1058.36	128.71	787.2	1433.8	0.12	0.64
Ünye	1185.51	160.85	906.6	1532.8	0.14	0.44
Giresun	1308.07	170.71	970.7	1743.4	0.13	1.09
Şebinkarahisar	568.64	91.91	345.8	741.9	0.16	-0.12
Gümüşhane	472.08	84.11	311.0	651.0	0.18	0.34
Trabzon	846.55	111.99	594.4	1044.6	0.13	-0.39
Akçaabat	721.37	111.71	494.0	1017.4	0.15	0.32
Bayburt	464.34	75.35	318.2	614.6	0.16	-0.03
Rize	2284.35	273.76	1694.0	3097.1	0.12	0.73
Pazar	2105.38	360.58	1326.8	2905.0	0.17	0.34
Artvin	721.41	132.51	425.1	1005.9	0.18	-0.12
Hopa	2329.73	372.30	1685.3	3379.5	0.16	1.07

When analyzing *Table 2*, the station with the lowest average annual total precipitation is Osmancık with 423.41 mm, while the station with the highest average annual total precipitation is Hopa with 2329.73 mm.

2.2. K-means algorithm

The k-means clustering algorithm (*Xin et al.,* 2011) is one of the simplest unsupervised and hard clustering algorithms. It is used to classify a given dataset into various clusters (*Vani et al.,* 2019).

Process steps of the algorithm:

- Step 1: Random centers are selected.
- Step 2: The distance between the centroids and the data points is calculated.
- Step 3: Data points are assigned to clusters based on the minimum Euclidean distance measure:

$$J_{KM}(X;V)= \sum_{i=1}^{c} \sum_{j=1}^{n} D_{ij}{}^{2}, \quad (1)$$

where V is a given centroid, c is the number of clusters, n is the number of iteractions, and D_{ij} is the Euclidean distance between each data points and centroid

- Step 4: New centroids are calculated:

$$V_i = \sum_{i=1}^{n_i} \frac{D_{ij}}{n_i}; 1 \leq i \leq c. \quad (2)$$

- Step 5: Check whether the new centroids are equal to the old centroids.
- Step 6: If the new centroids and the old centroids are equal, the algorithm terminates; otherwise, it goes back to step 2.

Input: V is the number of centroids (centers); x and y are the distance center values between the centroid and the data points; D_{ij} is the Euclidean distance between each data point and the centroids; c is the number of clusters, and n is the number of iterations.
Output: Number of clusters.

Advantages of the algorithm (*Vani et al.,* 2019):

- It is easy to understand and simple to implement.

Disadvantages of the algorithm(*Vani et al.,* 2019):

- Not effective for overlapping clusters.
- Ineffective for clustering heterogeneous data.
- Provides a local optimum of the squared error function.
- Randomly choosing the cluster centers may not yield optimal results.

2.3. Silhouette index analysis

In this method developed by *Rousseeuw* (1987), the suitability of each element in the dataset to the cluster to which it is assigned is defined by the silhouette index value obtained between [-1, +1]. A positive silhouette index value indicates that the element is assigned to the correct cluster, while a negative value indicates that the element is assigned to the wrong cluster. The silhouette index value indicates the degree of membership to the cluster to which the element is assigned. For example, a silhouette index value of +1 means that the element is definitely assigned to the correct cluster, while -1 means that the element is definitely assigned to the wrong cluster. The silhouette index value is calculated by the following formula (*Sonmez* and *Komuscu,* 2008; *Gunay Atbas,* 2008):

$$S(i) = \frac{min\{b(i,m)-a(i)\}}{max\{a(i), min(b(i,m))\}}, \quad (3)$$

where $a(i)$ refers to the average distance between point i and all other points in the same cluster, $b(i, m)$ is the average distance between point i and all points in cluster m.

3. Results

In this study, the k-means algorithm was utilized to identify clusters with similar characteristics using annual average temperature observations from 31 stations in the Black Sea Region, covering the period between 1982 and 2020. Analyses were performed using MATLAB R2016a. The maximum number of clusters was chosen as 5, which is less than the square root of the number of stations (*Karahan*, 2011, 2019; *Pal* and *Bezdek* 1995; *Zhang et al.*, 2008). Before cluster analysis of the observation records, these data were standardized using in the following formula (*Unal et al.*, 2003):

$$z = \frac{x_i - \bar{x}}{s}, \tag{4}$$

where x_i represents the standardized observation at rank i, $\bar{x}$ is the mean of the dataset. s is the standard deviation of the dataset, and z is defined as the standardized value (*Unal et al.*, 2003).

In the classification conducted for each cluster number from 2 to 5, using the k-means algorithm with the maximum number of clusters set at 5, the resulting clusters for the Black Sea Region wind speed series are illustrated in *Figs 2–5*, while statistical summary information of the clusters is provided in *Tables 3–6*.

The clusters formed when the number of clusters is selected as 2 are shown in *Fig. 2*. Upon analysis of the results, cluster A consists of 28 stations located in the Western, Central, and Eastern Black Sea regions. Cluster B consists of 3 stations located only in the Eastern Black Sea coastal region. *Table 3* presents the maximum, minimum, mean, and standard deviation values of annual total precipitation for the identified clusters.

Fig. 2. Spatial distribution of stations for 2 clusters.

Table 3. Statistical summary of precipitations for 2 clusters distribution (mm)

Cluster	Min.	Max.	Mean	Std. Dev.
A	423.41	1308.07	757.92	293.15
B	2105.38	2329.73	2239.82	118.62

The clusters obtained when the number of clusters is selected as 3 are shown in *Fig. 3*. Upon analysis of the results, it is observed that clusters A and B are separated as two sub-clusters of cluster A in the previous distribution. Additionally, it is noted that the Rize, Pazar, and Hopa stations, which maintained their integrity in the previous distribution, are assigned to cluster C. Thus, cluster A consists of 18 stations located in the Western, Central, and Eastern Black Sea regions. Cluster B consists of 10 stations located in the Western, Central, and Eastern Black Sea coastal areas. Cluster C consists of 3 stations located only in the Eastern Black Sea coastal area. *Table 4* presents the maximum, minimum, mean, and standard deviation values of annual total precipitation for the clusters.

Fig. 3. Spatial distribution of stations for 3 clusters.

Table 4. Statistical summary of precipitations for 3 clusters distribution (mm)

Cluster	Min.	Max.	Mean	Std. Dev.
A	423.41	818.43	566.49	135.95
B	846.55	1308.07	1102.49	133.00
C	2105.38	2329.73	2239.82	118.62

The clusters formed when the number of clusters is selected as 4 are shown in *Fig. 4*. Upon analysis of the results, it is observed that clusters C and D are separated as two sub-clusters of cluster C in the previous distribution. Additionally, it is noted that the Trabzon station, which was in cluster B in the previous distribution, is assigned to cluster A. Thus, Cluster A consists of 19 stations located in the Western, Central, and Eastern Black Sea regions. Cluster B consists of 9 stations located in the Western, Central, and Eastern Black Sea coastal areas. Clusters C and D consist of 1 and 2 stations, respectively, located only in the Eastern Black Sea coastal zone. Cluster C consists of only the Pazar station. Cluster D consists of the Rize and Hopa stations. *Table 5* presents the maximum, minimum, mean, and standard deviation values of annual total precipitation for the identified clusters.

Fig. 4. Spatial distribution of stations for 4 clusters.

Table 5. Statistical summary of precipitations for 4 clusters distribution (mm)

Cluster	Min.	Max.	Mean	Std. Dev.
A	423.41	846.55	581.23	146.91
B	981.62	1308.07	1130.92	103.93
C	2105.38	2105.38	2105.38	-
D	2284.35	2329.73	2307.04	32.09

The clusters formed for cluster number 5 are shown in *Fig. 5*. Upon analysis of the results, it is observed that clusters A, C, and E are separated as three sub-clusters of cluster A in the previous distribution. Additionally, Rize, Pazar, and Hopa stations maintain integrity again and form cluster D. Thus, cluster A consists of 9 stations located in the inland areas of the Western, Central, and Eastern Black Sea regions. Cluster B consists of 9 stations located in the coastal areas of the Western, Central, and Eastern Black Sea regions. Cluster C consists of 7 stations located in the Western, Central, and Eastern Black Sea regions. Cluster D consists of 3 stations located in the Eastern Black Sea coastal area. Cluster E consists of 3 stations located in the inland areas of the Western and Eastern Black Sea regions. The maximum, minimum, mean, and standard deviation values of annual total precipitation for the identified clusters are presented in *Table 6*.

Fig. 5. Spatial distribution of stations for 5 clusters.

Table 6. Statistical summary of precipitations for 5 clusters distribution (mm)

Cluster	Min.	Max.	Mean	Std. Dev.
A	423.41	476.32	453.90	16.89
B	981.62	1308.07	1130.92	103.93
C	716.47	846.55	757.99	53.98
D	2105.38	2329.73	2239.82	118.62
E	521.17	568.64	550.78	25.82

Clusters were identified using the k-means algorithm for each cluster number starting from 2 up to 5, which was determined as the maximum number of clusters. Silhouette index analysis was used to assess the accuracy of the clusters and to determine the optimum number of clusters. First, silhouette index values of the results obtained for each cluster number were calculated. Then, the average silhouette index values and the number of negative silhouette index values of each cluster were determined. The optimum number of clusters was determined based on the lowest negative silhouette index value in silhouette analysis (*Sonmez* and *Komuscu*, 2008).

Silhouette index values of the stations in the clusters determined from 2 clusters to 5 clusters with k-means are presented in *Fig. 6* and *Table 7*, while the average index value and the number of negative silhouette index values of the clusters are presented in *Table 7*.

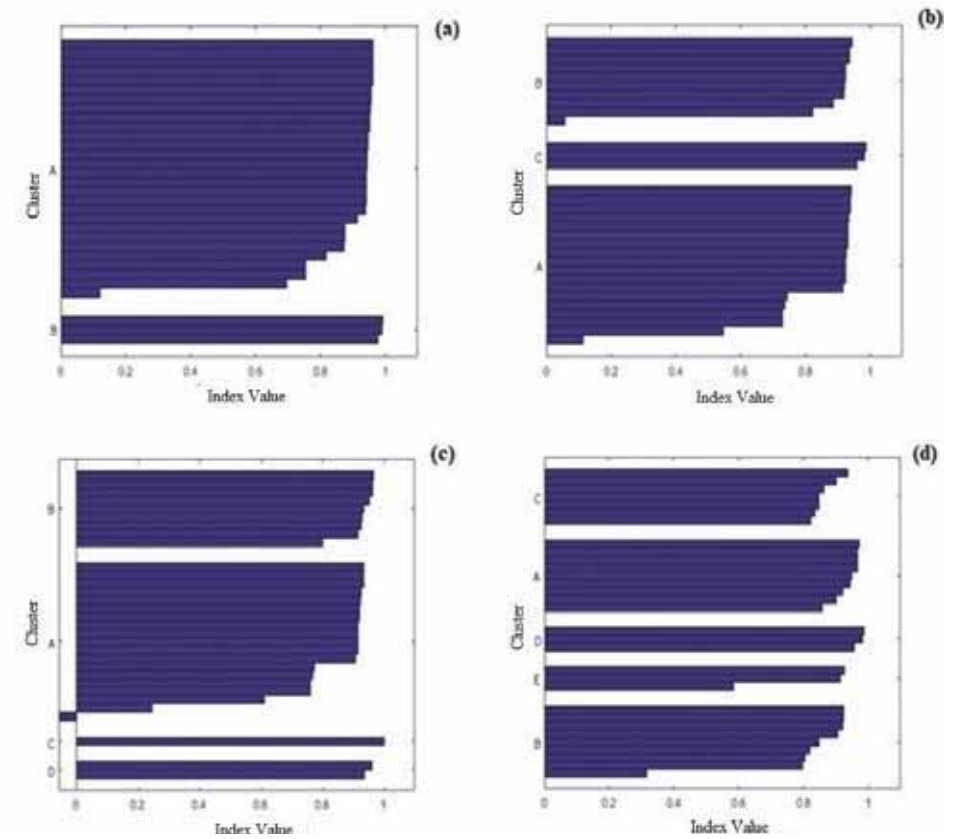

Fig. 6. Silhouette index values of the stations in the clusters.

Table 7. Silhouette index values of the stations in the clusters

Station	No of Clusters			
	2	**3**	**4**	**5**
Düzce	0.956^{A}	0.113^{A}	0.245^{A}	0.900^{C}
Akçakoca	0.817^{A}	0.945^{B}	0.966^{B}	0.922^{B}
Bolu	0.956^{A}	0.940^{A}	0.934^{A}	0.928^{E}
Zonguldak	0.697^{A}	0.923^{B}	0.952^{B}	0.905^{B}
Bartın	0.877^{A}	0.918^{B}	0.926^{B}	0.797^{B}
Amasra	0.913^{A}	0.821^{B}	0.802^{B}	0.317^{E}
Kastamonu	0.951^{A}	0.942^{A}	0.933^{A}	0.585^{A}
İnebolu	0.875^{A}	0.920^{A}	0.928^{B}	0.806^{B}
Bozkurt	0.754^{A}	0.937^{A}	0.963^{B}	0.924^{B}
Tosya	0.946^{A}	0.934^{A}	0.924^{A}	0.858^{A}
Çorum	0.943^{A}	0.926^{A}	0.916^{A}	0.972^{A}
Osmancık	0.939^{A}	0.916^{A}	0.906^{A}	0.920^{A}
Sinop	0.962^{A}	0.737^{A}	0.769^{A}	0.834^{C}
Amasya	0.945^{A}	0.931^{A}	0.921^{A}	0.944^{A}
Merzifon	0.942^{A}	0.924^{A}	0.914^{A}	0.967^{A}
Samsun	0.962^{A}	0.744^{A}	0.775^{A}	0.823^{A}
Bafra	0.961^{A}	0.546^{A}	0.610^{A}	0.935^{C}
Tokat	0.942^{A}	0.924^{A}	0.914^{A}	0.967^{C}
Zile	0.942^{A}	0.924^{A}	0.914^{A}	0.968^{A}
Ordu	0.872^{A}	0.923^{B}	0.933^{B}	0.820^{B}
Ünye	0.754^{A}	0.937^{B}	0.963^{B}	0.924^{B}
Giresun	0.108^{A}	0.886^{B}	0.916^{B}	0.849^{B}
Şebinkarahisar	0.956^{A}	0.939^{A}	0.933^{A}	0.915^{E}
Gümüşhane	0.946^{A}	0.932^{A}	0.923^{A}	0.901^{A}
Trabzon	0.952^{A}	0.057^{B}	-0.057^{A}	0.863^{C}
Akçaabat	0.962^{A}	0.728^{A}	0.761^{A}	0.848^{C}
Bayburt	0.945^{A}	0.930^{A}	0.921^{A}	0.948^{A}
Rize	0.993^{B}	0.988^{C}	0.936^{D}	0.987^{D}
Pazar	0.978^{B}	0.960^{C}	1.000^{C}	0.957^{D}
Artvin	0.962^{A}	0.728^{A}	0.761^{A}	0.849^{C}
Hopa	0.990^{B}	0.983^{C}	0.959^{D}	0.982^{D}
Average silhouette index value	**0.893**	0.837	0.844	0.875
Number of negative silhouette index value	-	-	1	-

According to the results of the silhouette index analysis method presented in *Fig. 6* and *Table 7*, the average silhouette index values of the stations were calculated as 0.893, 0.837, 0.844, and 0.875, respectively, when the number of clusters was selected as 2, 3, 4, and 5. If the number of clusters is 3, the negative silhouette index value belongs to Trabzon with -0.057. Among the clusters formed using the precipitation values of the stations in the Black Sea Region, the most appropriate number of clusters is proposed as a 2-cluster distribution, where the average silhouette index value is maximum at 0.893 and there are no negative silhouette index values. Although not supported by the results of the silhouette index analysis, choosing 3 clusters may offer a good alternative to the 2-cluster approach in terms of geographical integrity and precipitation values.

4. Discussion and conclusion

This study identified clusters with similar annual precipitation characteristics among stations in the Black Sea Region using the k-means algorithm. Clustering analysis was performed for 4 different numbers of clusters ranging from 2 to 5, and the optimal number of clusters was determined using the Silhouette index analysis method. As a result of the analysis, according to the k-means and silhouette index analysis methods, the stations in the Black Sea Region were determined to form 2 clusters with similar precipitation characteristics. A 4-cluster approach with stations having negative silhouette index values is not recommended. Based on silhouette index analysis among the clusters determined by FCM with the same dataset, the authors propose a 4-cluster approach. Alternatively, according to the results of the silhouette index analysis, the 2-cluster, 5-cluster, and 3-cluster approaches can be preferred, respectively (*Kir et al.*, 2023c). In *Kir et al.* (2023c), where clusters are formed with FCM, as an alternative to the 2-cluster approach, the 5-cluster and 3-cluster approaches can be preferred based on the silhouette index analysis. The main difference between the results of this study and *Kir et al.* (2023c) using the same data is thought to be due to the algorithms used in clustering analysis.

When comparing the results of this study with the main studies in the literature covering the Black Sea Region (*Turkes*, 1996; *Unal et al.*, 2003; *Iyigun et al.*, 2013; *Zeybekoglu* and *Ulke Keskin*, 2020; *Ozturk et al*., 2017), it is thought that the main reasons for the identification of different clusters are due to the following factors:

- the methods used in cluster analysis,
- hydrometeorological parameters used and observation periods, and
- regional geographical features of the study area such as mountainous terrain, ruggedness, and the parallelism of the mountains to the coast, as well as the sea effect.

As a follow-up to this study:

- It is recommended to incorporate monthly and seasonal precipitation regimes in clustering analyses using precipitation values and to compare the results with the clusters determined by annual precipitation values.
- In addition to precipitation observations, it is proposed to determine climate classes with various combinations not included in the literature by incorporating hydrometeorological parameters such as temperature, wind speed, current, humidity, evaporation, and geographical location information.
- It is recommended to conduct clustering studies that include hierarchical methods such as Ward's method as well as non-hierarchical methods such as fuzzy c-Means.

- It is recommended that cluster analysis should also be conducted for other regions in the geography of Türkiye.

Data availability: The meteorological data used in this manuscript were obtained from the Turkish State Meteorological Service (TSMS) for the master's thesis titled "Evaluation of the meteorological data of the Black Sea Region using clustering analysis methods" written by Gurkan Kir under the supervision of Asli Ulke Keskin.

Author contributions: AUK: Data curation, investigation, methodology, supervision, and writing (original draft, review and editing). GK: Data curation, investigation, methodology, formal analysis, visualization, and writing (original draft, review, and editing). UZ: Investigation, methodology, formal analysis, validation, visualization, supervision, and writing (original draft, review, and editing).

Competing interests: The authors declare that none of the authors has any competing interests.

Acknowledgments: The authors thank the Turkish State Meteorological Service for providing the meteorological data. The authors also thank the reviewers for their constructive criticisms which have considerably improved this manuscript.

References

Demircan, M., Arabacı, H., Coşkun, M., Türkoğlu, N., and *Çiçek, İ.*, 2017: İklim değişikliği ve halk takvimi: Maksimum sıcaklık desenleri ve değişimi. IV. Türkiye İklim Değişikliği Kongresi, İstanbul Medipol Üniversitesi, İstanbul. (In Turkish)

Dikbas, F., Firat, M., Koc, A.C., and *Gungor, M.*, 2012: Classication of precipitation series using fuzzy cluster method. Int. J. Climatol. 32(10), 1596–1603. https://doi.org/10.1002/joc.2350

Erinc, S., 1949: The climates of Turkey according to Thornthwaite's classifications. *Ann. Assoc. Am. Geograp. 39*, 26–46. https://doi.org/10.2307/2561098

Fırat, M., Dikbaş, F., Koç, A.C., and *Güngör, M.*, 2012: Classification of annual precipitations and identification of homogeneous regions using k-means Method. *Tech. J. 23*(113), 6037–6050.

Günay Atbaş, A.C., 2008: A study on determining the number of clusters in cluster analysis. MSc Thesis, Ankara University, Ankara, Turkey.

Iyigün, C., Türkeş, M., Batmaz, İ., Yozgatlıgil, C., Purutçuoğlu, V., Kartal Koç, E., and *Öztürk, M.Z.*, 2013: Clustering current climate regions of Turkey by using a multivariate statistical method. *Theor Appl Climatol. 114*, 95–106. https://doi.org/10.1007/s00704-012-0823-7

Karahan, H., 2011: Determination of Rainfall Intensity-Duration-Frequency Relationships Using Differential Evolution Algorithm. 108Y299, Research Project, The Scientific and Technological Research Council of Turkey (TUBITAK), Final Report, Ankara, Türkiye.

Karahan H., 2019: Determination of Homogeneous Sub-Regions by Using Intensity-Duration-Frequency Relationships and Cluster Analysis: An Application for the Aegean Region. Pamukkale University J. *Eng. Sci. 25*(8), 998–1013. https://doi.org/10.5505/pajes.2019.09365

Karahan, H., 2012: Determining rainfall-intensity-duration-frequency relationship using Particle Swarm Optimization. *KSCE J. Civil Engin. 16*, 667–675. https://doi.org/10.1007/s12205-012-1076-9

Karahan, H., 2022: Kentsel taşkınların kentleşme ve altyapı bağlamında değerlendirilmesi. TMMOB Afet Sempozyumu, Atmosfer ve İklim Kaynaklı Afetler Oturumu, Çağrılı Konuşmacı, 20-22 Nisan 2022. (In Turkish)

Karahan, H., Ayvaz, M.T., and *Gurarslan, G.*, 2008: Determination of intensity-duration-frequency relationship by genetic algorithm: Case study of GAP. Teknik Dergi/*Technical Journal of Turkish Chamber of Civil Engineers 19*(92), 4393–4407.

Karahan, H., Bahar, E., and *Zeybekoglu, U.*, 2015: Standart süreli maksimum yağış şiddetleri için trend analizi: Doğu Karadeniz Bölgesi için bir uygulama. 7. Kentsel Altyapı Sempozyumu, Bildiriler Kitabı, 227-238, Kasım 2015, Trabzon.

Kir, G., 2021: Evaluation of the meteorological data of the Black Sea Regıon using clustering analysis methods. MSc Thesis, Ondokuz May University, Samsun, Turkey.

Kir, G., Ulke Keskin, A., and *Zeybekoglu, U.*, 2023a: Clustering of Black Sea Region Stations Using K-Means, Fuzzy CMeans and Silhouette Index Analysis Methods. *Resilience 7*(2), 325–337. https://doi.org/10.32569/resilience.1336940

Kir, G., Ulke Keskin, A., and *Zeybekoglu, U.*, 2023b: Clustering of Black Sea Region Meteorology Observation Stations Using Wind Speed Values. *Ordu University Journal of Science and Technology 13*(1), 44–58. https://doi.org/10.54370/ordubtd.1275677

Kir, G., Ulke Keskin, A., and *Zeybekoglu, U.*, 2023c: Clustering of Precipitation in the Black Sea Region with by Fuzzy C-Means and Silhouette Index Analysis. *Black Sea Journal of Engineering and Science 6*(3), 210–218. https://doi.org/10.34248/bsengineering.1296734

Kite, G., 1991: Looking for Evidence of Climatic Change in Hydrometeorological Time Series. Western Snow Conference. Washington, Alaska.

Kulkarni, A. and *Kripalani, R.*, 1998: Rainfall patterns over India: Classification with fuzzy c-means method. *Theor. Appl. Climatol. 59*, 137–146. https://doi.org/10.1007/s007040050019

Ozkoca, T., 2015: Trend analysis of hydrometeorological parameters at middle blacksea region coast band. MSc Thesis, Ondokuz May University, Samsun, Turkey.

Ozturk, M.Z., Cetinkaya, G., and *Aydın, S.*, 2017: Climate Types of Turkey According to Köppen-Geiger Climate Classification. *J. Geography 35*, 17–27. https://doi.org/10.26650/JGEOG295515

Pal, N.R. and *Bezdek, J.C.*, 1995: On Cluster validity for the fuzzy c-means model. *IEEE Transactions On Fuzzy Systems 3*, 370–379. https://doi.org/10.1109/91.413225

Rau, P., Bourrel, L., Labat, D., Melo, P., Dewitte, B, Frappart, F., Lavado, W., and *Felipe, O.*, 2017: Regionalization of rainfall over the Peruvian Pacific slope and coast. Int. J. Climatol. 37, 143–158. https://doi.org/10.1002/joc.4693

Rousseuw, P.J., 1987: Silhouettes: A graphical aid to the interpretation and validation of cluster analysis. *J. Comput. Appl. Math. 20*, 53–65. https://doi.org/10.1016/0377-0427(87)90125-7

Soltani, S. and *Modarres, R.*, 2006: Classification of spatio temporal pattern of rainfall in Iran using a hierarchical and divisive cluster analysis. *J. Spat. Hydrol. 6*(2), 1–12.

Sonmez, I. and *Komuscu, A.*, 2008: Redefinition rainfall regions using k-means clustering methodology and changes of sub period. *Iklim Değişikliği ve Çevre 1*, 38–49.

Sahin, S., 2009: Applying artificial neural networks on determining climate zones and comparison with the Ward?s method. PhD Thesis, Istanbul Technical University, Istanbul, Turkey.

Sahin, S. and *Cigizoğlu, H.K.*, 2012: The sub-climate regions and the sub-precipitation regime regions in Turkey. *J. Hydrol. 450–451*, 180–189. https://doi.org/10.1016/j.jhydrol.2012.04.062

Turkes, M., 1996: Spatial and temporal analysis of annual rainfall variations in Turkey. *Int. J. Climatol. 16*(9), 1057–1076. https://doi.org/10.1002/(SICI)1097-0088(199609)16:9%3C1057::AID-JOC75%3E3.0.CO;2-D

Turkes, M., 2010: Küresel iklim değişikliği: Başlıca Nedenleri, gözlenen ve öngörülen değişiklikler ve etkileri. Uluslararası Katılımlı 1. Meteoroloji Sempozyumu, Devlet Meteoroloji İşleri Genel Müdürlüğü, Ankara. (In Turkish)

Unal, Y., Kındap, T., and *Karaca. M.*, 2003: Redefining the climate zones of Turkey using cluster analysis. *Int. J. Climatol. 23*, 1045–1055. http://dx.doi.org/10.1002/joc.910

Vani, H.Y., Anusuya, M.A., and *Chayadevi, M.L.*, 2019: Fuzzy Clusterıng Algorıthms-Comparatıve Studıes For Noısy Speech Sıgnals. Ictact *J. Soft Comput. 9*(3), 1920–1926. https://doi.org/10.21917/ijsc.2019.0267

Xin, G.L., Min, F.Y., and *Wen, T.H.*, 2011: Speech Recognition based on K-Means Clustering and Neural Network Ensembles. Proceedings of 7th International Conference on Natural Computation.

Zeybekoglu, U. and *Karahan, H.*, 2018: Investigation of Rainfall Intensity Series of Standart Duration with Trend Analysis Methods. Pamukkale *Univ. J. Engin. Sci. 24*(6), 974–1004. https://doi.org/10.5505/pajes.2017.54265

Zeybekoglu, U. and *Ulke Keskin, A.*, 2020: Defining rainfall intensity clusters in Turkey by using the fuzzy c-means algorithm. *Geofizika 37*(2), 181–195. https://doi.org/10.15233/gfz.2020.37.8

Zhang, Y., Wang, W., Zhang, X., and *Li, Y.*, 2008: A cluster validity index for fuzzy clustering. Information Sciences 178, 1205–1218. https://doi.org/10.1016/j.ins.2007.10.004

DOI:10.28974/idojaras.2025.3.6

IDŐJÁRÁS

Quarterly Journal of the HungaroMet Hungarian Meteorological Service
Vol. 129, No. 3, July – September, 2025, pp. 357–372

Evaluation of drought in Bosnia and Herzegovina during the period 1956–2022

Dragan Papić

University of Banja Luka
Faculty of Natural Sciences and Mathematics
Department of Geography
78000 Banja Luka, the Republic of Srpska,
Bosnia and Herzegovina

Author's e-mail: dragan.papic@pmf.unibl.org

(Manuscript received in final form July 23, 2024)

Abstract— The issue of drought is treated as an important natural phenomenon that often has a negative impact on both the livelihoods of the population and environmental protection. Many parts of the world have been affected by catastrophic droughts in the past, leading to prolonged periods of famine and disease among local populations. According to the definition provided by the Intergovernmental Panel on Climate Change in 2014 (IPCC), drought can be assessed as a potential hazard and challenge depending on the evaluation of its impact on the population and its economic activities. The aim of this study is to determine drought periods in Bosnia and Herzegovina and to highlight their consequences. For the purpose of analysis, available data on average monthly precipitation from 12 meteorological stations in Bosnia and Herzegovina from 1956 to 2022 were used. The Standardized Precipitation Index (SPI-1 and SPI-3) was used to determine meteorological drought, including its intensity, frequency, and duration. Based on the results obtained, a relatively uniform frequency of drought was observed across the seasons. On the other hand, extreme droughts were most pronounced in winter and spring months. The maximum duration of drought was recorded in Zenica from November 1989 to October 1990.

Key-words: drought, precipitation, Standardized Precipitation Index, climate change, Bosnia and Herzegovina

1. Introduction

In recent decades, there has been an increase in the occurrence of extreme weather events in many countries worldwide, such as cold and heat waves, floods, fires, droughts, and others. Drought is one of the natural phenomena that has had pronounced negative effects on human society as a whole (*Heim*, 2002; *Zhou* and *Xu*, 2024). It is one of the most destructive natural phenomena globally, considering its long duration, wide-ranging impact, and high frequency (*Mishra* and *Singh*, 2010; *Vogt et al*., 2011; *Vicente-Serrano et al*., 2013; *Lai et al*., 2019; *Wang et al*., 2024). It negatively affects agricultural yields, contributes to soil degradation, leads to the extinction of plant and animal species, while in some parts of the world it is a direct cause of famine and disease (*Mouillot et al*., 2002; *Mishra* and *Singh*, 2010).

Historical data on precipitation and drought indices suggest increased aridity since 1950 in many terrestrial regions on Earth (*Dai*, 2011. 2013). Drought, as a periodic phenomenon, is most commonly caused by natural factors such as lack or insufficient amount of precipitation, low air humidity, and high air temperatures (*Djabeu*, 2017; *Eslamain* and *Eslamain*, 2017), exacerbated by anthropogenic factors such as excessive water consumption, land use, and land management practices (*Wilhite et al*., 2000). Meteorological drought is a monthly or yearly period with precipitation below normal values, often accompanied by above-average temperatures. It precedes and also triggers other types of drought, such as hydrological and agricultural droughts (*Heim*, 2002; *Dai*, 2011).

McMahon and *Diaz Arenas* (1982) define drought as a prolonged period of abnormally dry weather caused by a lack of precipitation that results in serious hydrological imbalance. According to *Anđelković* and *Živković* (2007), drought periods are considered unfavorable phenomena when they last longer than one month.

Dry areas cover 41% of the world's land surfaces (*White* and *Nackoney*, 2003; *Huang et al*., 2015; 2017), and they are home to approximately 2.5 million people (*Mortimore*, 2009). These areas are extremely sensitive to degradation caused by global warming and anthropogenic activities due to the low fertility of dry soils (*Scheffer et al*., 2001; *Rietkerk et al*., 2004; *Maestre et al*., 2013; *Huang et al*., 2015; *Li et al*., 2016; *Zhou et al*., 2016). Studies on drylands worldwide have been the focus of many international scientific research projects such as the Global Land Project (GLP), Integrated Land-Ecosystem-Atmosphere Processes Study (iLEAPS), and Global Water System Project (GWSP) (*Fu* and *De Vries*, 2006).

Many authors have pointed out the increased frequency of drought periods caused by decreased precipitation and increased air temperatures in Southeast Europe (*Anagnostopoulou et al*., 2003; *Tsakiris* and *Vangelis*, 2005; *Anđelković* and *Živković*, 2007; *Koleva* and *Aleksandrov*, 2008; *Reiser* and *Kutiel*, 2008; *Kalamaras et al*., 2010; *Stricevic et al*., 2011; *Gočić* and *Trajković*, 2013; 2014;

Tošić and *Unkašević*, 2013; *Popova et al.*, 2015; *Trnka et al*., 2016; *Spinoni et al*., 2017; *Janačova et al*., 2018; *Jingtao*, 2019; *Hološ* and *Šurda*, 2021; *Stoyanova* and *Nikolova*, 2022). However, there is a lack of studies specifically addressing the issue of drought in Bosnia and Herzegovina, although there are quantitative and qualitative climatological studies dealing with changes in air temperatures and precipitation (*Trbić et al.*, 2017; *Popov et al.*, 2018; 2019; *Papić et al*., 2020; *Gnjato et al*., 2021, *Bačević et al*., 2022), which can serve as a basis for more concrete research on drought periods.

This paper consists of the following subsequent sections: 1) introductory section; 2) overview of the study area; 3) methodology and data sources; 4) findings and discussion; and 5) concluding remarks.

2. Study area

Bosnia and Herzegovina is located in Southeast Europe and shares borders with Croatia, Serbia, and Montenegro (*Fig. 1*). It is situated between 45°16'08" N, 17°13'11" E in the north (municipality of Kozarska Dubica) and 42°33'00" N, 18°32'24" E in the south (city of Trebinje), as well as 44°03'00" N, 19°37'41" E in the east (municipality of Bratunac) and 44°49'30" N, 15°44'00" E in the west (city of Bihać). In the southern part, through a narrow corridor of 21.2 km, it has an outlet to the Adriatic Sea (municipality of Neum).

Table 1. Meteorological stations in Bosnia and Herzegovina

Station No.	Station location	Altitude	Latitude	Longitude
1	Banja Luka	153 m	44°47′08″ N	17°13′11″ E
2	Bileća	443 m	42°53′04″ N	18°27′29″ E
3	Bugojno	562 m	44°03′43″ N	17°27′02″ E
4	Doboj	146 m	44°44′17″ N	18°06′16″ E
5	Ivan Sedlo	967 m	43°45′04″ N	18°02′10″ E
6	Livno	724 m	43°49′22″ N	17°00′04″ E
7	Mostar	99 m	43°20′53″ N	17°47′38″ E
8	Sanski Most	158 m	44°46′12″ N	16°40′25″ E
9	Sarajevo	630 m	43°52′04″ N	18°25′22″ E
10	Sokolac	872 m	43°57′14″ N	18°49′26″ E
11	Tuzla	305 m	44°32′31″ N	18°41′06″ E
12	Zenica	344 m	44°12′07″ N	17°54′01″ E

Fig. 1. Geographical position of Bosnia and Herzegovina with landmarks of the analyzed meteorological stations.

The climate of Bosnia and Herzegovina is diverse, influenced by various climatic factors. The Adriatic Sea significantly affects the climate, particularly during the colder periods of the year, by releasing a large amount of heat, thus tempering extreme winter temperatures. The relief, altitude, distribution of mountain ranges, plateaus, basins, and karst fields significantly modify the climate of Bosnia and Herzegovina. The Dinaric Mountains, in particular, exert a pronounced climatic influence as they act as a natural barrier, preventing the penetration of cold air masses from the north and warm air masses from the south. Through karst basins and valleys of major rivers, continental influences from the north and Mediterranean influences from the south penetrate deeper into the interior. Soil composition, vegetation, and snow cover also influence the character of climatic elements, thereby modifying the climate of specific locations. Cyclonic activity and numerous local influences also contribute to the climate (*Marković*, 1972; *Rodić*, 1975; *Drešković* and *Mirić*, 2014; *Bajić* and *Trbić*, 2016).

On the territory of Bosnia and Herzegovina, three main types of climate are prevalent: continental and moderately continental, mountainous and

mountainous-valley, and Mediterranean and modified Mediterranean climates. Continental climate is found in the northern part of the country, Mediterranean in the south, and the area between these two climate regions is characterized by high mountains, plateaus, and valleys, where, depending on the altitude, mountainous climate predominates.

3. Data and methods

3.1. Data

The study determined drought periods in the research area from 1956 to 2022. Precipitation data from 12 meteorological stations (MS) were utilized, which were published in the Statistical Yearbooks of the Statistical Office of the Republic of Srpska and the Federal Hydrometeorological Institute of Bosnia and Herzegovina. Most meteorological stations lack data, primarily from the period of the civil war (1991–1995). An exception is the meteorological station in Mostar, where continuous measurements are available throughout the analyzed period. The percentage of missing data for other stations is as follows: MS Sarajevo 1.5%, MS Sanski Most 1.7%, MS Tuzla 3.1%, MS Zenica 3.7%, MS Bugojno 4.6%, MS Banja Luka, MS Bileća, and MS Livno 5.9%, MS Sokolac and MS Doboj 7.4%, and MS Ivan Sedlo 8.3%. Accordingly, missing data were supplemented using interpolation methods due to justified reasons (*Kasam et al*., 2014; *Kilibarda et al*., 2015).

From *Table 1*, which displays the mathematical-geographical coordinates of meteorological stations and their relative altitudes, it is evident that the selected meteorological stations are situated at varying elevations. The lowest relative altitude is found at the MS Mostar (99 m), while the highest is at Ivan Sedlo (967 m), indicating a diversity in climate conditions.

3.2. Methods

To determine meteorological drought in the study, the Standardized Precipitation Index (SPI) (*McKee et al.,* 1993) was utilized. It was calculated using data on average monthly precipitation for the period 1956–2022. SPI values were obtained using RStudio (Version R4.3.3). The World Meteorological Organization (WMO) recommends this index as a universal drought analysis tool, and it is frequently used in scientific studies (*Kim et al.,* 2009; *Mendez* and *Magana*, 2010; Hayes et al., 2011; Stricevic et al., 2011; Spinoni et al., 2014; Labudova et al., 2016; *Šudra et al*., 2020; *Hološ* and *Šurda*, 2021; *Stoyanova* and *Nikolova*, 2022; *Amiri* and *Gocic*, 2023; *Erkol et al*., 2024; *Zhou* and *Hu*, 2024). Generally, indices based on precipitation data are more widely accepted by the scientific community, as precipitation is the main factor contributing to the occurrence, development, and duration of droughts (*Mahmoudi et al*., 2019).

Using SPI as an indicator, a functional and quantitative definition of drought can be established for each time period. In addition to its applicability to various time series, it can provide early drought warning and assist in assessing drought intensity. SPI values correspond to standardized sets of precipitation values transformed into a gamma distribution. The occurrence of drought for a given time period is defined as a period in which SPI is continuously negative and when SPI reaches a value of -1.0 or less. According to *McKee et al*. (1993), drought intensity is arbitrarily defined for SPI values in the following categories:

Table 2. Classification of droughts according to SPI values

SPI values	Drought category
0 to -0.99	mild drought
-1.00 to -1.49	moderate drought
-1.5 to -1.99	severe drought
≤ -2.00	extreme drought

Source: *McKee et al.,* 1993

Using the provided categorization, we determined a drought period as when SPI ≤ -1, while extreme drought occurs when SPI ≤ -2. For determining meteorological drought, we utilized short-term SPI values for 1 and 3 months (SPI-1 and SPI-3), as opposed to agricultural and hydrological droughts, which typically employ SPI-6 and SPI-12 values (Svodoba et al., 2012; *Stoyanova* and *Nikolova*, 2022; *Wang et al.*, 2022).

We utilized SPI-1 values to determine the duration, magnitude, and intensity of drought. The onset of drought is defined as the period when the SPI-1 value is less than or equal to -1.0, while the drought ends when SPI-1 reaches 0 or a positive value. According to *McKee et al.* (1993), the drought magnitude (DM) represents the sum of all mentioned months (from -1 to 0) and is calculated using the formula:

$$DM \equiv -\left(\sum_{j-1}^{x} \mathrm{SPI}_{ij}\right),$$

where *j* represents the first month in which SPI-1 is less than or equal to -1.0, and *x* is the last consecutive month with a negative SPI-1 value. Based on the obtained drought magnitude values, the average drought intensity (ADI) can be calculated, representing the ratio between the magnitude (DM) and the duration of drought (D) (*McKee et al*., 1995; *Bonaccorso et al.*, 2003; *Stoyanova* and *Nikolova*, 2022). It is calculated using the formula:

$$ADI \equiv \frac{DM}{D}.$$

SPI-3 values were used to determine seasonal droughts. Accordingly, SPI-3 values were extracted for each season. Spring was calculated using total precipitation for March, April, and May; summer for June, July, and August; autumn for September, October, and November; and finally, winter for the months of December, January, and February.

4. Results and discussion

4.1. Duration, magnitude, and average drought intensity based on SPI-1 values

Drought as a phenomenon significantly impacts various economic sectors, with agriculture often being the first to suffer due to its dependence on soil moisture content, which can decrease rapidly during a drought period. If the duration of precipitation deficit extends, then other sectors reliant on available water resources will also be affected (*Table 3*).

Table 3. Duration, magnitude, and average drought intensity in Bosnia and Herzegovina from 1956 to 2022

Meteorological stations (MS)	Start month	End month	D	Lowest value of SPI-1	DM	ADI
Banja Luka	October 2019	April 2020	7	-4.93	6.33	-0.90
Bileća	January 2000	June 2000	6	-5.43	6.82	-1.13
Bugojno	November 1989	September 1990	11	-4.60	11.13	-1.01
Doboj	March 2011	November 2011	9	-4.55	11.02	-1.22
Ivan Sedlo	June 1990	January 1991	8	-4.83	3.97	-0.49
Livno	May 1962	October 1962	6	-4.11	7.81	-1.30
Mostar	January 1993	May 1993	5	-4.78	9.53	-1.90
Sanski Most	June 1988	March 1989	9	-4.33	8.29	-0.92
Sarajevo	December 1989	August 1990	9	-4.31	8.59	-0.95
Sokolac	September 1956	March 1957	7	-5.44	7.88	-1.12
Tuzla	May 1962	October 1962	6	-4.53	5.85	-0.97
Zenica	November 1989	October 1990	12	-4.31	13.80	-1.15

The duration of drought at the observed stations in Bosnia and Herzegovina varies, which is expected given the different climatic characteristics. The maximum duration of drought in the observed period was 12 months at the meteorological station Zenica from November 1989 to October 1990 (*Table 3*).

The magnitude of this event was 13.80, with an average drought intensity of -1.15. The minimum duration of drought was 5 months, recorded from January to May 1993 at MS Mostar. Although the drought lasted for 5 months, the magnitude of this event was very high at 9.53, resulting in the most pronounced average drought intensity (-1.90).

The occurrence of extreme drought was recorded at most observed stations in the years 1957 (9 stations), 1963 (9 stations), 1969 (8 stations), 1989 (9 stations), 2007 (9 stations), 2012-2013 (all stations), 2017 (10 stations), and 2021–2022 (8 stations). Multi-year periods without drought occurrence at most stations were observed in the years 1958–1960, 1976–1978, 2004–2006, and 2008–2010 (*Fig. 2*).

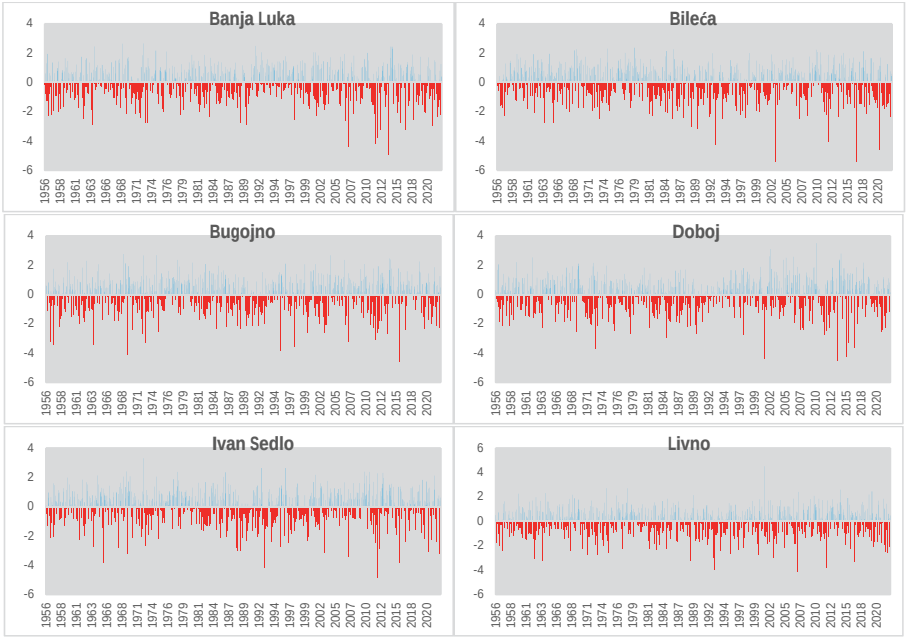

Fig. 2. SPI-1 values at 12 meteorological stations in Bosnia and Herzegovina.

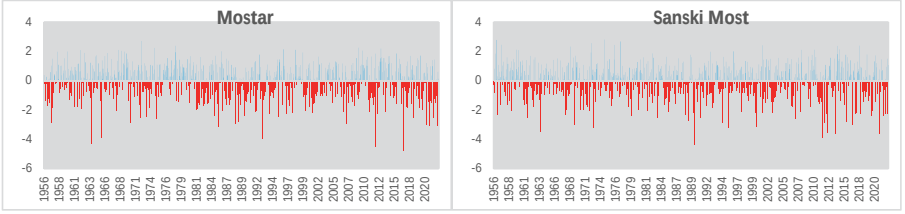

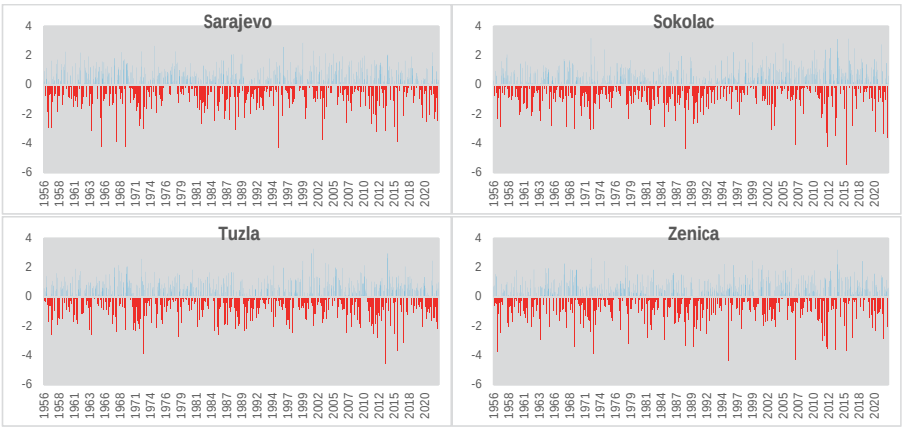

Fig. 2 continued.

4.2. Drought frequency according to SPI-3 values

Analysis of drought results obtained based on SPI-3 values for all 12 observed stations in Bosnia and Herzegovina indicates a relatively uniform frequency of droughts and extreme droughts across the seasons (*Table 4*, *Fig 3*). The frequency of drought was highest in the summer period (13.55%), while it was lowest in the winter period (12.93%). The frequency of extreme drought was most pronounced in winter (2.98%), and least pronounced in autumn (2.07%).

Table 4. Frequency of drought in Bosnia and Herzegovina from 1956 to 2022 by seasons

	Season	Spring		Summer		Autumn		Winter	
MS	**Drought**	**No. of months**	**%**	**No. of months**	**%**	**No. of months**	**%**	**No. of months**	**%**
Banja Luka	Dry	26	12.93	29	14.42	29	14.42	28	13.93
	Extremely dry	6	2.98	3	1.49	4	1.99	5	2.48
Bileća	Dry	26	12.93	27	13.43	24	11.94	23	11.44
	Extremely dry	5	2.48	5	2.48	5	2.48	10	4.97
Bugojno	Dry	30	14.92	21	10.44	30	14.92	22	10.94
	Extremely dry	5	2.48	8	3.98	6	2.98	6	2.98
Doboj	Dry	28	13.93	24	11.94	26	12.93	27	13.43
	Extremely dry	3	1.49	2	0.99	5	2.48	5	2.48
Ivan Sedlo	Dry	29	14.42	27	13.43	25	12.43	25	12.43
	Extremely dry	3	1.49	3	1.49	4	1.99	6	2.98
Livno	Dry	35	17.41	30	14.92	21	10.44	23	11.44
	Extremely dry	2	0.99	3	1.49	1	0.49	8	3.98
Mostar	Dry	28	13.93	30	14.92	25	12.43	28	13.93
	Extremely dry	4	1.99	4	1.99	4	1.99	9	4.47
Sanski Most	Dry	18	8.95	26	12.93	25	12.43	31	15.42
	Extremely dry	10	4.97	5	2.48	4	1.99	5	2.48
Sarajevo	Dry	25	12.43	28	13.93	27	13.43	28	13.93
	Extremely dry	7	3.48	4	1.99	4	1.99	3	1.49
Sokolac	Dry	24	11.94	24	11.94	27	13.43	27	13.43
	Extremely dry	6	2.98	2	0.99	5	2.48	5	2.48
Tuzla	Dry	26	12.93	31	15.42	29	14.42	24	11.94
	Extremely dry	6	2.98	7	3.48	3	1.49	4	1.99
Zenica	Dry	28	13.93	30	14.92	28	13.93	26	12.93
	Extremely dry	7	3.48	8	3.98	5	2.48	6	2.98
Total	Dry	323	13.39	327	13.55	316	13.1	312	12.93
	Extremely dry	64	2.65	51	2.11	50	2.07	72	2.98

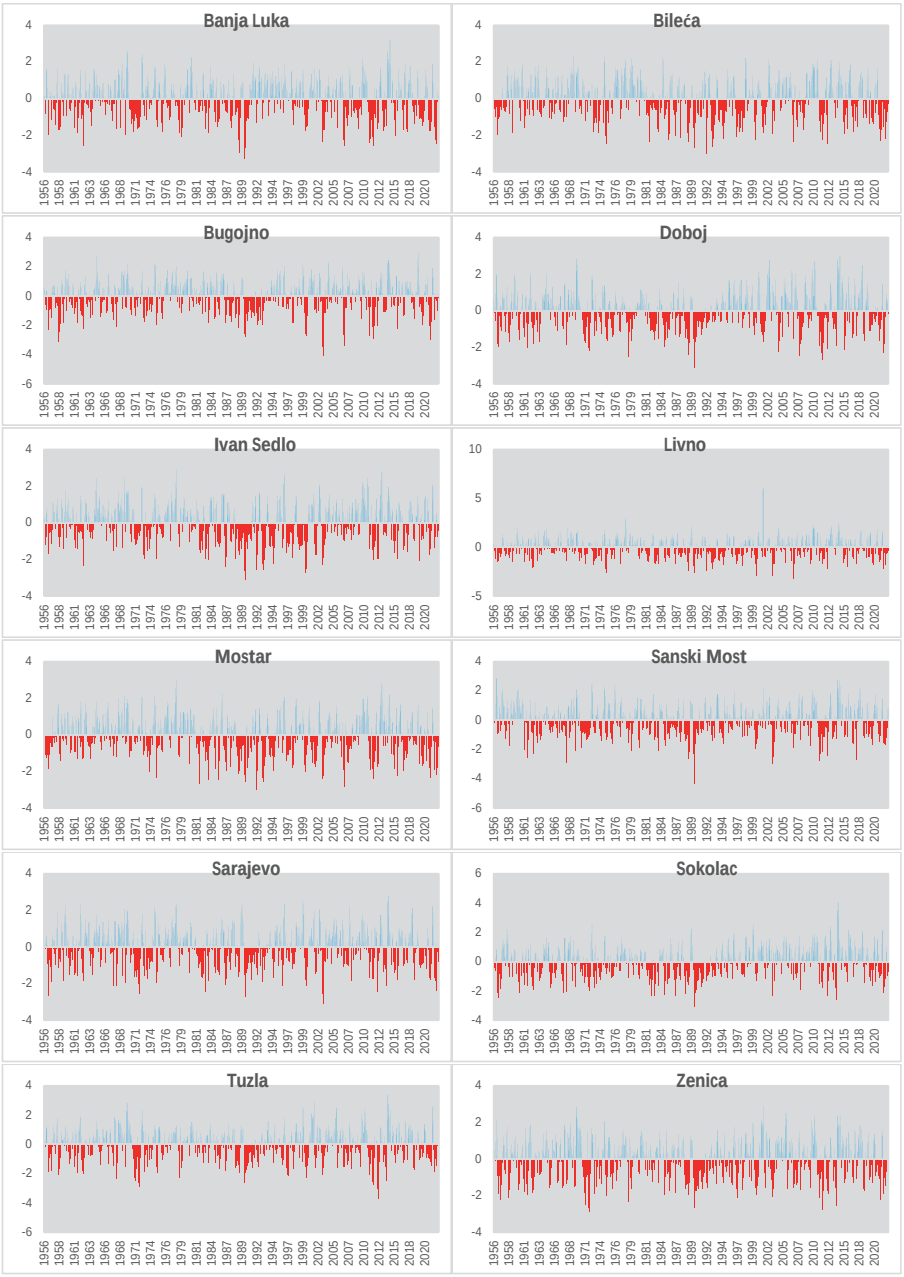

Fig. 3. SPI-3 values at 12 meteorological stations in Bosnia and Herzegovina.

Expectedly, the frequencies of drought vary across seasons when observing individual meteorological stations. The highest number of drought months in spring was recorded in Livno, totaling 35 (17.41%), while the lowest was in Sanski Most with 18 (8.95%). The most pronounced drought in the summer period was observed in Tuzla with 31 drought months (15.42%), while the least pronounced was in Bugojno with 21 drought months (10.44%). The highest number of drought months in autumn was recorded in Bugojno, totaling 30 (14.92%), and the lowest in Livno with 21 (10.44%). Winter saw the most pronounced drought in Sanski Most with 31 drought months (15.42%), while the least pronounced was in Bileća and Livno with 23 drought months each (11.44%).

The most extremely dry spring months were recorded in Sanski Most, totaling 10 (4.97%), summer months in Bugojno and Zenica, totaling 8 (3.98%), autumn months in Bugojno, totaling 6 (2.98%), and winter months in Mostar, totaling 9 (4.47%). In contrast, Livno has the least extremely dry spring months, totaling 2 (0.99%), Sokolac summer months, totaling 2 (0.99%), Livno autumn months 1 (0.49%), and Sarajevo winter months, totaling 3 (1.49%).

5. Conclusion

Meteorological drought occurs when below-average amounts of precipitation are recorded over an extended period, resulting in reduced moisture in the soil and atmosphere. It can significantly impact crop yields, reduce livestock numbers, increase the risk of wildfires, degrade soil, and disrupt ecosystems.

The study analyzed available data on average monthly precipitation from 12 meteorological stations in the territory of Bosnia and Herzegovina from 1956 to 2022. By using the Standardized Precipitation Index (SPI) as an indicator, we identified drought periods and their characteristics. We observed a relatively uniform frequency of droughts across the seasons, with the most pronounced extreme droughts occurring in winter and spring months. The maximum duration of drought was recorded in Zenica from November 1989 to October 1990. The longest periods of extreme drought in most stations were observed in 1957, 1963, 1969, 1989, 2007, 2012–2013, 2017, and 2021-2022.

In conclusion, our research highlights the crucial importance of understanding drought dynamics for efficient water resource management, adapting to climate change, and efforts to reduce disaster risks in Bosnia and Herzegovina. Although drought is a common occurrence in Bosnia and Herzegovina, a drought management strategy has not yet been developed in the country. This study can serve as a basis for future research focusing on assessing the risks and hazards of drought.

References

Amiri, M.A. and *Gocic, M.*, 2023: Analysis of temporal and spatial variations of drought over Serbia by investigating the applicability of precipitation-based drought indices. *Theor. Appl. Climatol. 154*, 261–274. https://doi.org/10.1007/s00704-023-04554-6

Anagnostopoulou, C., Maheras, P., Karacostas, T., and *Vafiadis, M.*, 2003: Spatial and temporal analysis of dry spells in Greece. *Theor. Appl. Climatol. 74*, 77–91. https://doi.org/10.1007/s00704-002-0713-5

Anđelković, G. and *Živković, N.*, 2007: Precipitation as adverse climatic phenomenon in Negotin. *Bull. Serbian Geograph. Soc. 87*(1), 51–62. https://doi.org/10.2298/GSGD0701051A

Bačević, N.R., Milentijević, N., Valjarević, A., Nikolić, M., Stevanović, V., Kićović, D., Radaković, M., Papić, D., and *Marković, S.B.*, 2022: The analysis of annual and seasonal surface air temperature trends of southern and southeastern Bosnia and Herzegovina from 1961 to 2017. *Időjárás 126*, 355–374. https://doi.org/10.28974/idojaras.2022.3.5

Bajić, D. and *Trbić, G.*, 2016: Klimatski atlas Bosne i Hercegovine. Temperature i padavine. (1961-1990, A1B 2001-2030, A1B 2071-2100, A2 2071-2100). Banja Luka: Prirodno-matematički fakultet.

Bonaccorso, B., Bordi, I., Cancelliere, A., Rossi, G., and *Sutera, A.*, 2003: Spatial Variability of Drought: An Analysis of the SPI in Sicily. *Water Res. Manage. 17*(4), 273–296. https://doi.org/10.1023/A:1024716530289

Dai, A., 2011: Drought under global warming: A review. *WIREs Climatic Change 2*, 45–65. https://doi.org/10.1002/wcc.81

Dai, A., 2013: Increasing drought under global warming in observations and models. *Nat. Climate Change 3*, 52–58. https://doi.org/10.1038/nclimate1633

Drešković, N. and *Mirić, R.*, 2014: Klimatska regionalizacija Bosne i Hercegovine, Zbornik radova III kongresa geografa Bosne i Hercegovine, Sarajevo: Geografsko društvo u Federaciji BiH, 280–294. (In Serbian)

Djebou, D.C.S., 2017: Bridging drought and climate aridity. *J. Arid Environ. 144*, 170–180. https://doi.org/10.1016/j.jaridenv.2017.05.002

Erkol, Z.I., Yesilyurt, S.N., and *Dalkilic, H.Y.*, 2024: Impacts of climate change on spatial drought distribution in the Mediterranean Basin (Turkey): different climate models and downscaling methods. *Theor. Appl. Climatol. 155*, 4065–4087. https://doi.org/10.1007/s00704-024-04867-0

Eslamian, E. and *Eslamian, F.A.*, (Eds.). 2017: Handbook of Drought and Water Scarcity: Management of Drought and Water Scarcity. Routledge. https://doi.org/10.1201/9781315226774

Fu, C. and *De Vries, F.P.*, 2006: Initial Science Plan of the Monsoon Asia Integrated Regional Study, MAIRS-IPO, IAP-CAS, Beijing.

Gnjato, S., Popov, T., Ivanišević, M., and *Trbić, G.*, 2021: Changes in extreme climate indices in Sarajevo (Bosnia and Herzegovina). *Bull. Serbian Geograph. Soc. 101*(2), 1−21. https://doi.org/10.2298/GSGD2102001G

Gocic, M. and *Trajkovic, S.*, 2013: Analysis of precipitation and drought data in Serbia over the period 1980–2010. *J. Hydrol. 494*, 32–42. https://doi.org/10.1016/j.jhydrol.2013.04.044

Gocic, M. and *Trajkovic, S.*, 2014: Spatiotemporal characteristics of drought in Serbia. *J. Hydrol. 510*, 110–123. https://doi.org/10.1016/j.jhydrol.2013.12.030

Hayes, M., Svoboda, M., Wall, N., and *Widhalm, M.*, 2011: The Lincoln declaration on drought indices: Universal meteorological drought index recommended. *Bull. Amer. Meteorol. Soc., 92*, 485–488. https://doi.org/10.1175/2010BAMS3103.1

Heim, R.R., 2002: A review of twentieth-century drought indices used in the United States. *Bull. Amer. Meteorol. Soc., 83*, 1149–1165. https://doi.org/10.1175/1520-0477-83.8.1149

Hološ, S. and *Šurda, P.*, 2021: Evaluation of Drought – Review of Drought Indices and their Application in the Recent Studies from Slovakia. *Acta Horticulturae et Regiotecturae 24*, 97–108. https://doi.org/10.2478/ahr-2021-0015

Huang, J., Yu, H., Guan, X., Wang, G., and *Guo, R.*, 2015: Accelerated dryland expansion under climate change. *Nature Climate Change 6*,166–171. https://doi.org/10.1038/nclimate2837

Huang, J., Li, Y., Fu, C., Chen, F., Fu, Q., Dai, A., Shinoda, M., Ma, Z., Guo, W., Li, Z., Zhang, L., Liu, Y., Yu, H., He, Y., Xie, Y., Guan, X., Ji, M., Lin, L., Wang, S., Yan, H., and *Wang, G.*, 2017: Dryland climate change: Recent progress and challenges. *Rev. Geophys. 55*, 719–778. https://doi.org/10.1002/2016RG000550

IPCC, 2014: Climate Change 2014: Synthesis Report. Contribution of Working Groups I, II and III to the Fifth Assessment Report of the Intergovernmental Panel on Climate Change [Core Writing *Team, R.K. Pachauri and L.A. Meyer* (eds.)]. IPCC, Geneva, Switzerland, 151.

Janáčová, T., Labudová, L., and *Labuda, M.*, 2018: Meteorological drought in the parts of Slovakia with lowland features in 1981– 2010. *Geographia Cassoviensis 12*(1), 53–64.

Jiangtao, W., 2019: Spatiotemporal analysis of drought based on meteorological index SPI in North China. *Soil Water Conserv. 26*(4), 203–7.

Kalamaras, N., Michalopoulou, H., and *Byun, H.R.*, 2010: Detection of drought events in Greece using daily precipitation, *Hydrology Res. 41*(2), 126-133. https://doi.org/10.2166/nh.2010.001

Kasam, A.A., Lee, B.D., and *Paredis, C.J.J.*, 2014: Statistical Method for interpolating missing meteorological data for use in building simulation. *Build. Simulat. 7*, 455–465. https://doi.org/10.1007/s12273-014-0174-7

Kilibarda, M., Tadić Perčec, M., Hengl, T., Luković, J. and *Bajat, B.*, 2015: Global geographic and feature space coverage of temperature data in the context of spatio-temporal interpolation. *Spat. Stat. 14(A)*, 22–38. https://doi.org/10.1016/j.spasta.2015.04.005

Kim, D.W., Byun, H.R., and *Choi, K.S.*, 2009: Evaluation, modification, and application of the effective drought index to 200 – year drought climatology of Seoul Korea. *J. Hydrol. 378*(1–2), 1–12. https://doi.org/10.1016/j.jhydrol.2009.08.021

Kim, D.W. and *Byun, H.R.*, 2009: Future pattern of Asian drought under global warming scenario. *Theor. Appl. Climatol. 98*(1–2), 137–150. https://doi.org/10.1007/s00704-008-0100-y

Koleva, E. and *Alexandrov, V.*, 2008: Drought in the Bulgarian low regions during the 20th century. *Theor. Appl. Climatol. 92*, 113–120. https://doi.org/10.1007/s00704-007-0297-1

Labudová, L., Labuda, M., and *Takáč, J.*, 2016: Comparison of SPI and SPEI applicability for drought impact assessment on crop production in the Danubian lowland and the east Slovakian lowland. *Theor. Appl. Climatol. 128*, 491–506. https://doi.org/10.1007/s00704-016-1870-2

Lai, C., Zhong, R., Wang, Z., Wu, X., Chen, X., Wang, P., and *Lian, Y.*, 2019: Monitoring hydrological drought using long-term satellite-based precipitation data. *Sci. Total Environ. 649*, 1198–1208. https://doi.org/10.1016/j.scitotenv.2018.08.245

Li, J., Liu, Z., He, C., Tu, W., and *Sun, Z.*, 2016: Are the drylands in northern China sustainable? A perspective from ecological footprint dynamics from 1990 to 2010, *Sci. Total Environ. 553*, 223–231. https://doi.org/10.1016/j.scitotenv.2016.02.088

Mahmoudi, P., Rigi, A., and *Miri Kamak M.*, 2019: A comparative study of precipitation-based drought indices with the aim of selecting the best index for drought monitoring in Iran. *Theor. Appl. Climatol. 137*, 3123–3138. https://doi.org/10.1007/s00704-019-02778-z

Marković, J.Đ., 1972: Geografske oblasti Socijalističke Federativne Republike Jugoslavije. Beograd: Zavod za udžbenike i nastavna sredstva Srbije. (In Serbian)

McKee, T. B., Doesken, N. J., and *Kleist, J.*, 1993: The Relationship of Drought Frequency and Duration to Time Scales. In *Proceedings of the 8th Conference on Applied Climatology 17*(22), 179–183. https://climate.colostate.edu/pdfs/relationshipofdroughtfrequency.pdf

McKee, T.B., Doesken, N.J., and *Kleist, J.*, 1995: Drought monitoring with Multiple Time scales. *Proceeding of the 9th Conference on Applied Climatology*. Dallas, TX: American Meteorological Society, 233–236.

Méndez, M. and *Magaña, V.*, 2010: Regional Aspects of Prolonged Meteorological Droughts over Mexico and Central America. *J. Climate 23*, 1175–1188. https://doi.org/10.1175/2009JCLI3080.1

Maestre, F.T., Escolar, C., Ladron de Guevara, M., Quero, J.L., Lazaro, R., Delgado-Baquerizo, M., Ochoa, V., Berdugo, M., Gozalo, B., and *Gallardo, A.*, 2013: Changes in biocrust cover drive carbon cycle responses to climate change in drylands, *Glob. Change Biol. 19*(12), 3835–3847. https://doi.org/10.1111/gcb.12306

Mouillot, F., Rambal, S., and *Joffre, R.*, 2002: Simulating climate change impacts on fire frequencyand vegetation dynamics in a Mediterranean-type ecosystem. *Glob. Change Biol. 8*, 423–437.

https://doi.org/10.1046/j.1365-2486.2002.00494.x
Mortimore, M., 2009: Dryland Opportunities, IUCN, Gland, Switzerland, HED, London, UK and UNDP, New York, USA.
Mishra, A.K. and *Singh, V.P.*, 2010: A review of drought concepts. *J. Hydrol. 391*(1–2), 202–216. https://doi.org/10.1016/j.jhydrol.2010.07.012
McMahon, T.A. and *Diaz Arenas, A.*, 1982: Methods of Computation of Low Streamflow, Studies and Reports in Hydrology 36 UNESCO Paris 9S.
Papić, D., Bačević, R. B., Valjarević, A., Milentijević, N., Gavrilov, B. M., Živković, M., and *Marković, B.M.*, 2020: Assessment of air temperature trends in South and Southeast Bosnia and Herzegovina from 1961 to 2017, *Időjárás 124*, 381–399. https://doi.org/10.28974/idojaras.2020.3.5
Popov, T., Gnjato, S., and *Trbić, G.*, 2018: Analysis of Extreme Precipitation over the Peripannonian Region of Bosnia and Hercegovina. *Időjárás 122*, 433–452. https://doi.org/10.28974/idojaras.2018.4.5
Popov, T., Gnjato, S., and *Trbić, G.*, 2019: Changes in Extreme Temperature Indices over the Peripannonian Region of Bosnia and Herzegovina. *Geografie 124*(1), 19–40. https://doi.org/10.37040/geografie2019124010019
Popova, Z., Ivanova, M., Pereira, L., Alexandrov, V., Kercheva, M., Doneva, K., and *Martins, D.*, 2015: Droughts and Climate Change in Bulgaria: Assessing Maize Crop Risk and Irrigation Requirements in Relation to Soil and Climate Region. *Bulgarian J. Agricult. Sci. 21*(1), 35–53. https://www.agrojournal.org/21/01-04.pdf
Reiser, H. and *Kutiel, H.*, 2008: Rainfall uncertainty in the Mediterranean: definition of the rainy season – a methodological approach. *Theor. Appl. Climatol. 94*, 35–49. https://doi.org/10.1007/s00704-007-0343-z
Rietkerk, M., Dekker, S. C., de Ruiter, P. C., and van *de Koppel, J.*, 2004: Self-organized patchiness and catastrophic shifts in ecosystems, *Science 305*(5692), 1926–1929. https://doi.org/10.1126/science.1101867
Rodić, D.P., 1975: *Geografija Jugoslavije*, Naučna Knjiga, Beograd. (In Serbian)
Šurda, P., Vitkova, J., and *Rončak, P.*, 2020: Regional Drought Assessment Based on the Mateorological Indices, *Bull.Georgian Nat. Acad. Sci. 14*, 69–74.
Scheffer, M., Carpenter, S., Foley, J.A., Folke, C., and *Walker, B.*, 2001: Catastrophic shifts in ecosystems, *Nature 413*(6856), 591–596. https://doi.org/10.1038/35098000
Spinoni, J., Naumann, G., Carrao, H., Barbosa, P., and *Vogt, J.*, 2014: World drought frequency, duration, and severity for 1951–2010. *Int. J. Climatol. 34*, 2792–2804. https://doi.org/10.1002/joc.3875
Spinoni, J., Gustavo, N., and *Vogt, J. V.*, 2017: Pan-European seasonal trends and recent changes of drought frequency and severity. *Glob. Planet. Change 148*, 113–130. https://doi.org/10.1016/j.gloplacha.2016.11.013
Stricevic, R., Djurovic, N., and *Djurovic, Z.*, 2011: Drought classification in Northern Serbia based on SPI and statistical pattern recognition. *Meteorol. Appl. 18*(1), 60–69. https://doi.org/10.1002/met.207
Stoyanova, R. and *Nikolova, N.*, 2022: Meteorological drought in southwest Bulgaria during the period 1961–2020, *Journal of Geographical Institute „Jovan Cvijic" 72*(3), 243–255. https://doi.org/10.2298/IJGI2203243S
Svoboda, M., Hayes, M., and *Wood, D.*, 2012: Standardized Precipitation Index: User Guide (WMO-No.1090). World Meteorological Organization.
Tošić, I. and *Unkašević, M.*, 2013: Analysis of wet and dry periods in Serbia. *Int. J. Climatol.* 34, 1357–1368. https://doi.org/10.1002/joc.3757
Tsakiris, G. and *Vangelis, H.*, 2005: Establishing a Drought Index Incorporating Evapo-Transpiration. *Eur. Water J. 9*, 3–11. 10.1146/annurev.environ.33.081307.123117
Trbić, G., Popov, T., and *Gnjato, S.*, 2017: Analysis of Air Temperature Trends in Bosnia and Herzegovina. *Geographica Pannonica 21*(2), 68–84. https://doi.org/10.5937/GeoPan1702068T
Trnka, M., Balek, J., Štěpánek, P., Zahradníček, P., Možný, M., Eitzinger, J. et al., 2016: Drought trends over part of Central Europe between 1961 and 2014. *Climate Res. 70*, 143–160. https://doi.org/10.3354/cr01420

Vicente-Serrano, S.M., Gouveia, C., Camarero, J. J., Beguería, S., Trigo, R., López-Moreno, J. I., Azorín-Molina, C., Pasho, E., Lorenzo-Lacruz, J., Revuelto, J., Morán-Tejeda E. and *Sanchez-Lorenzo, A.*, 2013: The response of vegetation to drought time-scales across global land biomes. *Proceedings of the National Academy of Sciences of the United States of America 110*, 52–57. https://doi.org/10.1073/pnas.1207068110

Vogt, J.V., Barbosa, P., Hofer, B., Magni, D., De Jager, A., Singleton, A., Horion, S., Sepulcre, G., Micale, F., Sokolova, E., Calcagni, L., Marioni, M., and *Antofie, T.E.*, 2011: Developing a European Drought Observatory for Monitoring, Assessing and Forecasting Droughts across the European Continent. In *AGU Fall Meeting Abstracts 1*, NH24A-07.

Wang, Q., Zhang, R., Qi, J., Zeng, J., Wu, J., Shui, W., Wu, X., and *Li, J.*, 2022: An improved daily standardized precipitation index dataset for mainland China from 1961 to 2018. *Sci. Data 9*, 124. https://doi.org/10.1038/s41597-022-01201-z

Wang, W., Du, Q., Yang, H., Jin, P., Wang, F., and *Liang, Q.*, 2024: Drought patterns and multiple teleconnection factors driving forces in China during 1960–2018, *J. Hydrol.* 631, 130821. https://doi.org/10.1016/j.jhydrol.2024.130821

White, R.P. and *Nackoney, J.*, 2003: Drylands, People and Ecosystem Goods and Services, World Resources Institute, Washington.

Zhou, L., Chen, H., Hua, W., Dai, Y., and *Wei, N.*, 2016: Mechanisms for stronger warming over drier ecoregions observed since 1979, *Climate Dynamics* 47(9), 2955–2974. https://doi.org/10.1007/s00382-016-3007-9

Zhou, X., and *Xu, X.*, 2024: The research of common drought indexes for the application to the drought monitoring in the region of Jin Sha river. *Open Geosciences 16*, 1. https://doi.org/10.1515/geo-2022-0489

INSTRUCTIONS TO AUTHORS OF *IDŐJÁRÁS*

The purpose of the journal is to publish papers in any field of meteorology and atmosphere related scientific areas. These may be

- research papers on new results of scientific investigations,
- critical review articles summarizing the current state of art of a certain topic,
- short contributions dealing with a particular question.

Some issues contain "News" and "Book review", therefore, such contributions are also welcome. The papers must be in American English and should be checked by a native speaker if necessary.

Authors are requested to send their manuscripts to

Editor-in Chief of IDŐJÁRÁS
P.O. Box 38, H-1525 Budapest, Hungary
E-mail: journal.idojaras@met.hu

including all illustrations. MS Word format is preferred in electronic submission. Papers will then be reviewed normally by two independent referees, who remain unidentified for the author(s). The Editor-in-Chief will inform the author(s) whether or not the paper is acceptable for publication, and what modifications, if any, are necessary.

Please, follow the order given below when typing manuscripts.

Title page should consist of the title, the name(s) of the author(s), their affiliation(s) including full postal and e-mail address(es). In case of more than one author, the corresponding author must be identified.

Abstract: should contain the purpose, the applied data and methods as well as the basic conclusion(s) of the paper.

Key-words: must be included (from 5 to 10) to help to classify the topic.

Text: has to be typed in single spacing on an A4 size paper using 14 pt Times New Roman font if possible. Use of S.I. units are expected, and the use of negative exponent is preferred to fractional sign. Mathematical formulae are expected to be as simple as possible and numbered in parentheses at the right margin.

All publications cited in the text should be presented in the *list of references*, arranged in alphabetical order. For an article: name(s) of author(s) in Italics, year, title of article, name of journal, volume, number (the latter two in Italics) and pages. E.g., *Nathan, K.K.,* 1986: A note on the relationship between photosynthetically active radiation and cloud amount. *Időjárás 90,* 10–13. For a book: name(s) of author(s), year, title of the book (all in Italics except the year), publisher and place of publication. E.g., *Junge, C.E.*, 1963: *Air Chemistry and Radioactivity.* Academic Press, New York and London. Reference in the text should contain the name(s) of the author(s) in Italics and year of publication. E.g., in the case of one author: *Miller* (1989); in the case of two authors: *Gamov* and *Cleveland* (1973); and if there are more than two authors: *Smith et al.* (1990). If the name of the author cannot be fitted into the text: *(Miller,* 1989); etc. When referring papers published in the same year by the same author, letters a, b, c, etc. should follow the year of publication. DOI numbers of references should be provided if applicable.

Tables should be marked by Arabic numbers and printed in separate sheets with their numbers and legends given below them. Avoid too lengthy or complicated tables, or tables duplicating results given in other form in the manuscript (e.g., graphs). *Figures* should also be marked with Arabic numbers and printed in black and white or color (under special arrangement) in separate sheets with their numbers and captions given below them. JPG, TIF, GIF, BMP or PNG formats should be used for electronic artwork submission.

More information for authors is available: journal.idojaras@met.hu

Published by the HungaroMet Hungarian Meteorological Service

Budapest, Hungary

ISSN 0324-6329 (Print)

ISSN 2677-187X (Online)